Incorporation of tin in glass melts

Dissertation

zur Erlangung des akademischen Grades doctor rerum naturalium

(Dr. rer. nat.)

vorgelegt dem Rat der Chemisch-Geowissenschaflichen Fakultät der
Friedrich-Schiller-Universität Jena

von Dipl.-Min. Darja Benne
geboren am 11.03.1975 in Gehrden

Gutachter:

1. Prof. C. Rüssel

2. Prof. K. D. Becker

Tag der öffentlichen Verteidigung: 9.07.2003

Contents

Chapter 1

Zusammenfassung

Glasschmelzen und die daraus resultierenden Glasprodukte werden in vielen ihrer Eigenschaften vom Redoxzustand polyvalenter Elemente beeinflusst. Der Einbau von Zinn in Glas und der Redoxzustand von Zinn ist aufgrund des Floatglasprozesses von besonderem Interesse für die Glasindustrie. Ferner werden Zinnverbindungen auch als Läutermittel verwendet. In dieser Arbeit wurde der Einbau von Zinn in Glasschmelzen anhand elektrochemischer Messmethoden in einem Temperaturbereich von 1000–1600°C und ^{119}Sn-Mößbauer-Spektroskopie untersucht. Die Bestimmung der thermodynamischen Daten, Diffusionskoeffizienten, Debye-Temperaturen, sowie der Mößbauerparameter in Abhängigkeit der Zusammensetzung soll zu einem besseren Verständnis des Einbaus von Zinn in Silicat- und Alumosilicatschmelzen führen. Hierfür wurde in Alkali-Erdalkali-Silicatschmelzen und Alumosilicatschmelzen die Alkalioxidkonzentration, die Art des Alkalioxids, die Erdalkalioxidkonzentration, die Art des Erdalkalioxids und die Aluminiumoxidkonzentration variiert.

Die Hauptuntersuchungsmethode dieser Arbeit war die Square-Wave Voltammetrie. Hier wird einer stufenförmig abfallenden Potenzial-Zeit-Kurve mit der Stufenhöhe δE eine Rechteckspannung mit der Amplitude ΔE überlagert. Am Ende jeder Halbwelle wird der Strom gemessen. In den Voltammogrammen wird der Differenzstrom ΔI zweier aufeinanderfolgender Halbwellen gegen das mittlere Potenzial aufgetragen. Tem-

1

peraturabhängige mößbauerspektroskopische Untersuchungen ermöglichen die Bestimmung von Debye-Temperaturen für Sn^{2+} und Sn^{4+} in Gläsern. Die Debye-Temperatur ist ein Maß für die Bindungsstärke und ist somit eng verknüpft mit dem Einbau der jeweiligen Ionen in die Glasstruktur. Zusätzliche Information können aus den Isomerieverschiebungen und der Quadrupolaufspaltung gewonnen werden.

Um zunächst den Mechanismus der Elektrodenreaktion zu klären, wurden impedanzspektroskopische Messungen in der Schmelze $20\ Na_2O \cdot 80\ SiO_2$ (mol%) durchgeführt. In den Square-Wave Voltammogrammen wurde bei hohen Temperaturen ein Peak detektiert. Dieser Peak wird durch eine vollständig reversibel ablaufende Redoxreaktion verursacht. Bei tiefen Temperaturen und kurzen Stepzeiten tritt ein weiterer Peak bei weniger negativen Peakpotenzialen auf. Dieser Peak kann nicht auf eine diffusionskontrollierte Elektrodenreaktion zurückgeführt werden. Impedanzspektren bei hohen Temperaturen wurden unter Verwendung eines einfachen Ersatzschaltbilds, in dem die Warburgimpedanz einen diffusionskontrollierten Elektronentransfer berücksichtigt, simuliert. Bei tieferen Temperaturen konnten die Impedanzspektren nicht mehr mit diesem einfachen Ersatzschaltbild simuliert werden. Das Ersatzschaltbild wurde um einen zusätzlichen Widerstand und eine Kapazität, die eine Adsorption berücksichtigen, erweitert. Es wurden Minima in der Abhängigkeit der Warburgimpedanz vom Potenzial beobachtet. Diese Minima liegen in guter Übereinstimmung mit den Peaks, die in den Square-Wave Voltammogrammen auftreten. Deswegen sind die Minima in der Warburgimpedanz-Potenzialabhängigkeit und die Peakpotenziale in der SWV auf die gleiche Elektrodenreaktion zurückzuführen. Anhand eines Elektrolyseexperiments und mößbauerspektroskopischen Untersuchungen konnte nachgewiesen werden, dass dieser Peak dem Redoxpaar Sn^{4+}/Sn^{2+} entspricht. Es wurden Maxima in der Abhängigkeit der Adsorptionskapazität vom Potenzial beobachtet. Die Lage dieser Maxima stimmt mit den Potenzialen des Peaks, der in der SWV zusätzlich bei tiefen Temperaturen und kurzen Stepzeiten auftritt, überein. Diese Effekte werden durch eine Adsorption einer monomolaren SnO_x-Schicht auf der Arbeitselektrode verursacht. In dieser Ar-

beit wurde zum ersten Mal gezeigt, dass die Adsorption an Elektroden auch bei hohen Temperaturen auftreten kann.

Bei allen untersuchtem Zusammensetzungen verschieben sich die Peakpotenziale des Redoxübergangs Sn^{4+}/Sn^{2+} mit sinkender Temperatur linear zu negativeren Potenzialen. Dies entspricht einer Verschiebung des Sn^{4+}/Sn^{2+}-Redoxgleichgewichts in Richtung Sn^{4+}. Die lineare Abhängigkeit zwischen dem Peakpotenzial und der Temperatur ermöglicht die Bestimmung der Standardreaktionsenthalpie ΔH^0 und der Standardentropie ΔS^0. Durch Messungen der Sauerstoffaktivität ist eine weitere Möglichkeit gegeben, die Standardreaktionsenthalpie ΔH^0 zu ermitteln. Die Ergebnisse beider Methoden zeigen eine gute Übereinstimmung. Desweiteren ermöglicht die Kenntnis der Sauerstoffaktivität und der thermodynamischen Standarddaten die Bestimmung des Redoxzustandes in Schmelzen bei hohen Temperaturen. Es wurde gezeigt, dass das Gleichgewicht in allen untersuchten peralkalischen Schmelzen durch die verwendeten Schmelzbedingungen eingestellt werden konnte.

In Lithiumoxid- und Natron-Silicatschmelzen ist das Peakpotenzial mit steigender Natriumoxidkonzentration im Rahmen der Fehler konstant. Das heißt eine Veränderung der Alkalikonzentration hat keinen deutlichen Einfluss auf das Redoxgleichgewicht. In Kalk-Natron-Silicatschmelzen wurde eine lineare Verschiebung in Richtung negativerer Peakpotenziale mit zunehmender Natriumoxidkonzentration festgestellt. Die Sn^{4+}-Spezies wird also mit zunehmendem Natriumoxidgehalt begünstig eingebaut. In Alkali-Silicatschmelzen führt eine Erhöhung des Alkaliionenradius zu negativeren Potenzialen, was eine Verschiebung in Richtung Sn^{4+} bedeutet. Allerdings tritt dieser Effekt in Alkali-Erdalkali-Silicatschmelzen nur beim Austausch von Natrium zu Kalium auf. Eine Erhöhung der Calciumoxidkonzentration und der Austausch von Calciumoxid zu Magnesiumoxid führt zu einer leichten Erhöhung der Peakpotenzials. Dies entspricht einer leichten Verschiebung des Redoxgleichgewichts in Richtung Sn^{2+}. Eine Erhöhung der Aluminiumoxidkonzentration führt zu einer deutlichen Verschiebung des Peakpotenzials in Richtung positiverer Werte. Dementsprechend wird bei größeren

Aluminiumoxidkonzentrationen die Sn^{2+}-Spezies begünstigt eingebaut. Die Veränderung der Aluminiumoxidkonzentration hat im Vergleich zu den übrigen untersuchten Effekten den stärksten Einfluss auf das Sn^{4+}/Sn^{2+}- Redoxgleichgewicht. In allen peralkalischen Schmelzen, die untersucht wurden, wurde gezeigt, dass der Anteil an Sn^{4+} dominiert.

Die Zinn-Diffusionskoeffizienten zeigen in Natron- und Kalk-Natron-Silicatschmelzen eine lineare Abhängigkeit von der Natriumoxidkonzentration: Bei Zunahme der Natriumoxidkonzentration sinken die Zinn-Diffusionskoeffizienten. Im Gegensatz hierzu hat die Calciumoxidkonzentration nur einen sehr geringen Einfluss auf die Zinn-Diffusion. Auch Veränderungen in der Art des Alkalioxids oder Erdalkalioxids führen nur zu geringen Veränderungen der Zinn-Diffusionskoeffizienten. Veränderungen in der Aluminiumoxidkonzentration haben hingegen einen sehr deutlichen Einfluss auf die Zinn-Diffusionskoeffizienten: Im peralkalischen Bereich ($[Na_2O] > [Al_2O_3]$) steigen die Zinn-Diffusionskoeffizienten mit zunehmenden Aluminiumoxidgehalt an. Im peralumischen Bereich ($[Na_2O] < [Al_2O_3]$) hingegen sinken die Zinn-Diffusionskoeffizienten mit zunehmendem Aluminiumoxidgehalt.

In Kalk-Natron-Silicatgläsern zeigen Mößbauerspektren jeweils ein Sn^{2+}-Signal mit deutlicher Quadrupolaufspaltung und ein Sn^{4+}-Signal mit kleiner Quadrupolaufspaltung. Für das Subspektrum des Sn^{2+}-Ions wurde eine deutliche Asymmetrie beobachtet. Die Isomerieverschiebung von Sn^{2+} sinkt leicht mit zunehmendem Natriumoxidgehalt. Gleichzeitig steigt die Quadrupolaufspaltung leicht an. Diese Effekte werden durch eine leichte Zunahme des kovalenten Anteils der Sn^{2+}-O Bindung mit steigender Natriumoxidkonzentration erklärt. Die Mößbauerparameter von Sn^{4+} sind im Rahmen der Fehler unabhängig von der Natriumoxidkonzentration, d.h. Sn^{4+} weist keine Änderung des Bindungscharakters in Abhängigkeit von der Natriumoxidkonzentration auf. In Alumosilicatschmelzen wird sowohl für das Subspektrum des Sn^{2+}-Ions als auch für das Subspektrum des Sn^{4+}-Ions eine deutliche Asymmetrie beobachtet. Die Isomerieverschiebung von Sn^{2+} ist im Rahmen der Fehler unabhängig von der Aluminiumox-

idkonzentration. Die Quadrupolaufspaltung steigt aber linear mit Zunahme der Aluminiumoxidkonzentration an, d.h. die Symmetrie der Umgebung der Sn^{2+}-Ionen nimmt mit steigender Aluminiumoxidkonzentration ab. Die Isomerieverschiebung von Sn^{4+} steigt mit zunehmenden Aluminiumoxidgehalt linear an, d.h. die s-Elektronendichte am Kernort des Sn^{4+}-Ions nimmt zu. Gleichzeitig ist ein Anwachsen der Quadrupolaufspaltung festzustellen. Sn^{2+} liegt in den untersuchten Gläsern ähnlich wie in amorphem SnO vor. Sn^{4+} besitzt in den untersuchten Gläsern eine verzerrt oktaedrische Koordination. Die Sn^{4+}-O Bindungen haben einen ausgeprägt ionischen Bindungscharakter. Die Debye-Temperaturen betragen für Sn^{4+} $\sim$268K und für Sn^{2+} $\sim$184K, d.h. Sn^{4+} ist wesentlich stärker in das Netzwerk eingebunden als Sn^{2+}. Änderungen der Natriumoxidkonzentration haben keinen Einfluss auf die Debye-Temperaturen, d.h. der Einbau von Zinnionen in die Glasmatrix verändert sich nicht wesentlich.

Die zunehmende Stabilisierung von Sn^{4+}-Ionen mit steigender Natriumoxidkonzentration wurde wie folgt erklärt: Sn^{4+}-Ionen werden in den untersuchten Zusammensetzungen als $[SnO_6]^{2-}$-Komplexe, die von Na^+-Ionen ladungsstabilisiert werden, eingebaut. Im peralkalischen Bereich wird Aluminiumoxid als $[AlO_4]^-$-Tetraeder eingebaut und benötigt Alkaliionen zur Ladungskompensation. Das bedeutet, dass Sn^{4+} und Al^{3+} um Alkaliionen konkurrieren. Aus diesem Grund kann Sn^{4+} mit steigender Aluminiumoxidkonzentration schlechter stabilisiert werden. Im peralumischen Bereich nimmt der Anteil von Sn^{2+} weiter zu. Das hier oktaedrisch eingebaute Al^{3+} kann Sn^{4+} in oktaedrischer Koordination im Gegensatz zu Fe^{3+} nicht stabilisieren.

Werden Sn^{4+}-Verbindungen als Läutermittel verwendet, so liegt die maximale Blasenbildung bei wesentlich höheren Temperaturen als bei herkömmlichen Läutermitteln. Sn^{4+}-Verbindungen sind von daher vielversprechende Hochtemperaturläutermittel.

Chapter 2

Introduction

The incorporation of tin in glass and its valency are of special importance for the glass technology. According to [1] tin usually occurs in the valence states Sn^{4+} and Sn^{2+} in glasses. Under extremely reducing conditions the metallic state might also be formed. During the float glass process the tin of the float bath can be oxidised and tin ions diffuse into the glass surface and interact with other polyvalent elements especially Fe^{2+} and Fe^{3+} [2, 3]. In addition, tin compounds are applied as fining agents [4].

The redox behaviour of polyvalent elements affects many physical properties such as the colour and the optical transmission of glass melts and resulting glass products [5, 6]. As known from the Fe^{3+}/Fe^{2+} redox equilibrium, not only the temperature but also the chemical composition of the glass matrix may have a large effect on the redox equilibrium [7]-[12]. The structure of the glass matrix exercises also a large influence on the diffusion of the respective glass components. In consequence, variations in the diffusion coefficients of polyvalent elements should be correlated with changes of the structure of the melt. In the past few years numerous studies of the effect of the glass composition on the iron diffusion have been carried out [13]-[17]. By contrast, systematic studies of the effect of the glass composition on the thermodynamics of the redox equilibria and on the diffusion of tin ions have rarely been reported in the literature up to now.

Molten glasses with high alkali concentrations are good ionic conductors. Therefore, electrochemical methods such as square-wave voltammetry are a suitable tool to study the thermodynamic behaviour [18]-[21] and enable the determination of diffusion coefficients [13]-[15] of polyvalent ions in glass melts. Another method to study the redox behaviour of polyvalent ions is to equilibrate the melt with an atmosphere of well defined oxygen fugacity. The melt is subsequently quenched and analysed physically or chemically [22]-[24]. The presence of only one polyvalent element is a requirement to apply this method because otherwise redox reactions may occur during cooling and the redox ratios in the melt and in the solid glass are no longer the same [18].

Mössbauer spectroscopy at high temperatures provides an alternative method to study the incorporation of tin in glasses and enables the determination of redox states. Temperature dependent in-situ experiments allow the determination of the Debye temperatures specific for Sn^{2+} and Sn^{4+} ions in the glass. The Debye temperature is a measure for the strength of local bonding and is closely connected with the mode of incorporation of the respective ions in the glass structure [25]-[27]. Additional information on the structure of the glass can be obtained from the temperature dependent quadrupolar interactions and isomer shifts of Sn^{2+} and Sn^{4+}. The majority of the earlier Mössbauer spectroscopic investigations of tin have been carried out at room temperature or lower temperatures [25]-[39]. Up to now, systematic studies of the effect of the glass composition on the incorporation of tin using Mössbauer spectroscopy at high temperatures have not been reported in the literature.

In this thesis, both square-wave voltammetric measurements and Mössbauer spectroscopic experiments have been performed at high temperatures in alkali-alkaline earth-silicates as well as in alumosilicates. The determination of the thermodynamics of redox equilibria, diffusion coefficients, Mössbauer parameters and Debye temperatures as a function of the glass composition shall contribute to a better understanding of the structural incorporation of tin in silicate melts.

Chapter 3

Principles and methods

3.1 Thermodynamics

The behaviour of polyvalent species with regard to their thermodynamics can be studied by electrochemical methods. In the case of tin, the electrode reaction is described as follows: The reduced state Sn^{2+}, the oxidised state Sn^{4+} and the physically dissolved oxygen of the melt are in equilibrium at high temperatures [40, 41]:

$$Sn^{4+} + O^{2-} \leftrightarrows Sn^{2+} + \frac{1}{2}O_2 \tag{3.1}$$
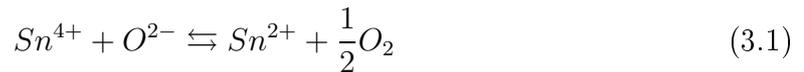
The equilibrium constant $K(T)$ depends on the glass composition and the temperature [40]:

$$K(T) = \frac{a_{Sn^{2+}} \cdot a_{O_2}^{1/2}}{a_{Sn^{4+}} \cdot a_{O^{2-}}} \tag{3.2}$$

where a_i are the activities of the respective species.

Assuming that the oxygen ion activity of the melt is constant, it can be included in the equilibrium constant. Thus, $K^*(T)$ is dependent on the glass composition. If only

a small quantity of the polyvalent element is present, the respective ion concentrations can replace the ion activities:

$$K^*(T) = \frac{[Sn^{2+}]}{[Sn^{4+}]}[a_{O_2}]^{\frac{1}{2}} = e^{-\Delta G^0/RT} \tag{3.3}$$

where R is the gas constant and T the temperature. Assuming an equilibrium with the surrounding atmosphere the oxygen partial pressure p_{O_2} replaces the oxygen activity a_{O_2}, if $a_{O_2} = p_{O_2}/p^0, p^0 = 1$ bar. As a result, the Nernst equation can be written as:

$$E = E^0 + \frac{RT}{2F}ln\frac{[Sn^{4+}]}{[Sn^{2+}] \cdot p_{O_2}^{1/2}} \tag{3.4}$$

where F is the Faraday constant and E^0 the standard potential expressed relative to a reference electrode. This electrode is an Y_2O_3 doped ZrO_2 solid electrolyte with air as reference gas. The standard free enthalpy ΔG^0 of the redox reaction can be calculated from the equilibrium constant and correlated to the standard potential of the redox reaction:

$$\Delta G^0(T) = -RT \cdot lnK^*(T) = \Delta H^0 - T \cdot \Delta S^0 = -2F \cdot E^0(T) \tag{3.5}$$

By rearranging Eq. (3.5), Eq. (3.6) is obtained:

$$E^0 = \frac{T\Delta S^0}{2F} - \frac{\Delta H^0}{2F} \tag{3.6}$$

If the dependency of E^0 or K on temperature has been measured, it is possible to calculate the standard enthalpy ΔH^0 and the standard entropy ΔS^0:

$$\Delta S^0 = 2F\left(\frac{\partial E^0(T)}{\partial T}\right) \tag{3.7}$$

$$\Delta H^0 = 2F\left[T\left(\frac{\partial E^0(T)}{\partial T}\right) - E^0(T)\right] \tag{3.8}$$
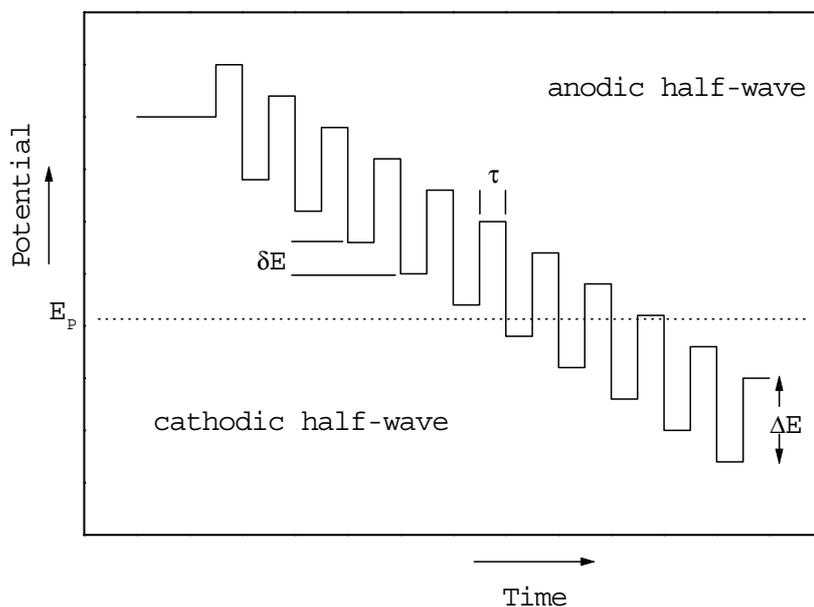
Figure 3.1: Potential time dependency for square-wave voltammetry.

Furthermore, the equilibrium constant can be calculated from the standard potentials by Eq. (3.9).

$$lnK^*(T) = \frac{2F}{RT}E^0(T) \tag{3.9}$$

3.2 Square-wave voltammetry (SWV)

Square-wave voltammetry (SWV) —a fast potentiostatic method— is one of the four major voltammetric techniques. Its application has boomed in the last decade due to a well developed theory and its high sensitivity to surface confined electrode reactions. The theory and application of SWV were described in several reviews [42]-[44]. The method originated from Barker's square-wave polarography [45].

As shown in Fig. 3.1, the applied potential is a staircase ramp with a step height δE superimposed by a rectangular wave of comparably short pulse time ($\tau = 1$–500 ms)

and high amplitude ($\Delta E = 50$–250 mV). Each square-wave period occurs during one staircase period τ. The current is measured at the end of every half-wave. The currents of anodic and cathodic half-waves are subsequently subtracted. This eliminates the charging currents since they decay much more rapidly than Faradaic currents. A more detailed description of this method is given by Claußen [46].

3.3   Determination of diffusion coefficients

Diffusion coefficients can be calculated from SWV on condition that the following requirements are fulfilled: First, the electrode reactions of polyvalent elements during voltammetric measurements have to be reversible, second, the reaction ought to be controlled by diffusion, third, the polyvalent species is predominantly present in its oxidised form ($c_0 \approx c_{ox}$) at the start potential and fourth, $\Delta E < \frac{RT}{2F}$. The current, which is measured at the end of a half-wave, is given by the following equations:

$$I_j = 2FAc_0 \left(\frac{D}{\pi\tau}\right)^{\frac{1}{2}} \sum_{m=1}^{j} \frac{Q_{m-1} - Q_m}{\sqrt{j - m + 1}} \tag{3.10}$$

$$\text{with} \quad Q_m = \frac{\epsilon_m}{1 + \epsilon_m} \tag{3.11}$$

$$\text{and} \quad \epsilon_m = exp\left(\frac{2F(E_m - E^0)}{RT}\right) \tag{3.12}$$

where A is the area of the immersed working electrode, D the diffusion coefficient and E_m the potential of the corresponding step.

In the voltammograms, the subtracted current $\Delta I = I_j - I_{j+1}$ with $j = 1, 3, 5...$, is plotted as a function of the corresponding potential $E_i = \frac{1}{2}(E_j + E_{j+1})$ of the staircase waveform. ΔI is maximum when the majority of ions are reduced or oxidised. The corresponding peak current ΔI_P is given by:

$$\Delta I_P = 0.31 \frac{4F^2 A c_0 \Delta E}{RT} \cdot \left(\frac{D}{\pi\tau} \right)^{\frac{1}{2}} \tag{3.13}$$

Self-diffusion coefficients of polyvalent elements can be calculated from the peak currents by Eq. (3.13), if the bulk concentration and the surface area of the working electrode are known.

The dependency of the self-diffusion coefficients on temperature is described over a wide temperature range by the Arrhenius equation:

$$D = D_0 \cdot e^{-E_D/RT} \tag{3.14}$$

where E_D is the activation energy of the diffusion process and D_0 is a constant. A more detailed description of these basics is given by Claußen [46].

As pointed out in Eq. (3.13), for the determination of diffusion coefficients, it is obligatory to know the area of the working electrode which can be evaluated from the conductivity of the glass melt [47]. The conductivity of an electrolyte is proportional to the concentration and the mobility of its charge carriers as well as to the area of the working electrode. In this procedure, a high frequency rectangular wave (10 kHz) is applied to the glass melt. In this way, a charging current is supplied during the entire pulse time which is limited by the conductivity of the glass melt. The conductivity can be determined from the potential amplitude and the measured currents. Because of the linear relation between the reciprocal resistance and the area of the working electrode, the absolute area of the immersed electrode can be determined by a defined variation of the immersion depth of the electrode [48].

3.4 Oxygen activity

Oxygen sensors for the *in-situ* measurement of the oxygen activity in glass melts have been developed in order to determine the oxidation states at high temperatures. For

some years it has been possible to measure the oxygen activity by means of sensors based on oxygen ion-conducting solid electrolytes [49]-[51].

Oxygen is physically dissolved in the molten glass and is in equilibrium with polyvalent cations such as tin (see Eq. (3.1)). The equilibrium constant is defined as follows:

$$a_{O_2} = K^*(T) \left(\frac{a_{Sn^{4+}}}{a_{Sn^{2+}}} \right)^2 \tag{3.15}$$

While the glass melt is cooling down from temperature T_1 to T_2 the equilibrium, according to Eq. (3.1), is shifted to the left side and the oxygen activity decreases. If the cooling of the molten glass is rapid, only the physically dissolved oxygen reacts with Sn^{2+} ions. Since the diffusion coefficients are too low, the oxygen from the furnace can not participate. On condition that only one type of polyvalent element is present, the concentration of physically dissolved oxygen is small and the reaction of the metal ions does not change the electrode potential, the standard enthalpy of the redox equilibrium (3.1) can be determined, according to [52, 53]:

$$ln\frac{a_{O_2}^{(1)}}{a_{O_2}^{(2)}} = \frac{2\Delta H^0}{R} \left(\frac{1}{T_1} - \frac{1}{T_2} \right) \tag{3.16}$$

The quantity measured by the oxygen sensor is the electromotive force E of the electro-chemical cell. The oxygen activity a_{O2} in the melt can be calculated from the measured potential difference ΔE [51]:

$$a_{O_2} = p_{O_2}(air) \cdot e^{4F\Delta E/RT} \tag{3.17}$$

where p_{O_2} is the oxygen partial pressure in air and 4 the number of electrons transferred per molecule O_2.

In combination with the Gibbs free enthalpy —which can be determined by square-wave voltammetric measurements, the redox ratio in the glass melt can be derived: The ion concentration replaces the respective ion activity in Eq. (3.15) (see section 3.1). Substituting Eq. (3.15) in Eq. (3.5) and rearranging it, results in Eq. (3.18).

$$\frac{[Sn^{4+}]}{[Sn^{2+}]} = a_{O2}^{1/2} \cdot e^{\Delta G^0/RT} \tag{3.18}$$

3.5   Electrochemical impedance spectroscopy (EIS)

In electrochemical impedance spectroscopy (EIS) the frequency band ranges between 10^{-4} and $> 10^6$ Hz. In principle, electrochemical impedance spectroscopy can be applied to any material and system, provided that a change of the electric voltage between the two poles leads to a characteristic change of the current. Measurements on electrochemical systems are one of the most important applications. However, up to now, electrochemical impedance spectroscopic studies in glass melts have rarely been reported [54]-[56].

Partial steps of a chemical reaction can be attributed to different impedance elements which contribute to the total impedance. By analysing impedance spectra, individual impedance elements can be defined: Ohmic resistances R and differential resistances R_{diff} are widely applied partial impedances:

$$R = \frac{E}{I} \tag{3.19}$$

$$R_{diff}(E) = \frac{dE}{dI} \tag{3.20}$$

For instance, an electrolyte-resistance acts approximately like an Ohmic resistor. Typical values of observed resistances are of the order of several Ω in the regarded systems. Capacitive behaviour of partial impedances is just as fundamental as the resistive behaviour. For example, double layer capacitances are potential dependent due to changes of the layer structure with the potential and therefore, are represented by a differential capacitance C_{Diff}:

$$C_{diff}(E) = \frac{I}{\frac{dE}{dt}} \quad \text{for I} = \text{const} \tag{3.21}$$

"Pseudo-capacitances" follow the same laws (Eq. (3.21)) as proper capacitances. They appear, e.g., due to the covering of electrode surfaces by the adsorption of substances. Double layer capacitances range from one up to several μF and for covering layer capacitances from less than one nF to the size of double layer capacitances. As a third component magnetic inductances L are observed in impedance spectroscopic studies of electrochemical systems:

$$\frac{dI}{dt} \cdot L = E \tag{3.22}$$

They exist almost only in form of parasitic inductances which emerge from the current feeding lines. Typical values of inductances are 0.1 to several μH. Resistance, capacitance and inductance represent the classic impedance elements. Further involved impedance elements do not possess equivalents in electrical engineering, e.g. the Warburg impedance. Mostly, several partial impedances are coupled in circuits either as parallel connections and/or series connections.

With a given potential at an electrode, a stationary or not too fast changing state is adjusted, to which a current I corresponds. The superposition of a sinus-ac voltage $E(t)$ of frequency f causes the appearance of an ac-component $I(t)$. $I(t)$ can also be regarded as sinusoidal. The current amplitude $I_\sim$ is proportional to $E_\sim$ and consequently, the amplitude ratio $E_\sim/I_\sim$ is non variable at a given frequency and small $E_\sim$. If the current depends on the previous values of the potential at any given time-dependency of the potential, the sine signals $E(t)$ and $I(t)$ show a phase shift φ. Hence, the amplitude ratio $E_\sim/I_\sim$ is frequency dependent.

The impedance is defined as:

$$Z(f) = \frac{E_\sim}{I_\sim} e^{j \cdot \varphi} \quad \text{with } \varphi = \varphi_E - \varphi_I \tag{3.23}$$

where $E_\backsim$ and $I_\backsim$ are the amplitudes of *E(t)* and *I(t)*, φ_E and φ_I are the phase shifts of *E(t)* and *I(t)*, related to the cosine function respectively, *j* is the imaginary unit. From the characteristic curves of impedance spectra direct conclusions may be drawn with regard to the participating partial impedances and their connections within the circuit. Equations (3.24)–(3.26) give the ac-analogue from the time domain law to ohmic resistance, capacitance and inductance. By contrast, Z is a complex value.

$$Z_R = R \tag{3.24}$$

$$Z_C = \frac{E_\backsim}{I_\backsim} = \frac{1}{C \cdot j\omega} \tag{3.25}$$

$$Z_L = \frac{E_\backsim}{I_\backsim} = L \cdot j\omega \tag{3.26}$$

In order to understand the results from impedance spectroscopy on electrochemical systems, it is necessary to develop additional partial impedances, for instance, for diffusion reactions. For example, the Warburg diffusion impedance can be written as follows [57]:

$$Z_W = \frac{W}{(j \cdot \omega)^{1/2}} \quad \text{with} \quad W = \frac{|\nu| \cdot p \cdot R \cdot T \cdot \alpha}{n^2 F^2 \cdot c \cdot D^{1/2} \cdot A} \tag{3.27}$$

where ν is the stoichiometric number, p the reaction order, c the concentration, D the diffusion coefficient, A the surface of the electrode and $\alpha = \frac{\text{partial current}_{I_k}}{\text{exchange current}_{I_x}}$.

3.6 Mössbauer spectroscopy

The emission of gamma rays by a free nucleus in an excited state is accompanied by nuclear recoil. As a result of this recoil, the energy of the emitted gamma ray is less than the energy difference between the two nuclear levels. Thus, for free nuclei the recoil energy prevents resonant absorption of gamma rays under normal circumstances.

Mössbauer discovered that a nucleus in a solid can emit and absorb gamma rays without recoil. In a solid matrix the emitting or absorbing nucleus is fixed within the lattice. In this situation, the recoil energy may be less than the lowest quantised lattice vibrational energy and consequently the gamma ray may be emitted without any loss of energy due to the recoil of the nucleus.

3.6.1 Debye-Waller factor

In the Debye model, the probability of recoil-free absorption or emission (Debye-Waller factor) is given by:

$$f_D(T) = exp\left[-\frac{3E_r}{2k\theta_D}\left(1 + 4\left(\frac{T}{\theta_D}\right)^2 \cdot \int_0^{\frac{T}{\theta_D}} \frac{x}{e^x - 1}\,dx\right)\right] \qquad (3.28)$$

where E_r is the recoil energy ($E_r(Sn) = 4.1171 \cdot 10^{-22}$ J), Θ_D the Debye temperature and k the Boltzmann constant. At higher temperatures Eq. (3.28) is modified as

$$ln\,f_D(T) \approx -\frac{6E_r T}{k\theta_D^2} \qquad \text{for} \qquad T > \frac{\theta_D}{2} \qquad (3.29)$$

By plotting $ln\,A$ (absorption area) versus the temperature T, Θ_B can be obtained from the slope of a straight line.

The Debye temperature is a measure for the strength of local bonding and is closely connected with the mode of incorporation of the respective ions in the glass structure. Debye temperatures Θ_B higher than 280K have been observed for network formers, whereas Debye temperatures Θ_B less than 270K have been taken as evidence for a network modifier [25]-[27].

The knowledge of the Debye-Waller factors f_D of the respective tin species is essential for the determination of the correct Sn^{4+}/Sn^{2+} ratios in tin glasses [58].

3.6.2   Mössbauer parameters

Isomer shift (IS)

The isomer shift (IS) of the absorption lines is a result of the electric monopole interaction between the nuclear charge distribution and the electronic charge density over the finite nuclear volume. The shift arises because of the difference in the nuclear volume of the ground and excited states, and the difference between the electron densities at the Mössbauer nuclei in different materials.

Since the major influence of the electron density at the nucleus is due to the s-electrons, these electrons contribute basically to the isomer shift, while p and d electrons exert shielding effects. An increase in the valence s-shell population increases the electron density at the nucleus. Accordingly, the isomer shift responds to any factor which can change the number or distribution of valence shell electrons. Therefore, it provides information about the valency states, hybridisation and the character of the chemical bonding.

In the case of Sn^{4+} with its ideal ionic configuration $4d^{10}$, an increase of the isomer shift corresponds to an increase in the number of 5s-electrons associated with the tin ions and represents an increase in the partial covalent character of the chemical bonds [59, 60]. For Sn^{2+}, the completely ionic configuration is $4d^{10}5s^2$. The transition from the ionic ($5s^2$) configuration towards a more covalent 5s-p hybridisation is accompanied by a decrease in the 5s-electron density and increases the electrical field gradient. There is a rough negative correlation between IS and QS [61]. Thus, for Sn^{2+}, a decreasing shift accompanied by an increase in the quadrupolar interaction corresponds to an increase in the covalent character of the chemical bonds.

Since the isomer shift represents the difference between the electronic monopole interactions in the source and the absorber, the IS are expressed throughout this thesis relative to $CaSnO_3$.

Quadrupole splitting (QS)

When the nuclear quadrupole moment experiences an asymmetric electrical field, produced by an asymmetric electronic charge distribution or ligand arrangement, an electric quadrupole interaction occurs, which gives rise to a splitting of the nuclear energy levels. The asymmetric charge distribution or ligand arrangement is characterised by the electric field gradient (EFG), which contains different contributions. One contribution arises from the valence electrons of the Mössbauer atom itself and is associated with the asymmetry in the electronic structure, i.e. partly filled electronic shells occupied by the valence electrons. Another contribution arises from asymmetric arrangements of the ligand atoms in non cubic lattices. A third one arises from dissimilar ligands in the coordination sphere. Therefore, the quadrupole splitting reflects the symmetry of the bonding environment and the local structure in the vicinity of the Mössbauer atom.

For an isolated Sn^{2+} ion, the outer electron configuration is $5s^2$, which is spherically symmetrical and hence, does not contribute to the EFG. Consequently, in Sn^{2+} compounds, the non bonding lone pair of electrons —which possesses strong p-character— on the tin ion generates the dominant contribution on the EFG. Sn^{4+} has a closed-shell electron configuration, and hence only a small quadrupole splitting.

Chapter 4

Experimental

4.1   Glass compositions and melting procedure

In the following, glass compositions which have been investigated in this thesis are summarised. All compositions are given in mol%.

- x Li_2O · (100-x) SiO_2 with x = 26, 33

- x Na_2O · (100-x) SiO_2 with x = 15, 20, 26, 33

- x Na_2O · 10 CaO · (90-x) SiO_2 with x = 10, 16, 20, 26

- 16 R_2O · 10 CaO · 74 SiO_2 with R = Li, Na, K

- 16 Na_2O · 10 RO · 74 SiO_2 with R = Mg, Ca

- 20 Na_2O · x CaO · (80-x) SiO_2 with x = 0, 10, 20

- 16 Na_2O · 10 CaO · x Al_2O_3 · (74-x) SiO_2 with x = 5, 10, 15, 20

- 10 Na_2O · 10 CaO · x Al_2O_3 · (80-x) SiO_2 with x = 5, 15, 25

The glasses have been melted in a platinum crucible from the raw materials Li_2CO_3, Na_2CO_3, $CaCO_3$, $MgCO_3$, $Al(OH)_3$ and SiO_2 at temperatures ranging from 1250° to 1600°C —depending on the glass composition— and have subsequently been fritted in cold water. The glass fritts have been crushed and mixed with 0.25, 0.5 or 1 mol% SnO_2 (added as Sn(II)-oxalate). These mixtures have been melted at 1600°C using the same platinum crucible which has later been employed for the SWV measurements. SnO_2 has been added as Sn(II)-oxalate because a complete dissolution of SnO_2 is only possible in this way and by treatment at high melting temperatures. The melts have been fritted twice in order to homogenise them. After homogenisation the melts have been left in the crucible to cool down and the crucible has been transferred into the SWV equipment. After performing SWV measurements the glasses have been heated to temperatures ranging from 1500° to 1600°C and poured on a Cu-block subsequently.

In order to perform Mössbauer experiments, glass fritts have been doped with 1.5 to 3 mol% SnO_2 and have been melted in SiO_2- or Al_2O_3-crucibles —depending on the glass composition— at temperatures in the range from 1500° to 1600°C. The melts have subsequently been poured on a Cu-block. (The same samples which have been prepared for SWV have been used for Mössbauer measurements of glasses doped with smaller SnO_2 concentrations).

Additionally the fritts x $Na_2O \cdot 10$ CaO $\cdot$ (90-x) SiO_2 with x = 10, 16, 20, 26 have been doped with 2 mol% SnO_2 and have been melted in a SiO_2 crucible at temperatures between 1400° and 1500°C for 2–3 hours. In order to produce reduced melts, 0.2 wt% carbon has been added. The melts have subsequently been fritted.

4.2 Square-wave voltammetry

In Fig. 4.1(a) the schematic experimental set-up is shown. The SWV experiments have been carried out in a Superkanthal vertical resistance-heated furnace ($MoSi_2$). In the middle of the alumina tube (furnace tube), a platinum crucible containing the glass

melt is located and three electrodes are inserted in the crucible: One of them is the working electrode consisting of a platinum wire 1 mm in diameter. The second electrode is a reference electrode, a rod of yttria stabilised zirconia being attached to an alumina tube by a ceramic binder. The third is a platinum plate (surface size: 2 cm^2) being used as the counter electrode. Inside of the alumina tube a platinum wire is inserted and air is used as reference gas. All potentials throughout this thesis are referenced to this electrode. The platinum crucible is placed on a second —smaller— alumina tube which can be adjusted from the bottom in that way that the level of the molten glass can be exactly varied. A dc-power supply is used. Electronics are self-constructed [46]. The main part consists of a potentiostat (Bank Elektronik Modell 75 L), which controls the potentials between the electrodes in such a way that the potential between working and reference electrode is equal to the required value. The potentiostat is connected to a microcomputer via digital/analogue and analogue/digital converters. The potential of the working electrode is measured relative to the ZrO_2-probe as reference electrode. No current is applied to the reference electrode and the reference electrode maintains a constant potential throughout the whole experiment. The potential of the working electrode is corrected in a way that it should correspond to a potential value controlled by a PC. The current is measured between the working and the counter electrode. For a more detailed description, see Ref. [46].

SWV measurements have been performed in the temperature range from 900° or 1000°C to 1500° or 1600°C, depending on the glass composition, using step times of $\tau = 2$, 5, 10, 20, 50, 100, 200 and 400 ms. All glass compositions doped with 0.25 or 0.5 mol% SnO_2, respectively, have been investigated by means of SWV. Additionally, SWV measurements have been carried out in the glass melt 20 Na_2O · 80 SiO_2 doped with three different SnO_2 concentrations (0.25, 0.5 and 1 mol%).

For each composition a glass with and without tin has been measured.

(a)   (b)
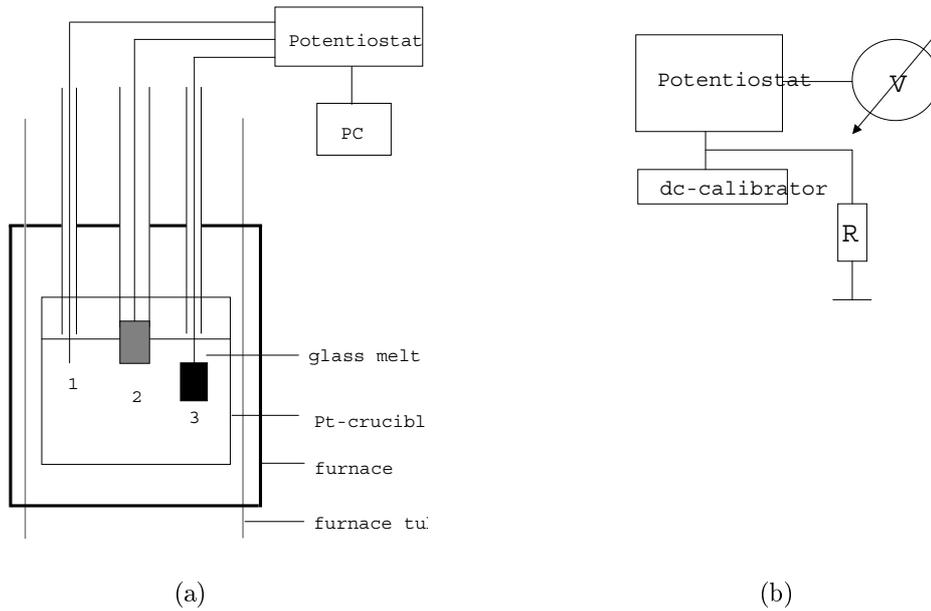
Figure 4.1: Schematic drawing of the experimental set-up for (a) SWV and (b) electrolysis. 1: working electrode 2: zirconia based solid electrolyte (reference electrode) 3: counter electrode.
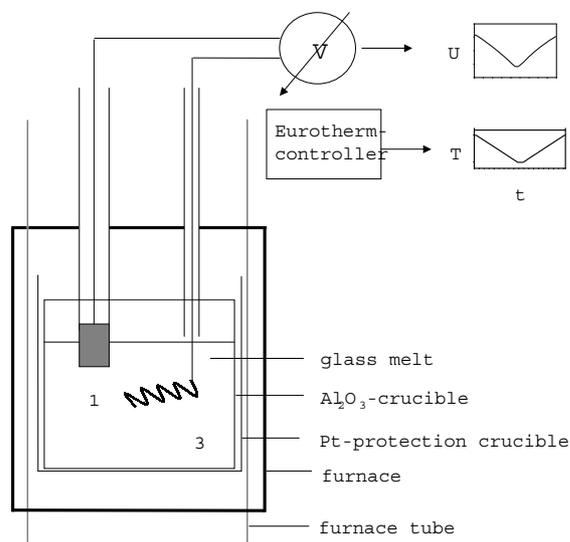

Figure 4.2: Schematic drawing of the experimental set-up for oxygen activity measurements. 1: zirconia based solid electrolyte (reference electrode) 2: working electrode.

4.3 Oxygen activity measurement

Figure 4.2 shows a schematic drawing of the electrochemical cell which has been employed for oxygen activity measurements. The molten glass is located in a Al_2O_3-crucible, which is inserted into a platinum crucible functioning as a protection. The ZrO_2 reference and the platinum measuring electrode are immersed into the glass melt. The reference electrode is described in detail in section 4.2. The measuring electrode consists of a platinum plate (1 cm $\cdot$ 5 cm) twisted as a curl. The measuring electrode has to be completely immersed in the molten glass: If a Pt wire is not fully immersed into the melt, it does not behave like an indicator electrode because its potential is influenced by the three-phase boundary (atmosphere-electrode-melt) and changes with the oxygen partial pressure of the atmosphere. Only when the electrode surface is isolated from the three-phase boundary it will act as an indicator electrode [50]. Furthermore, the surface of the working electrode should be large enough in order to prevent an uptake of oxygen from the atmosphere [62]. The platinum crucible is placed on an alumina tube in the same way as in the experimental set-up used for SWV (see section 4.2).

The glasses 20 Na_2O $\cdot$ 80 SiO_2, 16 Na_2O $\cdot$ 10 CaO $\cdot$ 20 Al_2O_3 $\cdot$ 54 SiO_2 and 10 Na_2O $\cdot$ 10 CaO $\cdot$ 25 Al_2O_3 $\cdot$ 55 SiO_2 have been heated to 1500° or 1600°C —depending on the glass composition— using a heating rate of 10K/min. Then, the electrodes have been immersed into the glass melt. The temperature has been cycled between 1200° or 1300°C and 1500° or 1600°C —depending on the glass composition, with a heating rate of 5 K/min and 30 min holding time at minimum and maximum temperatures. The potential difference has continuously been measured by a digital voltmeter (type MetraHit 22S). Time, temperature and potential have simultaneously been recorded by a computer using memory adapters (type MetraHit Si232) and Metrawin 10 software (Gossen-Metrawatt Camille Bauer). A different temperature program has been employed for measurements in the glass melts: x Na_2O $\cdot$ 10 CaO $\cdot$ (90-x) SiO_2 with x = 10, 16, 20, 26 doped with 2 mol% SnO_2 and 0.2 wt.% added carbon. The temperature

has been cycled between 1200° and 1400° or 1500°C with a heating rate of 5K/min and 5 min holding time at maximum and minimum temperatures.

4.4   Electrochemical impedance spectroscopy

For electrochemical impedance spectroscopy a Zahner IM5d (Zahner Elektrik, Kronach, Germany) equipment is used. The same three-electrode arrangement and experimental set-up as described in section 4.2 is employed. The spectra have been recorded in a frequency range from 10^{-2} to 10^5 s^{-1} as a function of the dc-voltage. The applied dc-voltage has been varied between 0.1 V and - 0.7 V at temperatures ranging from 900° to 1450°C. The spectra have been simulated using Thales software (Zahner Elektrik, Kronach, Germany) and appropriate equivalent circuits. Measurements have been carried out in the melt 20 $Na_2O \cdot 80$ SiO_2 doped with 0.25 mol% SnO_2.

4.5   Electrolysis

The same three-electrode arrangement and experimental set-up as used for SWV (see section 4.2) is employed. Figure 4.1(b) shows a schematic experimental set-up employed for electrolysis. Using a dc-calibrator (Knick) which is connected to a potentiostat the potential has been adjusted. The potentiostat transforms the current generated by the dc-calibrator into the demanded potential by a 100 Ω resistance. A multimeter (MetraHit 22S) is measuring the applied potential.

The glass 20 $Na_2O \cdot 80$ SiO_2 doped with 0.25 mol% SnO_2 has been heated to 1500°C by 10K/min. Then, the electrodes have been immersed into the glass melt. After the glass melt has been cooled down by 10K/min to 1350°C, a potential of -318 mV has been applied for 20 hours. After removing the potential, the glass melt has been heated to 1500°C by 10K/min in order to pull out the electrodes. The working electrode has been embedded in epoxy resin for further investigations.

4.6 Mössbauer spectroscopy

Mössbauer measurements have been carried out in standard transmission geometry and with standard data acquisition electronics. A $Ca^{119m}SnO_3$ radiation source has been used with a initial mean activity of approximately 15 mCi for measurements of tin in silicate or in alumosilicate glasses, respectively. The transmitted radiation has been detected using a 0.5 mm NaJ(Tl) crystal scintillation detector which provides high efficiency and good energy resolution at the same time. Additionally, in combination with the detector, a 25 μm thick Pd filter is used in order to reduce the K_{α}- radiation of ^{119}Sn. All spectra have been recorded using the sinusoidal drive mode, which allows to minimise the error of the driving unit. The 1024 channels per period result in folded spectra of 512 channels. Temperature dependent measurements have been carried out a using specially designed high-temperature furnace allowing for measurements up to 1300°C [63, 64].

The optimum weights of the glass absorbers have been calculated by the Recoil Software Suite [65]. The powdered glasses have been filled into polymethacrylate sample holders in order to provide absorbers of identical thickness. The spectra have been recorded for times from 24 hours to 10 days —depending on the mean activity of the radiation source— at different temperatures from 20° to 500°C. The data were fitted by means of the Recoil software using Voigt-based line shapes. These line shapes account for the heterogeneous distribution of nuclear interactions of the different ionic tin species in the glass and reflect slightly different neighbourhoods around each Mössbauer ion.

The following compositions have been investigated by means of Mössbauer spectroscopy: x $Na_2O \cdot$ (100-x) SiO_2 with x = 20, 26; x $Na_2O \cdot$ 10 $CaO \cdot$ (90-x) SiO_2 with x = 10, 16, 20, 26 melted in air and with the addition of carbon; 16 $Na_2O \cdot$ 10 $CaO \cdot$ x Al_2O_3 $\cdot$ (74-x) SiO_2 with x = 5, 15, 20. The SnO_2 dopant concentrations are given in Tables C.1–C.3.

Chapter 5

Glass properties

Glass properties have been determined for all glass compositions if phase separation or crystallisation did not prevent their evaluation. The density of the glass has been determined by measuring the buoyancy of a glass sample in CCl_4. Dilatometric measurements (Netzsch) have been carried out in order to obtain values of the two thermal properties, glass transition temperature T_g and thermal expansion coefficient α. A list of the determined values is given in Table A.1.

Viscosities

The viscosities of the respective melt compositions have been measured by a rotation viscometer (Bähr VIS 403). The glasses have been melted in a Pt/Rh crucible and located in the middle of a resistance heated furnace. A cylindrical Pt/Rh rotor has been inserted into the glass melt from the top of the furnace. The rotation velocity and the corresponding force has been controlled by a computer. Viscosity curves have been corrected using the DGG1 standard glass.

The extrapolation of the viscosity-temperature-course of glasses at higher temperatures has been calculated by the Vogel-Fulcher-Tammann equation (VFT) (5.1) [66].
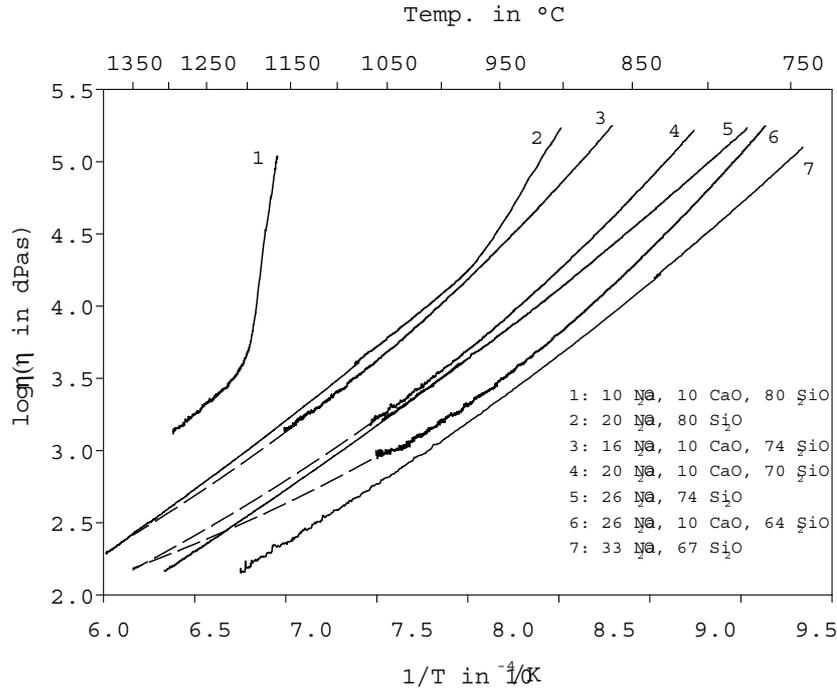
Figure 5.1: Viscosities of soda- and soda-lime-silicate melts as a function of the reciprocal temperature. Solid lines: experimental curves. Dashed lines: calculated curves. Data for curve 7 by M. Leister [67].

$$log\eta = A + \frac{B}{T - T_0} \tag{5.1}$$

The determined VFT-parameters are listed in Table A.2.

In Figure 5.1 viscosities of soda- and soda-lime-silicate melts are plotted as a function of the reciprocal temperature. For comparison, the data for 33 Na_2O · 67 SiO_2 are included [67]. In the melt 10 Na_2O · 10 CaO · 80 SiO_2 phase separation and in the melt 15 Na_2O · 85 SiO_2 crystallisation has occurred at lower temperatures (see section 7.3.1). This prevents the accurate determination of the viscosity. In general, the viscosity is found to decrease with increasing Na_2O concentration.

Viscosities of alkali-alkaline earth-silicate melts are presented in Fig 5.2. In the melt 16 Li_2O · 10 CaO · 74 SiO_2 phase separation and in the melt 20 Na_2O · 20 CaO · 60 SiO_2 crystallisation has occurred at lower temperatures (see section 7.3.1). The viscosity decreases with decreasing size of the alkali ion, i.e. the sequence K → Na
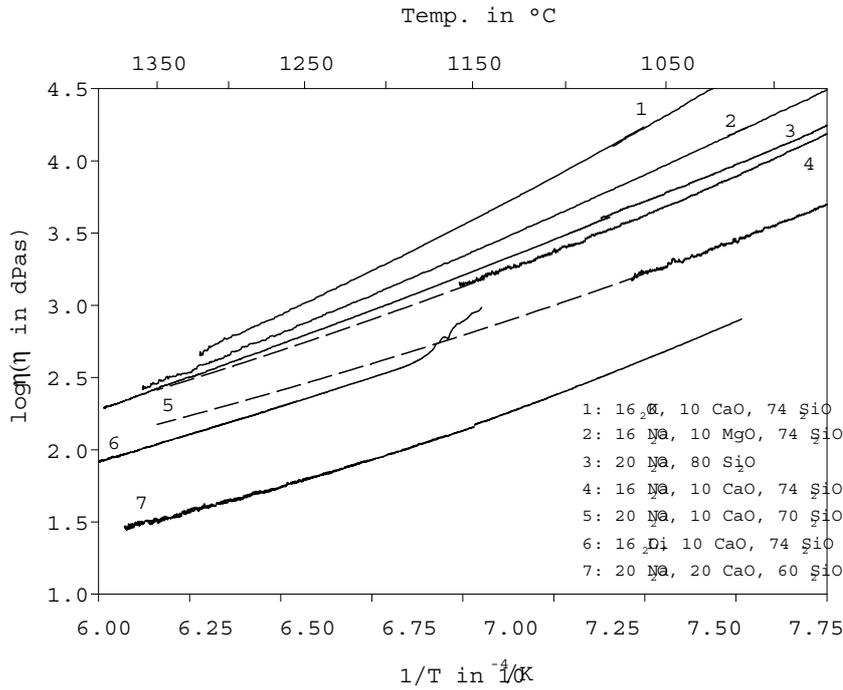
Figure 5.2: Viscosities of alkali-alkaline earth-silicate melts as a function of the reciprocal temperature. Data for curve 1 and 2 by S. Gerlach [68].
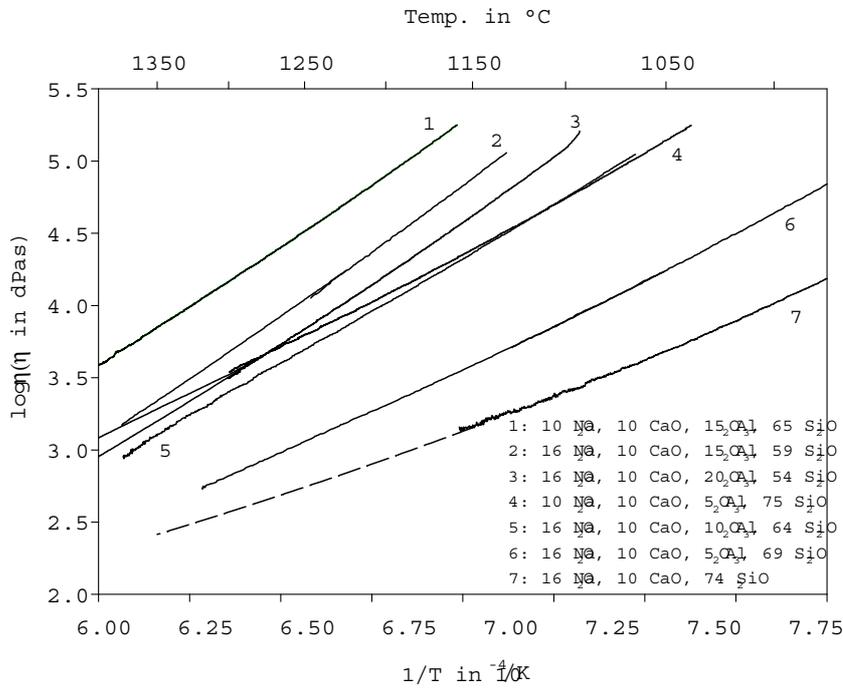

Figure 5.3: Viscosities of alumosilicate melts as a function of the reciprocal temperature. Data for curve 2, 5 and 6 by S. Gerlach [68].

$\rightarrow$ Li. The addition and of CaO to a soda-silicate melt decreases the viscosity. The viscosity of the melt 16 $Na_2O \cdot 10$ $MgO \cdot 74$ SiO_2 is larger than the viscosity of the melt 16 $Na_2O \cdot 10$ $CaO \cdot 74$ SiO_2.

Viscosities of alumosilicates with different Na_2O and Al_2O_3 concentration are plotted in Fig. 5.3. The viscosities are observed to increase with increasing Al_2O_3 concentration. On the other hand, Al_2O_3 concentrations larger than 15 mol% lead to a decrease in the viscosity of alumosilicate melts containing 16 mol% Na_2O. Melts with 10 mol% Na_2O show larger viscosities than those with 16 mol% Na_2O having the same Al_2O_3 concentration.

Chapter 6

The mechanism of the electrode reaction

6.1   SWV in the melt 20 Na$_2$O · 80 SiO$_2$

In Figs. 6.1 and 6.2 square-wave voltammograms recorded in the melt 20 Na$_2$O · 80 SiO$_2$ at 1100° and 1350°C, respectively, are shown for numerous step times. At 1100°C a distinct peak at -220 mV and a shoulder at -360 mV can be seen in the curve which has been recorded at $\tau = 2$ ms. At step times between 5 and 20 ms two well pronounced peaks are visible. The peak currents at -220 mV decrease more strongly with increasing step time than those attributed to the peak at -360 mV. Only the peak at -360 mV is observed at large step times (50–400 ms). By contrast, only one peak (see Fig. 6.2) is observed at all step times in the voltammograms recorded at 1350°C. A shoulder can additionally be seen at less negative potential at a step time of 2 ms.

The current-potential curves have been deconvoluted using experimentally recorded matrix currents and theoretical current-potential curves which are calculated by the procedure described in Ref. [69]. The deconvolution procedure is illustrated in Fig. 6.3. Curve 1 presents a voltammogram which has been recorded in a glass melt doped
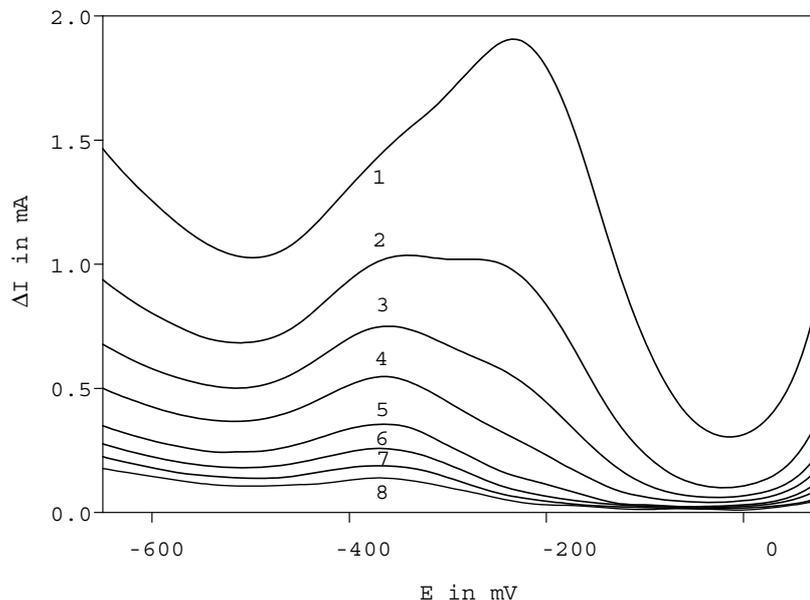
Figure 6.1: Square-wave voltammograms recorded in the melt 20 Na$_2$O ·
80 SiO$_2$ doped with 0.25 mol% SnO$_2$ at 1100°C. 1: $\tau = 2$ ms, 2: $\tau = 5$ ms,
3: $\tau = 10$ ms, 4: $\tau = 20$ ms, 5: $\tau = 50$ ms, 6: $\tau = 100$ ms, 7: $\tau = 200$ ms,
8: $\tau = 400$ ms.

with 0.25 mol% SnO$_2$ at a temperature of 1100°C and a step time of 5 ms. Curve
2 shows a voltammogram recorded in a glass melt without any additional polyvalent
element, curve 3 shows the difference of curve 1 and curve 2. The difference curve is
approximated by two calculated current potential curves (curve 4a and 4b) by using a
least square fit (assuming diffusion controlled reactions). The sum of the curves 4a and
4b is shown in curve 4, which is in good agreement with curve 3. The peak currents
which have been obtained from curve 4a and 4b (1100°C) and the peak current which
have been obtained from the peak at 1350°C are plotted as a function of $\tau^{-1/2}$ in Fig.
6.4. As it should be observed for a fully reversible electrode reaction, the peak currents
from the peaks at -360 mV (1100°C) and at -221 mV (1350°C) are proportional to $\tau^{-1/2}$
for step times larger than 20 ms and 2 ms, respectively. By contrast, the currents
attributed to the peak at -220 mV (1100°C) are not proportional to $\tau^{-1/2}$. That is,
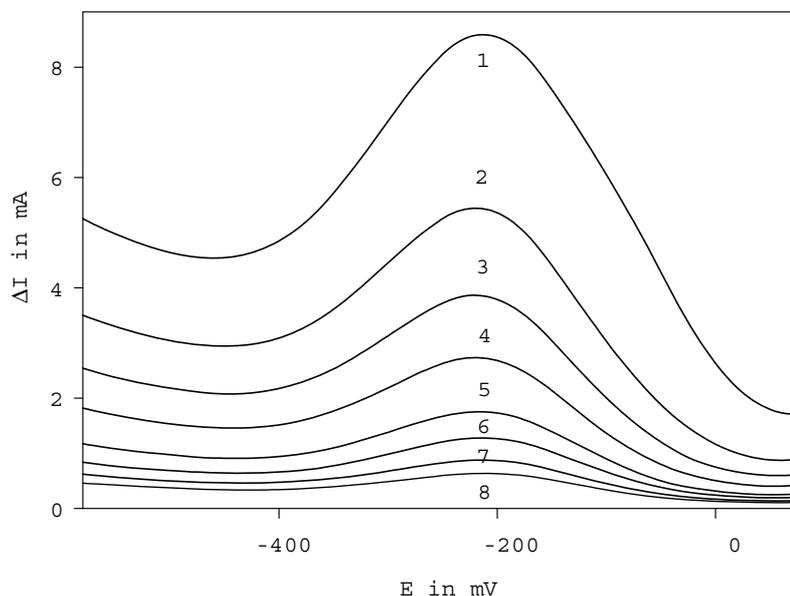the peak currents decline more strongly with increasing $\tau^{-1/2}$ than expected for an

Figure 6.2: Square-wave voltammograms recorded in the melt 20 $Na_2O \cdot$ 80 SiO_2 doped with 0.25 mol% SnO_2 at 1350°C. 1: $\tau = 2$ ms, 2: $\tau = 5$ ms, 3: $\tau = 10$ ms, 4: $\tau = 20$ ms, 5: $\tau = 50$ ms, 6: $\tau = 100$ ms, 7: $\tau = 200$ ms, 8: $\tau = 400$ ms.

electrode reaction controlled by diffusion.

In Fig. 6.5 square-wave-voltammograms of the melt 20 $Na_2O \cdot 80$ SiO_2 are shown at different temperatures at a step time of 5 ms. At high temperatures the less negative peak is only visible as a shoulder. With decreasing temperature this shoulder becomes more and more pronounced. At 900° and 1000°C, the shoulder appearing at less negative potentials has changed to a peak and the peak at more negative potential has diminished. In general, the appearance of two peaks is observed in the temperature range from 900° to 1250°C and shorter step times (i.e. 2 ms at 1250° and 2–20 ms at 1100°C). The behaviour described above has already been reported by G. von der Gönna [70].
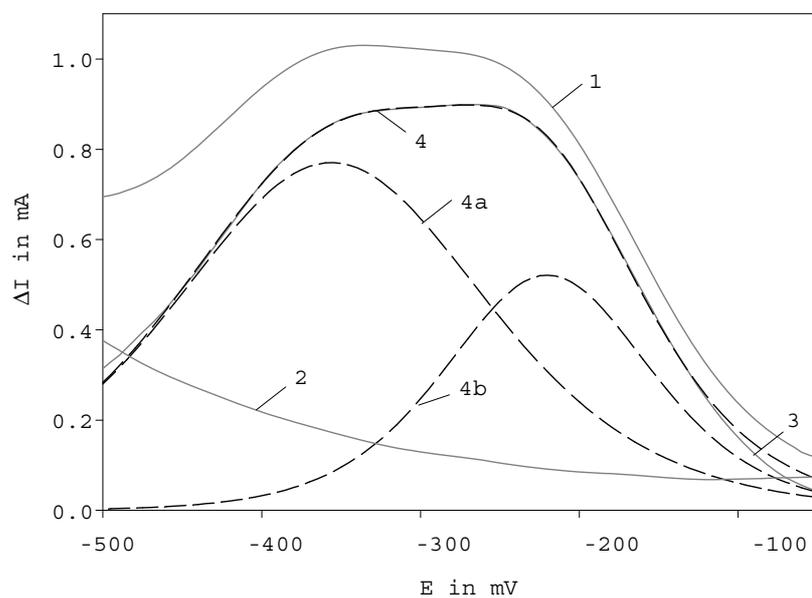
Figure 6.3: Square-wave voltammograms recorded in the melt 20 Na$_2$O · 80 SiO$_2$ doped with 0.25 mol% SnO$_2$ at 1100°C and $\tau = 5$ ms (curve 1) and in a melt without polyvalent ions (curve 2). Curve 3 = curve 1 - curve 2, curves 4a and b: calculated current-potential curves. Curve 4 = curve 4a + curve 4b.
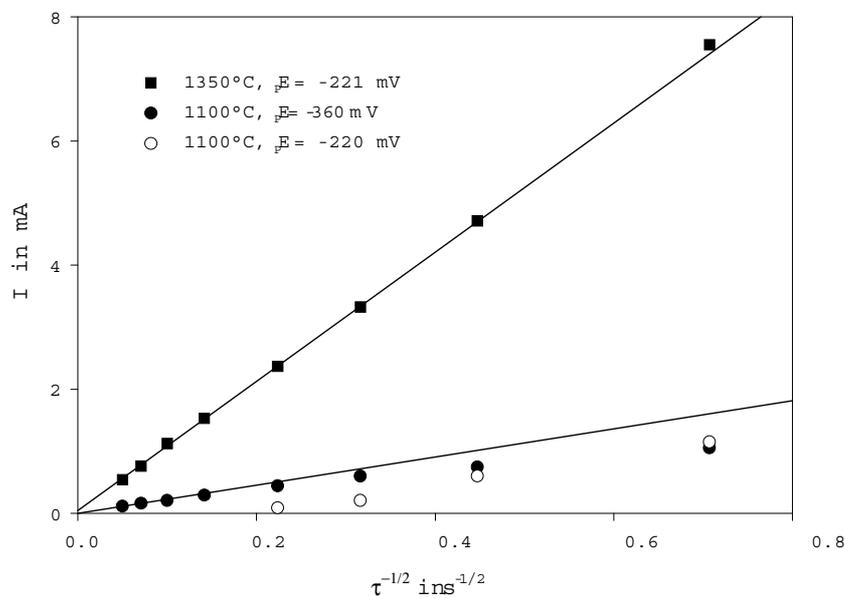

Figure 6.4: Peak currents as a function of $\tau^{-1/2}$ recorded in the melt 20 Na$_2$O · 80 SiO$_2$ doped with 0.25 mol% SnO$_2$.
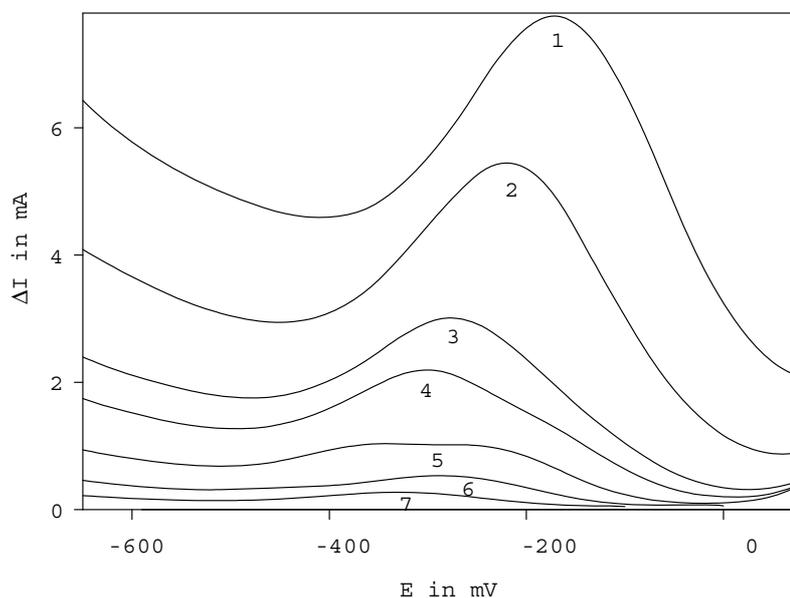
Figure 6.5: Square-wave voltammograms recorded in the melt 20 $Na_2O \cdot$ 80 SiO_2 doped with 0.25 mol% SnO_2 at $\tau = 5$ ms at different temperatures. 1: 1450°C, 2: 1350°C, 3: 1250°C, 4: 1200°C, 5: 1100°C, 6: 1000°C, 7: 900°C.
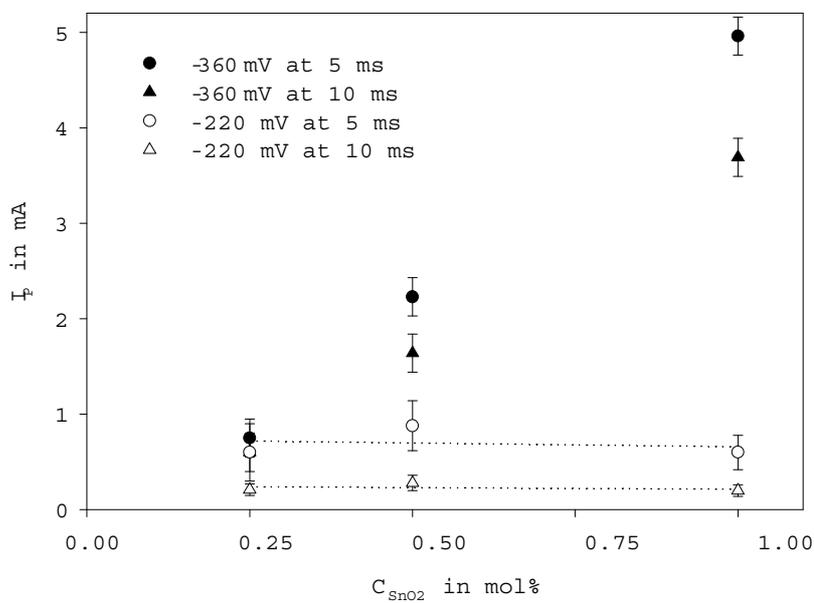
Figure 6.6: Peak currents of melts 20 $Na_2O \cdot$ 80 SiO_2 as a function of the SnO_2 concentration at 1100°C.

6.2 SWV as a function of the SnO_2 concentration in the melt 20 $Na_2O \cdot 80$ SiO_2

SWV measurements have been carried out in the melt 20 $Na_2O \cdot 80$ SiO_2 doped with different SnO_2 concentrations using the same immersion depth of the working electrode in order to enable the direct comparison of the peak currents. Figure 6.6 shows the peak currents of the melt 20 $Na_2O \cdot 80$ SiO_2 as a function of the SnO_2 concentration at 1100°C and at step times of 5 and 10 ms. The peak currents attributed to the peak at -360 mV increase linearly within the investigated concentration range. However, those attributed to the peak at -220 mV are constant within the limit of error with increasing SnO_2 concentration.

6.3 EIS in the melt 20 $Na_2O \cdot 80$ SiO_2

Figure 6.7 shows impedance spectra recorded at 1350°C by using different dc-potentials. The spectra show the absolute values of the impedance $|Z|$ and of the phase angle $|\varphi|$. The absolute value of the phase angle, which is recorded at a dc-potential of 100 mV (curve 1), increases from 38° at a frequency of $10^{-2}s^{-1}$ up to a maximum of 63° at a frequency of 72 s^{-1}. At further increasing frequencies the absolute phase angle decreases down to a minimum at $2 \cdot 10^4$ s^{-1}. At frequencies higher than $2.3 \cdot 10^4$ s^{-1} an increase of the absolute phase angle is again observed. This is result of an inductance caused by the wiring. At a dc-potential of -241 mV (curve 2), the absolute phase angle increases from 40°, at a frequency of 10^{-2} s^{-1}, up to a maximum of 44°, at a frequency of 1 s^{-1}. The high frequency has approximately the same shape as curve 1. Curve 3 shows an impedance spectrum which has been recorded using a dc-potential of -700 mV. Here, the absolute phase angle is quite smaller at a frequency of 10^{-2} s^{-1} and takes a value of 15°. The maximum ($|\varphi| = 39°$) is observed at a frequency of 7 s^{-1}. The high frequency part differs from the spectra described above. The minimum is

Figure 6.7: Impedance spectra recorded at 1350°C by using different dc-potentials. a: absolute values of the impedance, b: absolute values of the phase angle. 1: 100 mV, 2: -241 mV, 3: -700 mV.
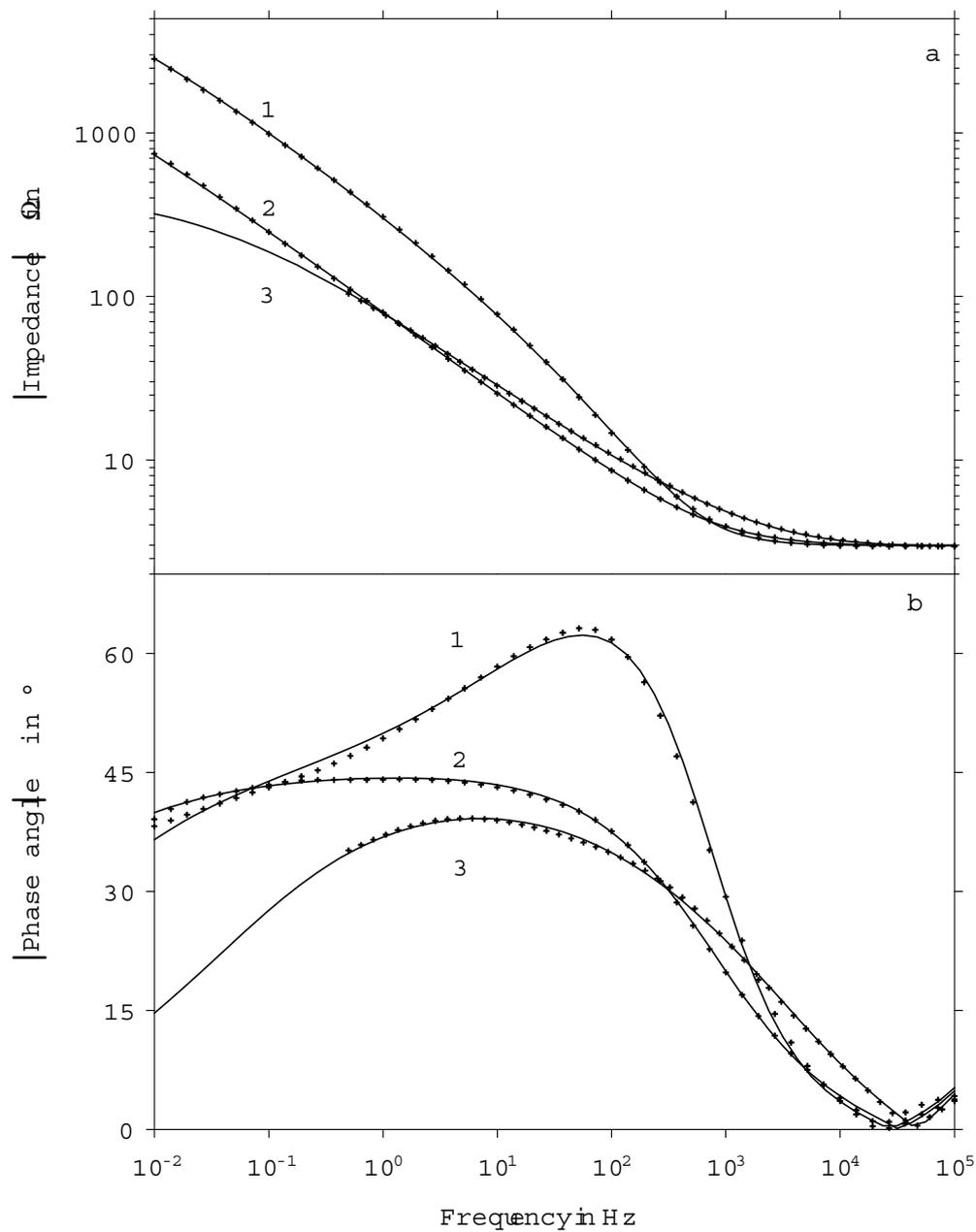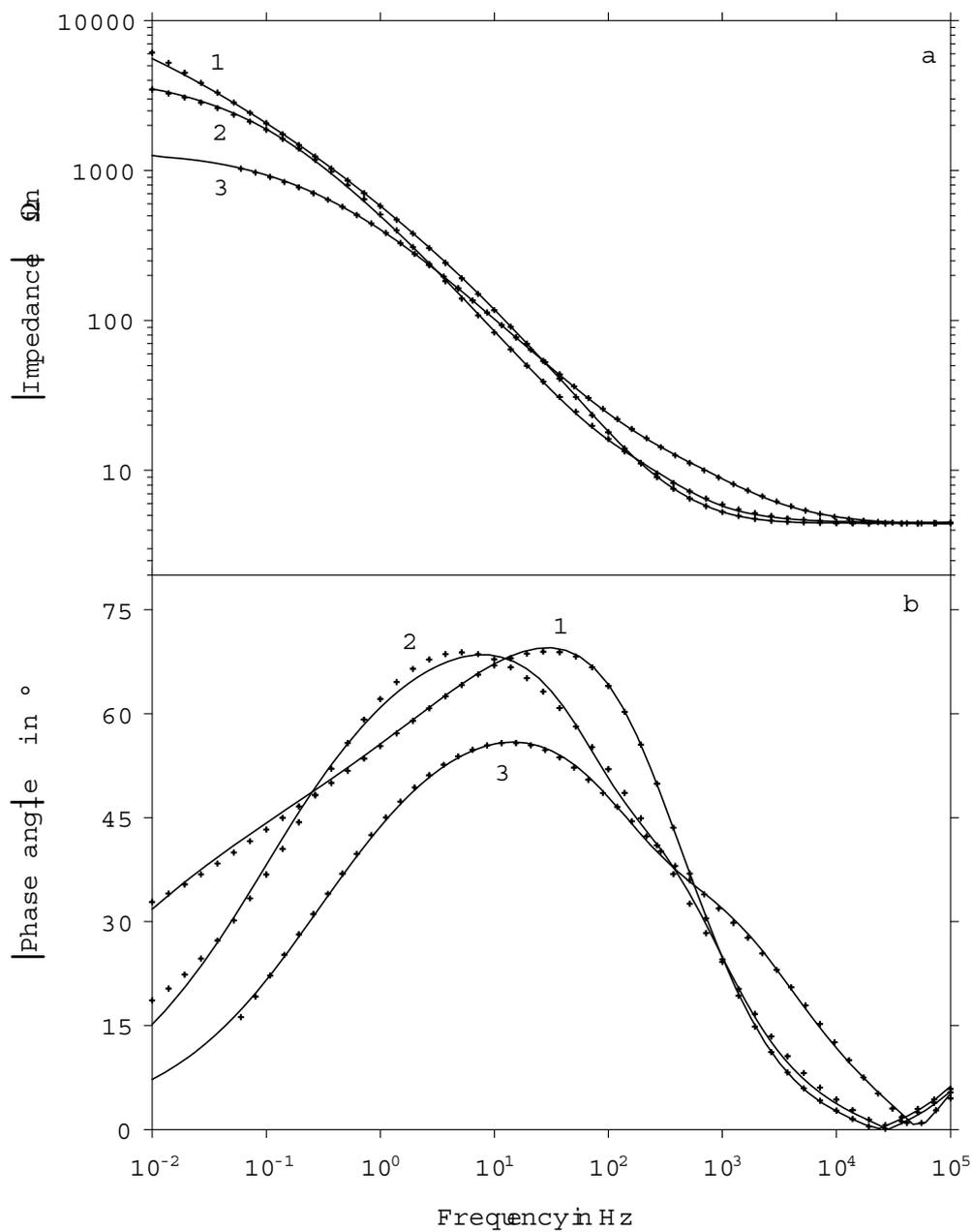
Figure 6.8: Impedance spectra recorded at 1100°C by using different dc-potentials. a: absolute values of the impedance, b: absolute values of the phase angle. 1: 100 mV, 2: -241 mV, 3: -641 mV.
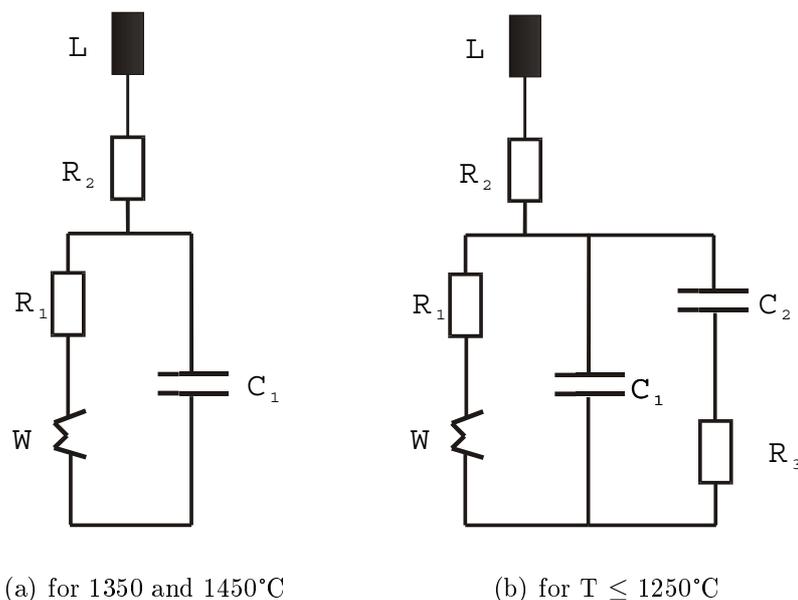
(a) for 1350 and 1450°C   (b) for T ≤ 1250°C

Figure 6.9: Equivalent circuits used for the simulation of the impedance spectra.

shifted to a frequency of $5 \cdot 10^4$ s^{-1}.

In Fig. 6.8, the impedance spectra are shown for a temperature of 1100°C. At dc-potentials from -141 mV to -262 mV (see curve 2) and from -561 mV to -700 mV (see curve 3), the shape differs from those shown in Fig. 6.7. Two shoulders are visible in the Bode plot.

The impedance spectra at 1350°C (see Fig. 6.7) and 1450°C have been simulated using an equivalent circuit shown in 6.9(a). Good agreement (within the limits of error) of the simulated spectra with the experimental ones has been obtained, as shown, by the solid lines belonging to the simulation. The Warburg impedance W, the resistance R_2 and the double layer capacitance C_1 —as received by the simulation of the impedance spectrum— are plotted as a function of the dc-potential in Fig. 6.10. (The Warburg W is corrected by spherical geometry, however only the Warburg parameter is interpreted.) The value of the resistance R_2 is nearly constant ($2.99\pm0.08\Omega$), whereas that of the resistance R_1 is < 0.2 Ω and not significantly different from 0. The Warburg impedance has a pronounced minimum at -225 mV. The double layer capacitance C_1 shows a
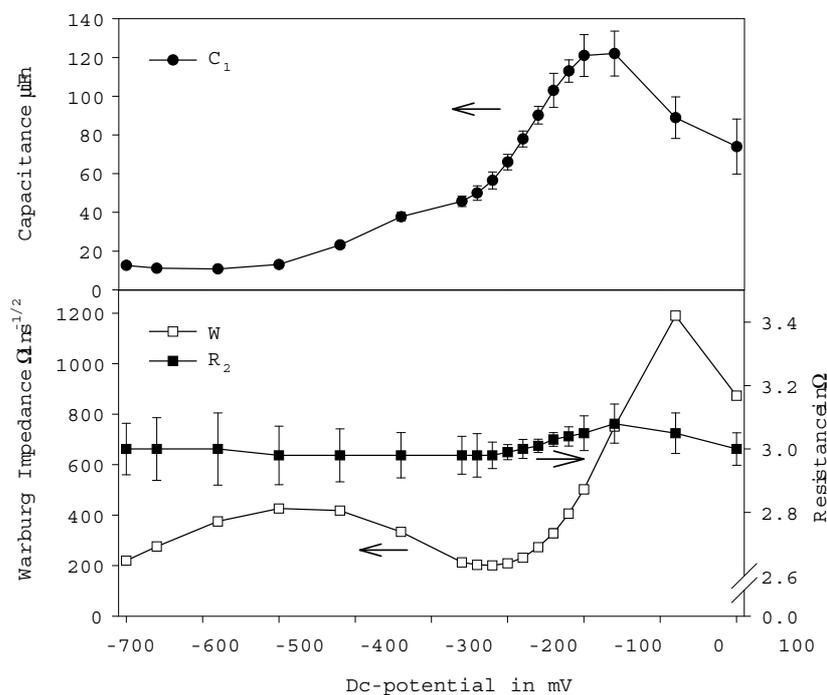
Figure 6.10: Warburg impedance, resistance R_2 and double layer capacitance C_1 as a function of the dc-potential at 1350°C.

maximum of 122 μF at -60 mV.

It was not possible to simulate the spectra at temperatures ≤ 1250°C (see Fig. 6.8) by using the equivalent circuit shown in 6.9(a). Hence, a more complex circuit has been employed (see 6.9(b)). In this case, the resistance R_3 and the capacitance C_2 have been added. As shown by the full lines in Fig. 6.8, the simulated curves are in agreement with the measured data in the frequency range from 10^{-2} to 10^5 s^{-1}. Figure 6.11 shows the Warburg impedance W, bulk electrolyte resistance R_2, double layer capacitance C_1, adsorption capacitance C_2 and resistance R_3 as a function of the dc-potential at 1100°C. In analogy to the measurement at 1350°C, the Warburg impedance W has a minimum at -360 mV at 1100°C. The resistance R_1 is not significantly different from 0. The resistance R_2 is slightly increasing from 4.32 to 4.54$\pm$0.17 Ω. The resistance R_3 shows a maximum of 55 Ω at -560 mV and is decreasing at lower and at higher dc-potentials
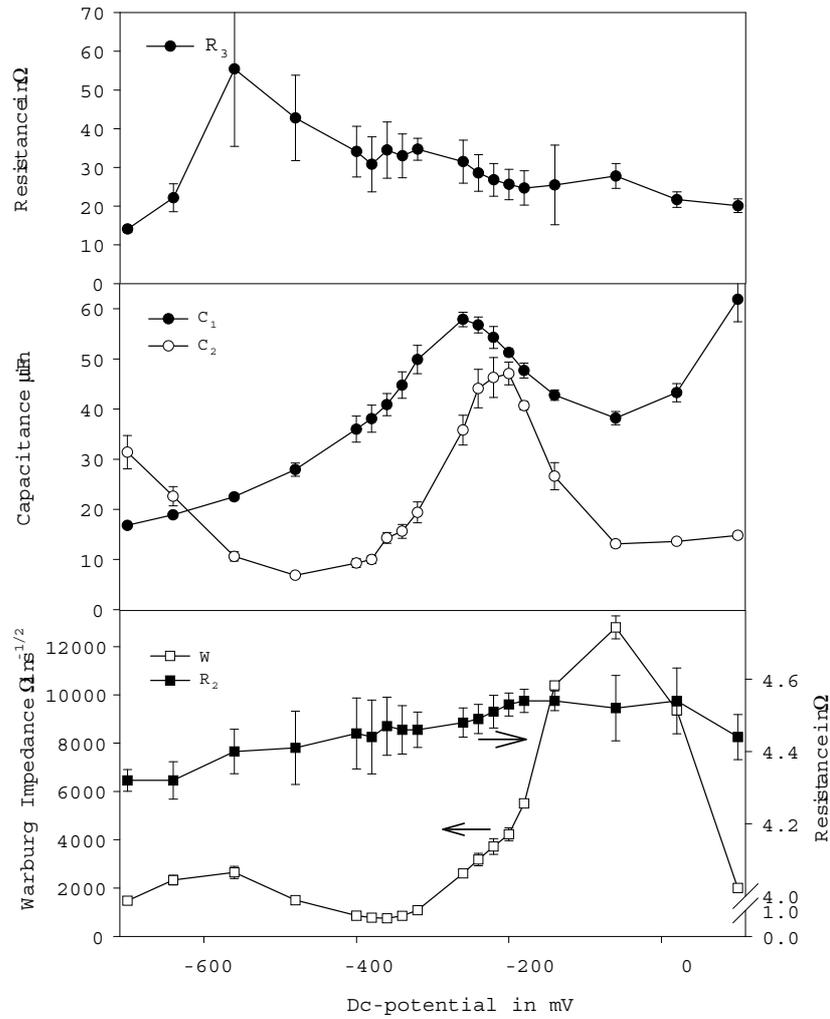
Figure 6.11: Warburg impedance, resistance R_2, double layer capacitance C_1, adsorption capacitance C_2 and resistance R_3 as a function of the dc-potential at 1100°C.
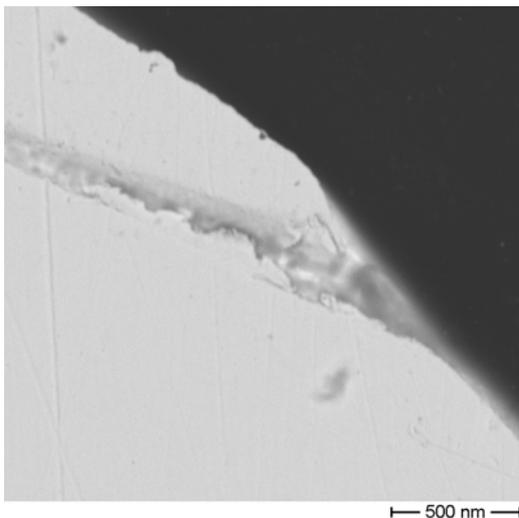
Figure 6.12: SEM image of a section of the working electrode

to $\sim 20\ \Omega$. C_1 has a maximum value of 58 μF at -260 mV and C_2 of 47 μF at -210 mV.

6.4 Electrolysis in the melt 20 Na$_2$O $\cdot$ 80 SiO$_2$

The applied potential (-318 mV, 20 hours, 1350°C) is in the range of the left flank of the peak which is observed at more negative potentials in SWV (see Fig. 6.2). In this potential range, the amount of the oxidised species has already diminished. In this way, a large quantity of the reduced species is formed during electrolysis. The reduced species could be either Sn^{2+} or metallic tin. On the other hand, if metallic tin is formed, a platinum/tin alloy should be generated [71]. However, if metallic tin is present, it can be detected by analytical methods.

SEM imaging and WDX-analysis of the working electrode

By scanning electron microscopy (SEM), it has been shown that small cracks and holes are visible on the electrode surface. In Fig. 6.12 a distinct crack is shown on a section of the working electrode which has been exposed to the melt. WDX-analyses have been

carried out on the surface close to the cracks and inside of the cracks. On no account tin has been detected, neither on the surface which has been exposed to the glass nor inside or next to the cracks and holes. 1.44±0.01 mol% SiO_2 and 4.48±0.09 mol% ZrO_2 have been detected near the cracks and holes. ZrO_2 inclusions are due to the reference electrode which dissolves at high temperature and long working time due to the high alkaline concentration present in the glass melt.

6.5   Assignment of voltammetric peaks

As mentioned earlier in the Introduction, tin might occur in the oxidation states Sn^{4+}, Sn^{2+} and Sn^0. That is, two characteristic peaks might in principle be observable in the voltammograms:

$$Sn^{4+} \overset{2e^-}{\rightleftharpoons} Sn^{2+} \quad \text{and} \quad Sn^{2+} \overset{2e^-}{\rightleftharpoons} Sn^0 \tag{6.1}$$
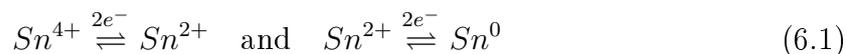
Hence, the question arises to which of the two redox pairs (see Eq. (6.1) the two observed peaks are assigned.

As shown in Fig. 6.4 the currents due to the peak at -221 mV (1350°C) and -360 mV (1100°C) are proportional to $\tau^{-1/2}$. This is expected for an electron transfer reaction controlled only by diffusion (see Eq. (3.13) and Ref. [42, 43]). However, the currents which are attributed to the peak occurring at less negative potentials are not corresponding to Eq. (3.13). Consequently, it is not possible to explain the occurrence of the peak which appears at less negative potentials by a simple electron transfer reaction controlled by diffusion.

At temperatures at which only one peak is visible in the SWV voltammograms, the impedance spectra (1350 and 1450°C) have been simulated by a quite simple equivalent circuit (Fig. 6.9(a)): The Warburg impedance W is the partial impedance element which accounts for a diffusion controlled reaction. A kinetic hindrance is not observed
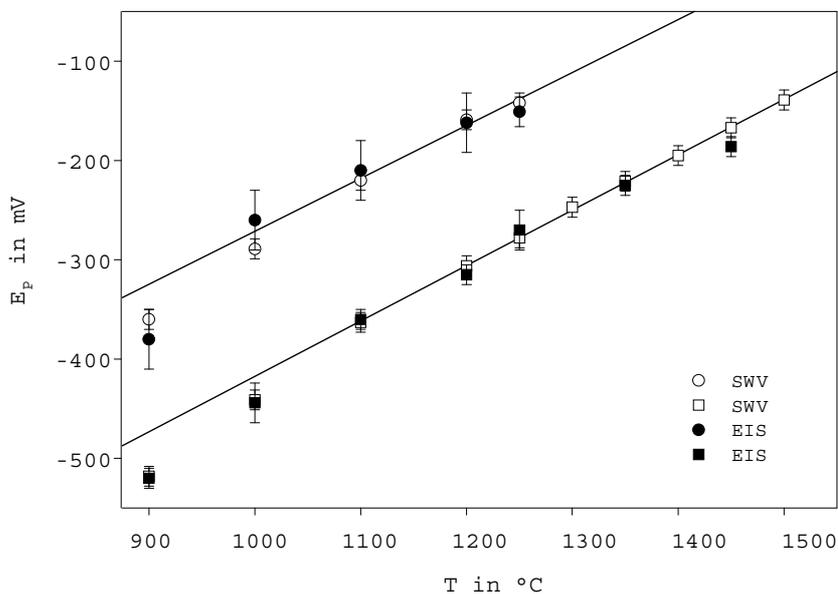
Figure 6.13: Potential as a function of the temperature determined by SWV and EIS.

because the resistance R_1 describing this phenomenon is 0. For this reason, the electrode reaction is only controlled by diffusion. According to Macdonald and Johnson [72], the Warburg impedance should have a minimum at the standard potential of the present redox pair. Indeed, well pronounced minima are observed in the graph Warburg impedance vs. potential (see Fig. 6.10). The potentials at which these minima appear are in good agreement with the peaks which are observed in SWV at the respective temperatures (see Fig. 6.13). As a result of this, the minima in the Warburg impedance-dc-potential dependency and the peak potentials observed by SWV should be attributed to the same electrode reaction.

At temperatures ($< 1300°C$) a second peak appears in the voltammograms. Here, the simple equivalent circuit (Fig. 6.9(a)) does not allow an accurate fit of the experimental data. This is why the impedance spectra at temperatures $< 1300°C$ have to be simulated with a more complex equivalent circuit (Fig. 6.9(b)). In analogy to the equivalent circuit which has been used for the simulation at higher temperatures, the minima in the Warburg impedance-dc-potential dependency have been assigned to the

peak having currents which are proportional to $\tau^{-1/2}$. As it can be seen in Fig. 6.13, the potentials which are obtained by the minima in the Warburg impedance-dc-potential dependency and by SWV are in agreement. The peak at less negative potentials is neither in agreement with Eq. (3.13) (see above) nor can it be attributed to a second Warburg impedance in the equivalent circuit (Fig. 6.9(b)). Hence, the appearance of this peak is not resulting from a diffusion controlled reaction. An electron transfer reaction is proposed in which an adsorbed state is involved. The adsorption of tin on platinum electrodes has already been observed by other authors who have studied diluted tin solutions by dc- and ac-voltammetry [73] and cyclic voltammetry [74].

In general, adsorption phenomena correspond to an equivalent circuit consisting of an "adsorption resistance" —determined by the rate of adsorption, an "adsorption capacitance" and a Warburg impedance —corresponding to diffusion of the surface reactants. According to Retter and Lohse [75], three different cases of adsorption kinetics occur: First, diffusion controlled kinetics, second, kinetics controlled by the adsorption exchange rate and third, a mixed control by diffusion and adsorption exchange. Consequently, in the equivalent circuit (Fig. 6.9(b)) the capacitance C_2 accounts for the adsorption capacitance and the resistance R_3 is the equivalent impedance element for the hindrance of the electron transfer from the adsorbed state. A Warburg impedance is not present within this branch. As a result of this, the adsorption exchange rate is the rate determining step. The adsorption capacitance C_2 has a strong dependency on the dc-potential, as already described in section 6.3 (see Fig. 6.11). According to Retter and Loser [75], a capacitance which is mainly determined by the potential dependency of the degree of coverage leads to the occurrence of maxima in the capacitance-potential dependency. The potentials which are observed at the maxima in the capacitance-dc-potential dependency are in good agreement with the potentials of the peak determined by SWV at less negative potentials (see Fig 6.13).

Now the question arises: to which of the two possible redox pairs (see above and Eq. (6.1)) the electrode reaction solely controlled by diffusion can be assigned. Assuming

an assignment to the Sn^{2+}/Sn^0-redox pair, metallic tin should be formed at the applied electrolysis potential. Since metallic tin and platinum form an alloy [71], it should be possible to detect metallic tin in case it is really formed. However, tin has not been detected in the working electrode by means of WDX-analyses (after electrolysis at -317 mV) (see section 6.4). Thus, it seems reasonable to assume that the observed electrode reaction is assigned to the redox pair Sn^{4+}/Sn^{2+}. This result is further confirmed by Mössbauer measurements (see section 8.1.1). By means of Mössbauer spectroscopy of quenched samples, it has been shown that only Sn^{2+} and Sn^{4+} are present in the composition 20 $Na_2O \cdot 80$ SiO_2.

However, an adsorbed state is involved in the electrode reaction. Since the potential attributed to the adsorbed state is less negative than that of the peak assigned to the diffusion controlled reduction —it is necessary to overcome the Gibbs energy of adsorption [76] and the adsorption of Sn^{2+} is energetically favoured. Due to the lack of diffusion controlled currents, Sn^{4+} is supposed to be absorbed as well.

The surface concentration of the adsorbed tin species $\Gamma = 18 \pm 5 \cdot 10^{-10}$ mol·cm^{-2} has been determined by using the amount of substance n and the area A of the immersed working electrode. The amount of substance n has been calculated by the second Faraday´s law of electrolysis:

$$\Gamma = \frac{n}{A} \qquad \text{with} \qquad n = \frac{Q}{z \cdot F} \qquad (6.2)$$

with Q being the charge, z the charge of the ion and F the Faraday constant. The charge has been determined from the area (charge) under the simulated curve (SWV) which is attributed to the adsorbed state. Mandler and Bard [74] have found by means of cyclic voltammetry that tin(II)chloride in aqueous solution was adsorbed on gold, forming a monolayer ($\Gamma = 6.8 \cdot 10^{-10}$ mol·cm^{-2}). The surface covering of tin(IV)chloride was at least 20-25 times smaller than that of tin(II)chloride. This is in agreement with the result of this work. The larger surface concentration Γ for SnO is due to its smaller cell parameters (SnO: a = 3.804 Å, c = 4.826 Å [77]; SnCl$_2$: a = 7.793 Å, b

= 9.207 Å, c = 4.430 Å [78]). Thus, the observed peak at less negative potential can be attributed to a monolayer of adsorbed SnO_x. This is confirmed by the fact that the peak current assigned to the adsorbed species does not increase as a function of the SnO_2 concentration. It is remarkable that adsorption of SnO_x on a Pt-electrode at high temperatures has been shown with this investigation for the first time.

Furthermore, it should be noted that a further increase in the Warburg impedance is not observed at potentials < -600 mV (1100°C) and a decrease is visible at potentials > -60 mV . These potentials are shifted, as observed by the minima in the Warburg-potential dependency, with increasing temperature to more positive values. This is not surprising because in SWV an increase in the current is also observed at potentials < -550 mV (at 1100°C see Fig. 6.1). This occurs in any silicate glass and can be explained by the decomposition of the silicate network. Elemental silicon or platinum silicide are formed at the platinum electrode. An increase in current is also observed at potentials > -20 mV which is due to the oxidation of the glass matrix to gaseous O_2 [7].

Chapter 7

Electrochemical measurements

7.1 Thermodynamic data

7.1.1 Alkali- and alkali alkaline-earth-silicate melts

Figure 6.5 shows square-wave voltammograms which have been recorded in the melt 20 $Na_2O \cdot$ 80 SiO_2 doped with 0.25 mol% SnO_2. The peak observed at more negative potential is assigned to the Sn^{4+}/Sn^{2+}-redox pair. The electrode reaction is diffusion controlled (see section 6.5). The peak observed at more positive potential is not further discussed in the following chapters. However, the peak attributed to the redox pair Sn^{4+}/Sn^{2+} strongly depends on temperature. The peak potential is observed at -167 mV at a temperature of 1450°C. The peak is continuously shifted to more negative potentials with decreasing temperature. A peak potential of -360 mV is observed at a temperature of 1100°C. A strong decrease in current is simultaneously observed, which is caused by the decreasing mobilities at lower temperatures (see section 7.4).

Voltammograms of all studied silicate melt compositions exhibit a shape similar to that presented in Fig. 6.5.

The peak potentials for the glasses: x $Na_2O \cdot$ (100 - x) SiO_2 with x = 15, 20, 26, 33 as a function of temperature are shown in Fig. 7.1. The data for x = 15 and 33 were taken
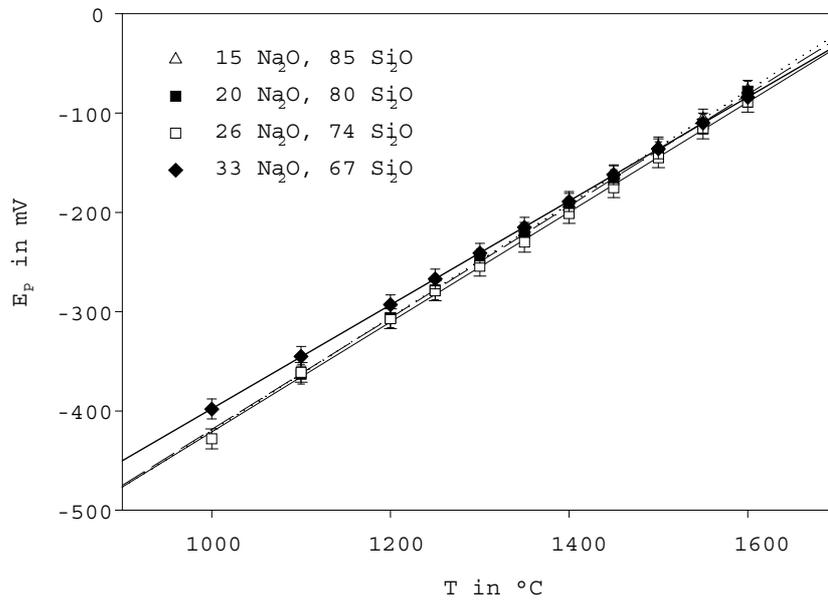
Figure 7.1: Peak potentials as a function of temperature for soda-silicate melts. Data for $[Na_2O] = 15, 33$ by G. von der Gönna [70].
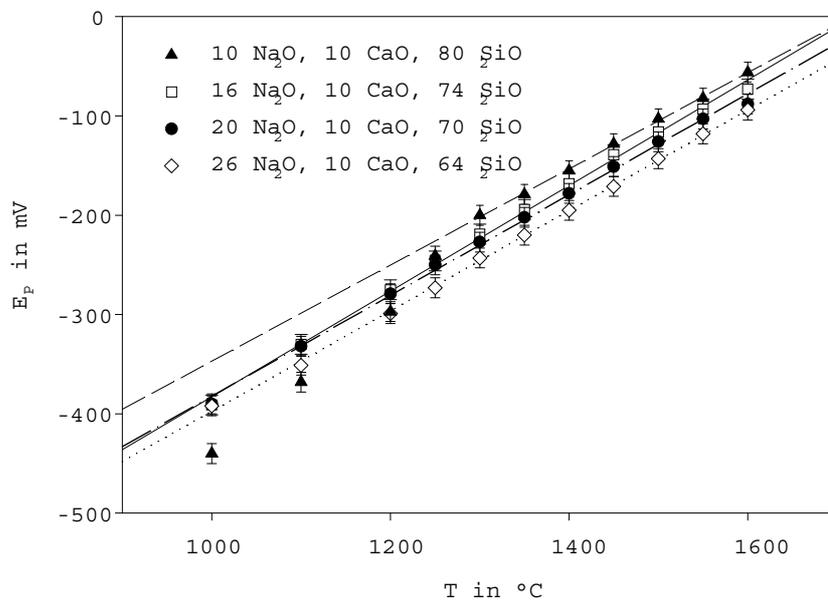

Figure 7.2: Peak potentials as a function of temperature for soda-lime-silicate melts.

from Ref. [70]. For the composition 15 $Na_2O \cdot 85 SiO_2$, peak potentials are plotted only for temperatures $\geq$ 1350°C because cristobalite crystallisation has occurred at lower temperatures [70]. Figure 7.2 shows the temperature dependent peak potentials for the glasses: x $Na_2O \cdot 10 CaO \cdot (90 - x) SiO_2$ with x = 10, 16, 20, 26.

Notable deviations of the peak potential from linearity are observed for the glass 20 $Na_2O \cdot 80 SiO_2$ at temperatures $\leq$ 1000°C (Fig. 7.1) and for the glass 10 $Na_2O \cdot 10 CaO \cdot 80 SiO_2$ at temperatures $\leq$ 1300°C (Fig. 7.2). On the other hand, the potentials for the other compositions depend linearly on temperature in the entire temperature range (1000°–1600°C). The linear correlation between the peak potential and the temperature observed for all compositions at temperatures higher than 1350°C allow for the determination of the standard enthalpies ΔH^0 and standard entropies ΔS^0, according to Eqs. (3.7) and (3.8). Thermodynamic data are summarised in Table B.1, as well as peak potentials and redox ratios, assuming equilibrium with air for the different glass compositions.

Furthermore, in Table B.1 the data for the melt 20 $Na_2O \cdot 80 SiO_2$ doped with different SnO_2 concentration are included. It is remarkable that the peak potentials and thermodynamic data are found to be independent of the dopant concentration within the limits of error.

Figure 7.3 shows voltammetrically determined peak potentials as a function of the temperature for melts with the compositions 16 $Li_2O \cdot 10 CaO \cdot 74 SiO_2$, 16 $Na_2O \cdot 10 CaO \cdot 74 SiO_2$ and 16 $K_2O \cdot 10 CaO \cdot 74 SiO_2$. For the Na_2O and K_2O containing melts, linear correlations of the peak potentials within the error limits are observed in the whole temperature range studied (1000°–1600°C or 1100°–1500°C). By contrast, a linear correlation is obtained only in the range from 1200 to 1600°C for the Li_2O containing melt. At lower temperatures significant deviations were observed. The sample was opaque after cooling. Whereas the slopes of the regression lines —shown in Fig. 7.3— for the Li_2O and the Na_2O containing melts are equal within the error limits, the slope attributed to the K_2O containing glass is notably larger.
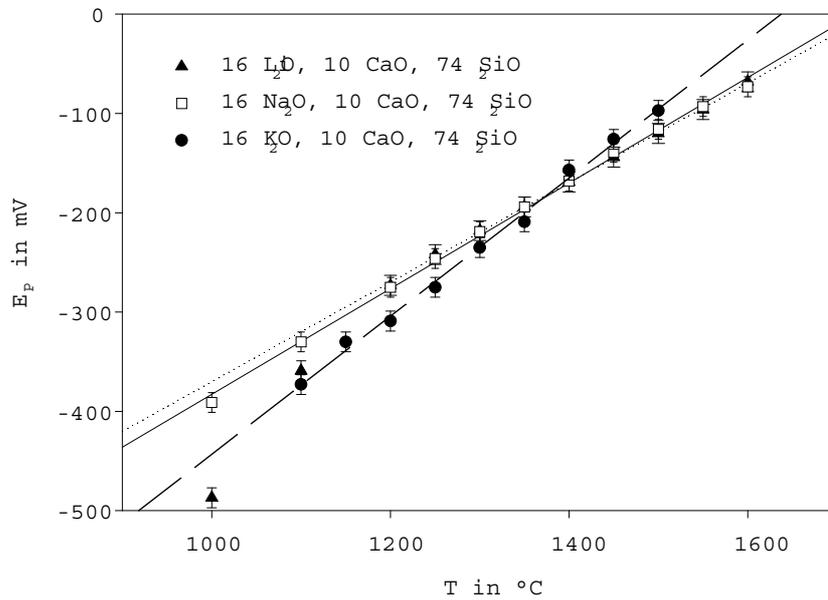
Figure 7.3: Peak potentials as a function of temperature, measured in alkali-lime-silicate melts.
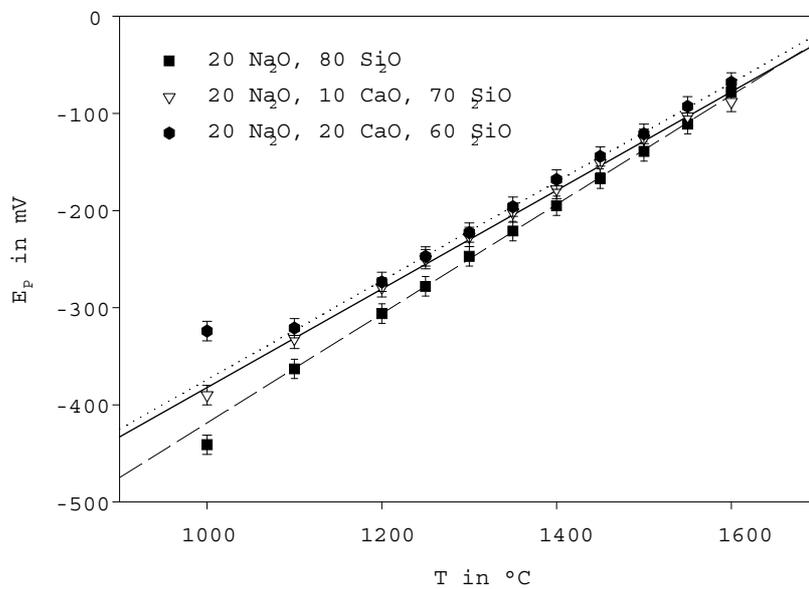

Figure 7.4: Peak potentials as a function of temperature, measured in silicate melts.
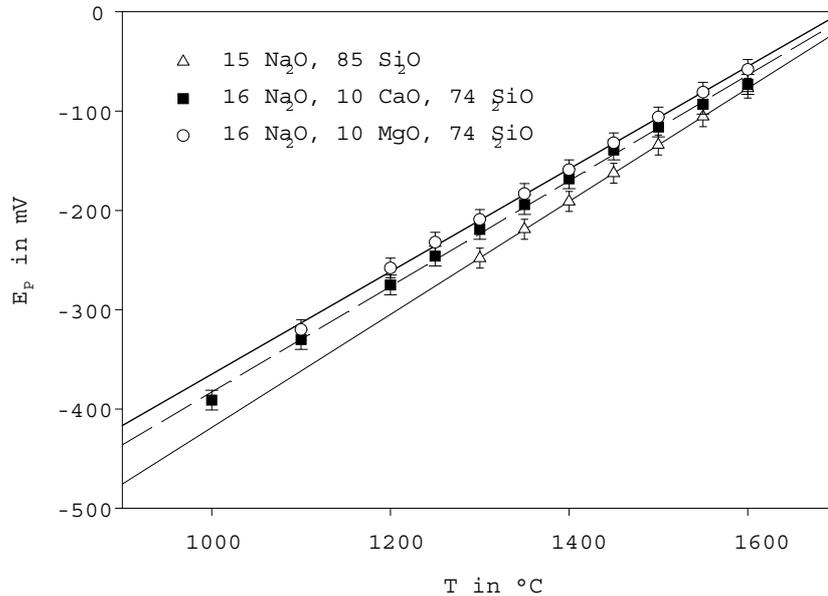
Figure 7.5: Peak potentials as a function of temperature and different alkaline earth oxides. Data for $[Na_2O] = 15$ mol% by G. von der Gönna [70].

Figure 7.4 shows peak potentials of melts containing 20 mol% Na_2O with CaO concentrations of 0, 10 and 20 mol% as a function of temperature. Linear correlations within the error limits are observed in the entire temperature range in the melts with 0 and 10 mol% CaO. Deviations from linearity are observed at 1000°C in the melt with 20 mol% CaO. The cooled down glass has shown crystals at the surface and at the interface electrode/glass.

Figure 7.5 shows peak potentials of the melts 15 $Na_2O \cdot$ 85 SiO_2, 16 $Na_2O \cdot$ 10 CaO $\cdot$ 74 SiO_2 and 16 $Na_2O \cdot$ 10 MgO $\cdot$ 74 SiO_2 as a function of the temperature. Data of the composition 15 $Na_2O \cdot$ 85 SiO_2 are taken from Ref. [70]. It should be noted that crystallisation has been observed after cooling (see above).

7.1.2 Alumosilicate melts

The voltammograms of all measured alumosilicate melt compositions show a shape similar to those presented in Fig. 6.5.
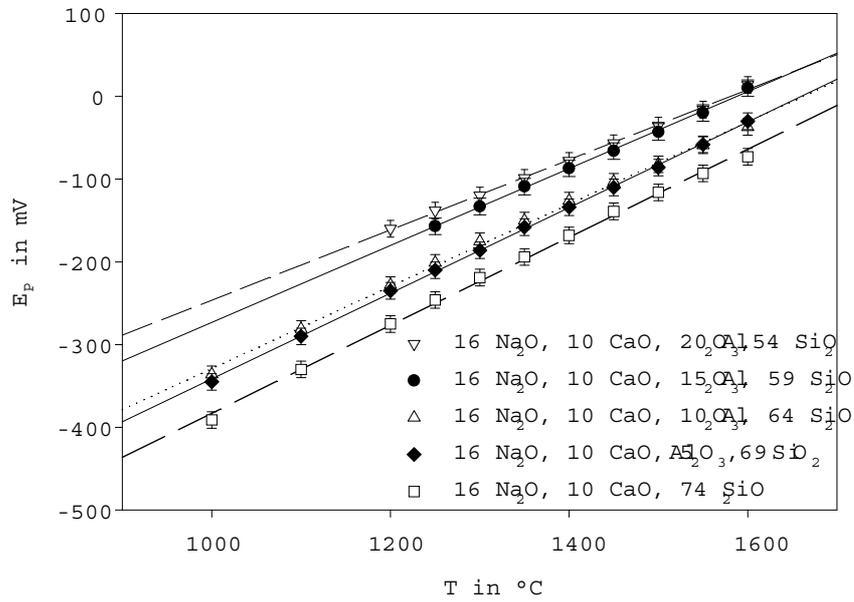
Figure 7.6: Peak potentials as a function of temperature for alumosilicate melts with 16 mol% Na_2O.
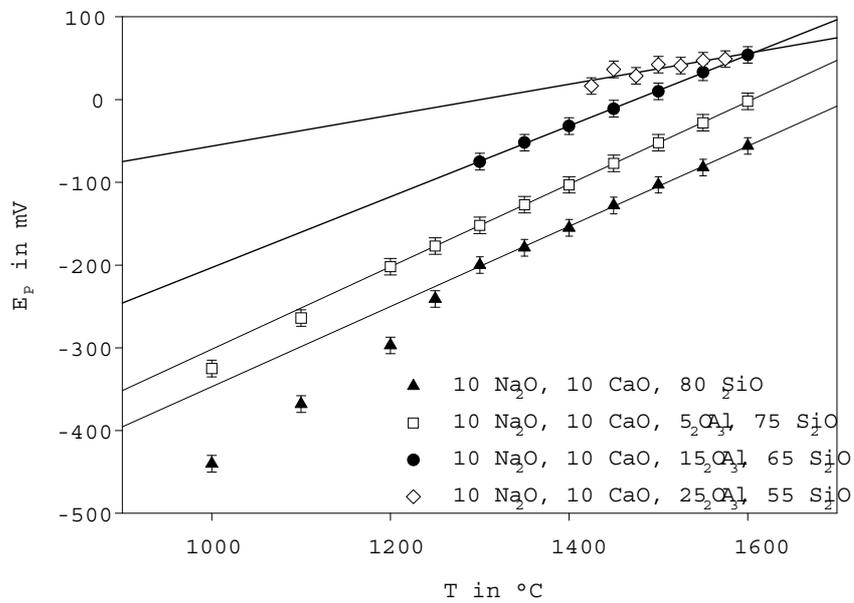

Figure 7.7: Peak potentials as a function of temperature for alumosilicate melts with 10 mol% Na_2O.

Figure 7.6 shows peak potentials as a function of temperature for the melts 16 Na_2O · 10 CaO · x Al_2O_3 · (74-x) SiO_2 with x = 0, 5, 10, 15, 20. Figure 7.7 presents peak potentials as a function of temperature for the melts 10 Na_2O · 10 CaO · x Al_2O_3 · (80-x) SiO_2 with x = 0, 5, 15, 25. For the compositions 16 Na_2O · 10 CaO · 15 Al_2O_3 · 59 SiO_2, 16 Na_2O · 10 CaO · 20 Al_2O_3 · 54 SiO_2, 10 Na_2O · 10 CaO · 15 Al_2O_3 · 65 SiO_2 and 10 Na_2O · 10 CaO · 25 Al_2O_3 · 55 SiO_2 the voltammograms have shown a more complex behaviour at lower temperatures; three peaks were present and therefore, a further evaluation has been useless at lower temperatures. The melts 10 Na_2O · 10 CaO · 80 SiO_2 and 10 Na_2O · 10 CaO · 5 Al_2O_3 · 75 SiO_2 show notable deviations from linearity. On the other hand, the potentials for the other compositions depend linearly on temperature in the entire temperature range (1000°–1600°C).

The linear correlation between the peak potential and the temperature observed for all compositions at higher temperatures allow for the determination of thermodynamic data according to Eqs. (3.7) and (3.8). Thermodynamic data as well as standard potentials and redox ratios (for an arbitrary temperature of 1300°C, assuming an equilibrium with air) are summarised for the different glass compositions in Table B.1. Here, the redox ratio and the peak potential for the melt 10 Na_2O · 10 CaO · 25 Al_2O_3 · 55 SiO_2 has been extrapolated.

7.2 Oxygen activity measurements

7.2.1 Compositions melted in air

In Figure 7.8 the oxygen activity of the glass melt 20 Na_2O · 80 SiO_2 doped with 0.5 mol% SnO_2 is presented as a function of time during variation of temperature. The oxygen activity decreases with decreasing temperature by almost two and a half orders of magnitude. At constant temperature (1200°C) the oxygen activity increases slightly. In other experiments with different glass compositions, i.e. 16 Na_2O · 10 CaO

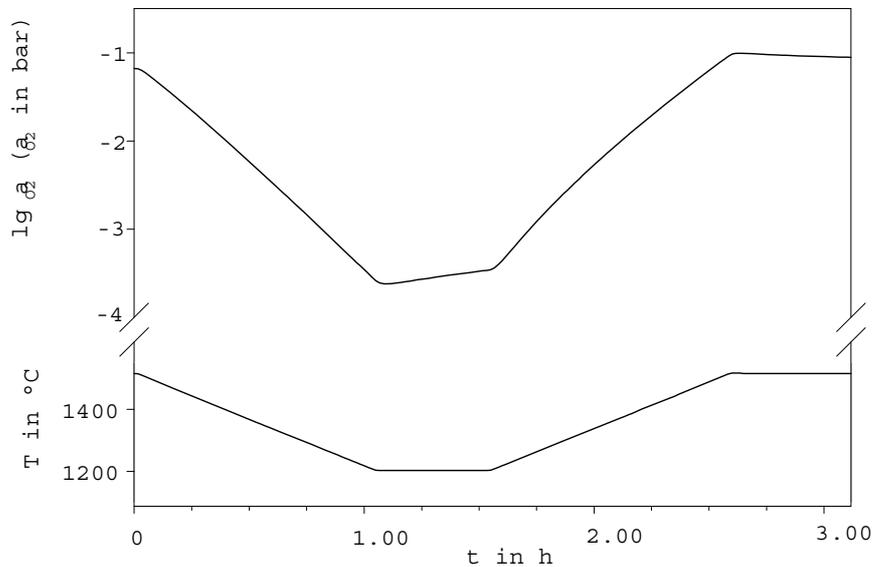Figure 7.8: Oxygen activity of the melt 20 Na_2O · 80 SiO_2 doped with 0.5 mol% SnO_2 as a function of time.

· 20 Al_2O_3 · 54 SiO_2 the oxygen activity decreases in the same temperature interval almost two orders of magnitude. For the composition 10 Na_2O · 10 CaO · 25 Al_2O_3 · 55 SiO_2 an even less pronounced decrease in the oxygen activity as a function of temperature is observed.

According to Eq. (3.16), it is possible to calculate the standard enthalpy of reaction (3.1) from the slope ln a_{O_2} vs. 1/T. The values are listed in Table B.2. Furthermore, the oxygen activities at 1300°C are included in Table B.2. The composition 20 Na_2O · 80 SiO_2 shows an oxygen activity of 0.0018, whereas the composition 16 Na_2O · 10 CaO · 20 Al_2O_3 · 54 SiO_2 shows a higher oxygen activity of 0.0127. For the composition 10 Na_2O · 10 CaO · 25 Al_2O_3 · 55 SiO_2 at temperatures < 1400°C a deviation from linearity has been observed, which has already been noted in the SWV experiment. Hence, an oxygen activity of 0.0225 at 1500°C was included in Table B.2. Using the thermodynamic standard data which are listed in Table B.1 and the oxygen activity, the redox ratios are calculated according to Eq. (3.18). It has been observed that the fraction of Sn^{2+} increases from 22% to 85% Sn^{2+} as the Al_2O_3 concentration increases.

7.2.2 Compositions melted in reducing conditions

Glass melts consisting of the compositions x Na_2O · 10 CaO · (90-x) SiO_2 with x = 10, 16, 20, 26 doped with 2 mol% SnO_2 have been melted with the addition of 0.2 wt.% C in order to obtain reducing conditions during melting. The standard reaction enthalpies, oxygen activities and the calculated redox ratios are summarised in Table B.2. At 1300°C the melts show oxygen activities ranging between 0.0004 and 0.0006. 64% Sn^{2+} are found in the melt with 10 mol% Na_2O. While increasing the Na_2O concentration, the percentage of Sn^{2+} decreases to 37%.

7.3 Discussion

7.3.1 Crystallisation and phase separation

While crystallisation or immiscibility is occurring, heterogeneous structures are formed. That means that during voltammetric experiments the composition of the melt at the surface of the working electrode is changing as the melt is cooled down below a certain temperature. Deviations from linearity have only been observed in these cases and are due to changes in the melt composition. In the following, the phenomena which have caused changes of the melt composition while performing SWV are described.

In the composition 26 Li_2O · 74 SiO_2 the crystallisation of tridymite and in the composition 33 Li_2O · 67 SiO_2 [79] the crystallisation of lithium disilicate has been observed as proved by X-ray diffraction (XRD). For the composition 20 Na_2O · 80 SiO_2 cristobalite crystallisation has occurred [80]. In the case of the 10 Na_2O · 10 CaO · 80 SiO_2 and the 16 Li_2O · 10 CaO · 74 SiO_2 glass, a crystalline phase was not detected. However, transmission electron microscopy gives evidence for phase separation. For the sample 20 Na_2O · 20 CaO · 60 SiO_2 the X-ray diffraction pattern shows distinct reflections attributable to sodium calcium silicate (JCPDS No 22-1455). For the compositions 16 Na_2O · 10 CaO · 15 Al_2O_3 · 59 SiO_2 and 16 Na_2O · 10 CaO · 20 Al_2O_3 · 54 SiO_2

Figure 7.9: Peak potentials as a function of the alkali concentration for alkali- and alkali-lime-silicate melts (T = 1300°C). Data for $[Na_2O] = 15$, 33 by G. von der Gönna [70].

crystallisation of nepheline has occurred. The crystallisation of wollastonite in the composition 10 Na_2O · 10 CaO · 5 Al_2O_3 · 75 SiO_2, the crystallisation of anorthite in the melt 10 Na_2O · 10 CaO · 15 Al_2O_3 · 65 SiO_2 and the crystallisation of corundum in the composition 10 Na_2O · 10 CaO · 25 Al_2O_3 · 55 SiO_2 have been shown by X-ray diffraction.

7.3.2 Discussion of thermodynamic data

As seen in Figs. 7.1–7.7, the peak potentials of all glasses shift to smaller potentials with decreasing temperature. This effect has been described often before and was observed in all studies of tin and other polyvalent elements [70]. Smaller peak potentials with decreasing temperature are attributed to a shift to the oxidised state, according to Eq. (3.1).

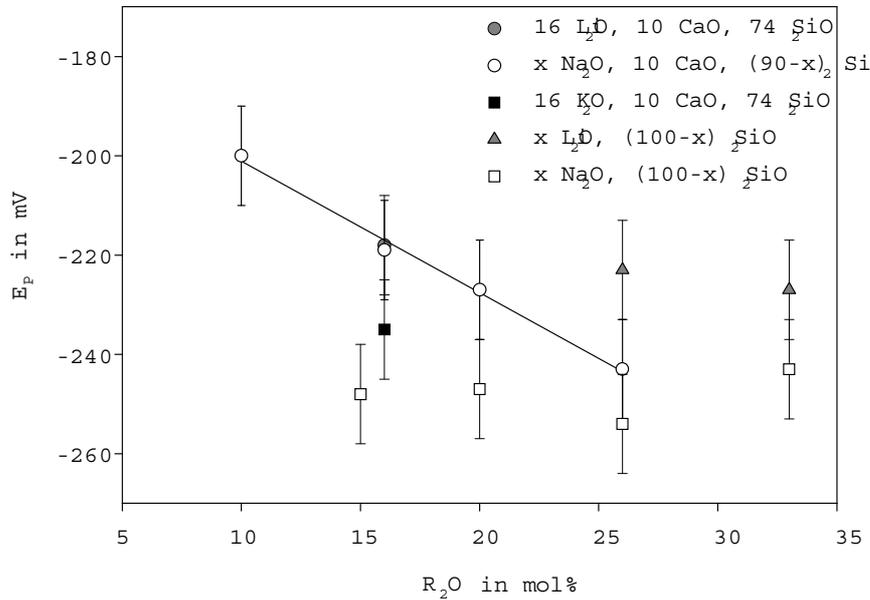Figure 7.9 presents the peak potentials measured at 1300°C as a function of the alkali
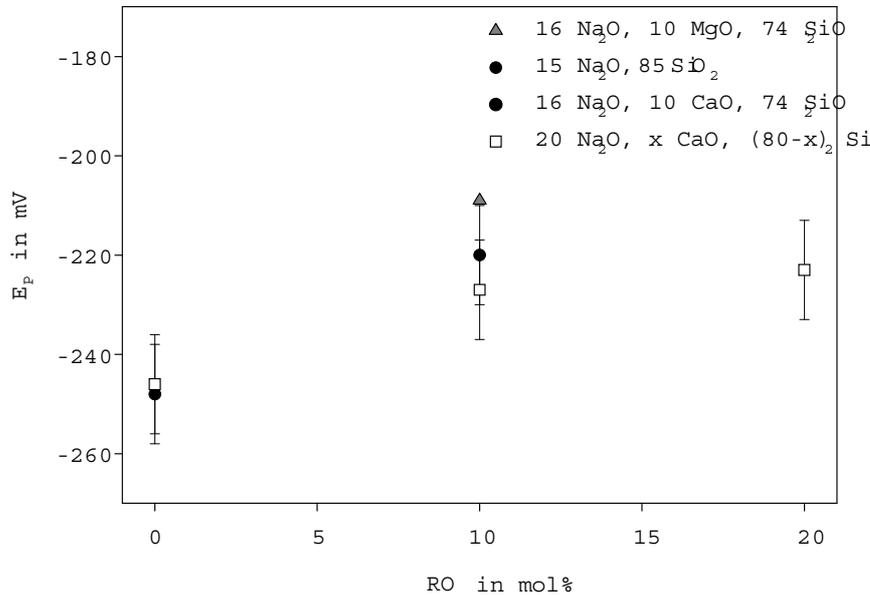
Figure 7.10: Peak potentials as a function of the alkaline earth concentration for alkali- and alkali-lime-silicate melts (T = 1300°C). Data for [Na$_2$O] = 15 mol% by G. von der Gönna [70].

concentration for alkali- and alkali-lime-silicate melts. The peak potentials measured in lithium oxide- and soda-silicate melts do not depend on the alkali concentration, i.e. they remain constant within the limits of error. Therefore, the change in the alkali concentration has no significant influence on the redox equilibrium. By contrast, for soda-lime-silicate melts, the dependency of the peak potentials on the Na$_2$O concentration is linear within the limits of error. The higher the Na$_2$O concentration, the lower the peak potentials and hence, the equilibrium, according to Eq. (3.1), is shifted to the left —i.e. to the oxidised state— with increasing alkali concentration. In alkali silicate melts a variation in the type of alkali ion, i.e. from Li to Na, leads to more negative standard potentials. Hence an increase in the size of the alkali ion generates a higher fraction of Sn^{4+}. This effect is observed in alkali alkaline earth melts as well. However, such an influence of the increasing size of the alkali ion has only been notable —in the case of Na to K— at temperatures < 1400°C.

Peak potentials measured at 1300°C as a function of the alkaline earth concentration
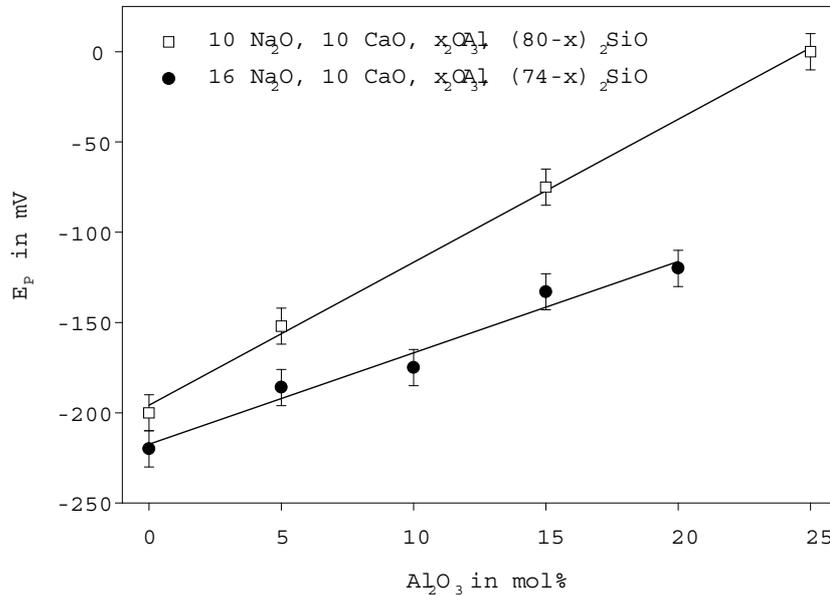
Figure 7.11: Peak potentials as a function of the Al_2O_3 concentration for alumosilicate melts containing 10 mol% Na_2O and 16 mol% Na_2O (T = 1300°C).

for alkali- and alkali-lime-silicate melts are shown in Fig. 7.10. By adding CaO to soda-silicate melts and increasing the CaO concentration, the peak potentials shift to less negative values. The effect is small, but significant. The replacement of CaO by MgO leads to less negative standard potentials. That is the equilibrium according to Eq. (3.1) shifts to the right side and the more reduced oxidation state is favoured.

Figure 7.11 presents the peak potentials measured at 1300°C for alumosilicate melts with 10 and 16 mol% Na_2O as a function of the Al_2O_3 concentration. The peak potentials move linearly —within the limits of error— to more positive values in both alumosilicate melt systems. Larger peak potentials with increasing Al_2O_3 concentration are attributed to a shift to the right side of the equilibrium according to Eq. (3.1). This means that the reduced state is favoured with increasing Al_2O_3 concentration.

The compositional effect on the tin redox equilibrium which has been found in alumosilicates is far larger than in other melt compositions such as alkali-silicate melts and alkali-alkaline earth-silicate melts.

All compositions reported in this chapter show that Sn^{4+} is the dominating species at the studied conditions. Only in the peraluminous melt the fractions of Sn^{2+} and Sn^{4+} are approximately equal in number at 1300°C.

7.3.3 Comparison of the results determined by SWV and oxygen activity measurements

The standard reaction enthalpies, which have been determined by both, SWV and oxygen activity measurements, are in agreement within the limits of error. The error in the standard reaction enthalpies for melts 20 Na_2O · 80 SiO_2 and 16 Na_2O · 10 CaO · 20 Al_2O_3 · 54 SiO_2 (as described in section 7.2.1) is 10%, and the values obtained from oxygen activity measurements are smaller than those determined by SWV. However, the standard reaction enthalpies determined for the melt 10 Na_2O · 10 CaO · 25 Al_2O_3 · 55 SiO_2 and soda-lime silicate melts (described in 7.2.1 and section 7.2.2) have smaller errors and the values are in a very good agreement with those determined by SWV (maximum deviation 0.5%). The smaller values observed for the standard enthalpy which has been determined by oxygen activity measurements are probably due to the slight increase in the oxygen activity at constant temperature. The observed increase reflects an uptake of oxygen from the atmosphere. The very good agreement observed for the other melt composition has been explained by an improvement of the experimental set-up. That is that the surface of the working electrode which is inserted in the glass melt has been increased. According to Müller-Simon [62], a sufficient surface of the working electrode minimises the uptake of oxygen.

In Table B.2, the redox ratios which have been calculated from SWV data for an equilibrium with air at 1600°C are compared with the redox ratios which have been determined by oxygen activity measurements for the compositions 20 Na_2O · 80 SiO_2, 16 Na_2O · 10 CaO · 20 Al_2O_3 · 54 SiO_2 and 10 Na_2O · 10 CaO · 25 Al_2O_3 · 55 SiO_2. The quoted glass compositions have been melted for 5h at 1600°C. Both redox ratios in the glass compositions 20 Na_2O · 80 SiO_2 and 16 Na_2O · 10 CaO · 20 Al_2O_3 ·

54 SiO_2 are in agreement within the limits of error. The slightly higher fraction of Sn^{4+} detected by oxygen activity measurements is probably due to an uptake of oxygen from the atmosphere (see above) which slightly falsifies the evaluation of the redox ratios. Hence, it is assumed that after melting for 5h at 1600°C, the equilibrium was reached. For the composition 10 Na_2O · 10 CaO · 25 Al_2O_3 · 55 SiO_2 a higher fraction of Sn^{2+} has been observed by oxygen activity measurement. Since Sn^{2+} has been added as Sn(II)oxalate it is obvious that for this composition the redox equilibrium has not been reached at these melting conditions. The different behaviour is explained by the fact that the composition 10 Na_2O · 10 CaO · 25 Al_2O_3 · 55 SiO_2 has a far higher viscosity than the compositions 20 Na_2O · 80 SiO_2 and 16 Na_2O · 10 CaO · 20 Al_2O_3 · 54 SiO_2 (see section 5).

Furthermore, in Table B.2 the redox ratios of the compositions melted with the addition of carbon are compared with the redox ratios which have been determined by SWV at the respective melting temperature in air. For the composition 10 Na_2O · 10 CaO · 80 SiO_2 and 16 Na_2O · 10 CaO · 74 SiO_2 the fraction of Sn^{2+} is increased by a factor of ∼3, whereas for the compositions 20 Na_2O · 10 CaO · 70 SiO_2 and 26 Na_2O · 10 CaO · 64 SiO_2 the fraction of Sn^{2+} is increased by a factor of ∼5. Hence, by adding 0.2 wt.% C it is possible to decrease the redox ratio significantly at the used melt conditions. Furthermore, it should be noted that the compositions melted by adding carbon have been doped with 2 mol% SnO_2 and a larger SnO_2 concentration needs longer time to equilibrate due to limited oxygen diffusion.

7.4 Diffusion

7.4.1 Alkali- and alkali alkaline-earth-silicate melts

Diffusion coefficients can be calculated from the peak current of curve 4 in Fig. 6.3, according to Eq. (3.13). Figure 6.4 shows the peak currents as a function of $\tau^{-1/2}$ for the

Temp. in °C

Figure 7.12: Diffusion coefficients of tin as a function of the temperature in soda-silicate-melts. Data for $[Na_2O]$ = 15, 33% by G. von der Gönna. [70].

temperatures 1100° and 1350°C. Due to higher diffusion coefficients, the peak currents at 1350°C are larger than those at 1100°C. Equation (3.13) demands a proportionality between I_P and $\tau^{-1/2}$. Such a linear correlation is observed up to 0.14 ms$^{-1/2}$ (τ = 50 ms) at 1100°C and up to 0.45 ms$^{-1/2}$ (τ = 5 ms) at 1350°C. This is evidence for an electrode reaction controlled by diffusion of the electroactive species and a prerequisite for the calculation of diffusion coefficients. A deviation from linearity is observed at smaller pulse times. In the following, diffusion coefficients are calculated from the linear part of the relation peak current/$\tau^{-1/2}$ using Eq. (3.13) for temperatures at which no sign of crystallisation or phase separation has been detected.

Figure 7.12 shows the temperature dependency of the diffusion coefficients of tin in soda-silicate melts. Here, also the data for 15 $Na_2O \cdot 85$ SiO_2 and 33 $Na_2O \cdot 67$ SiO_2 are included [70]. A linear dependency is observed within the limits of error for all samples in the Arrhenius plot (log D versus the reciprocal temperature). Compo-

Temp. in °C
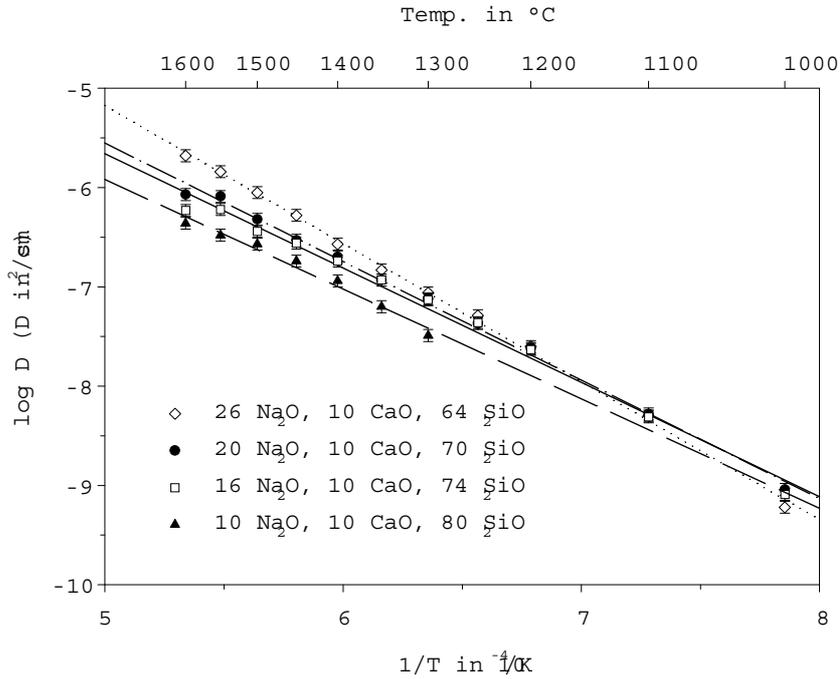
Figure 7.13: Diffusion coefficients of tin as a function of the temperature in soda-lime-silicate-melts.

sitions with larger Na_2O concentrations have higher diffusion coefficients at 1300°C. For Na_2O concentrations of 15 and 33 mol%, diffusion coefficients of $1.41 \cdot 10^{-8}$ and $9.25 \cdot 10^{-8}$ $cm^2 s^{-1}$ have been calculated. The diffusion coefficients for a temperature of 1300°C are given in Table B.3.

Figure 7.13 shows the temperature dependency of the diffusion coefficients of tin in soda-lime-silicate melts. A linear dependency has been observed within the limits of error in the Arrhenius plots for all compositions. Diffusion coefficients of $3.20 \cdot 10^{-8}$ and $8.77 \cdot 10^{-8}$ $cm^2 s^{-1}$ have been calculated for Na_2O concentrations of 10 and 26 mol%, respectively.

Figure 7.14 shows the temperature dependency of the diffusion coefficients of tin in alkali-lime-silicate melts with different alkali oxides. For all samples a linear dependency in the Arrhenius plot is observed within the limits of error. At 1300°C the largest diffusion coefficients ($7.41 \cdot 10^{-8}$ $cm^2 s^{-1}$) are observed for Na_2O containing melts. For the Li_2O containing melt a small decrease in the diffusion coefficient to a value of

Temp. in °C
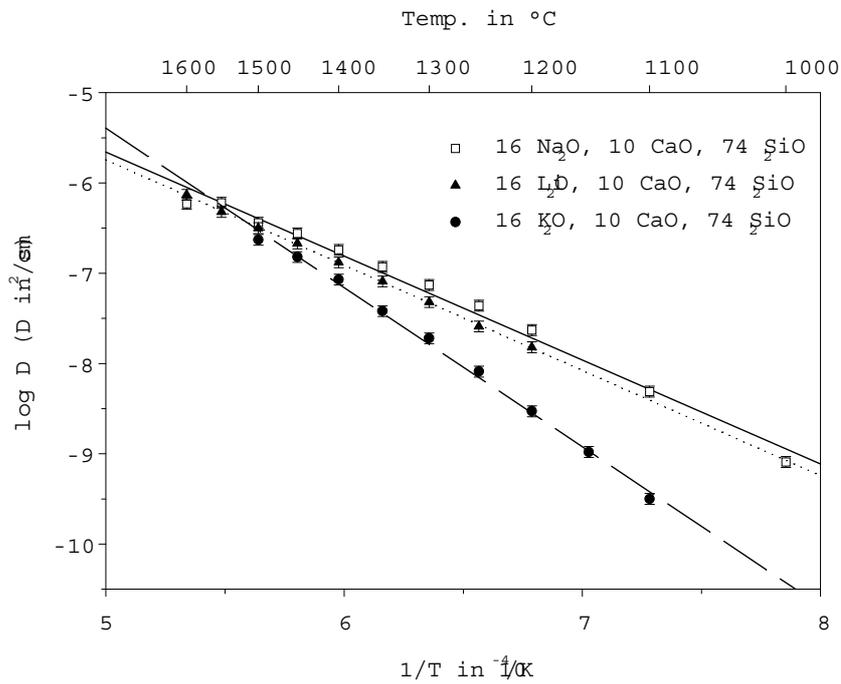
Figure 7.14: Diffusion coefficients of tin as a function of the temperature in alkali-lime-silicate melts.

Temp. in °C

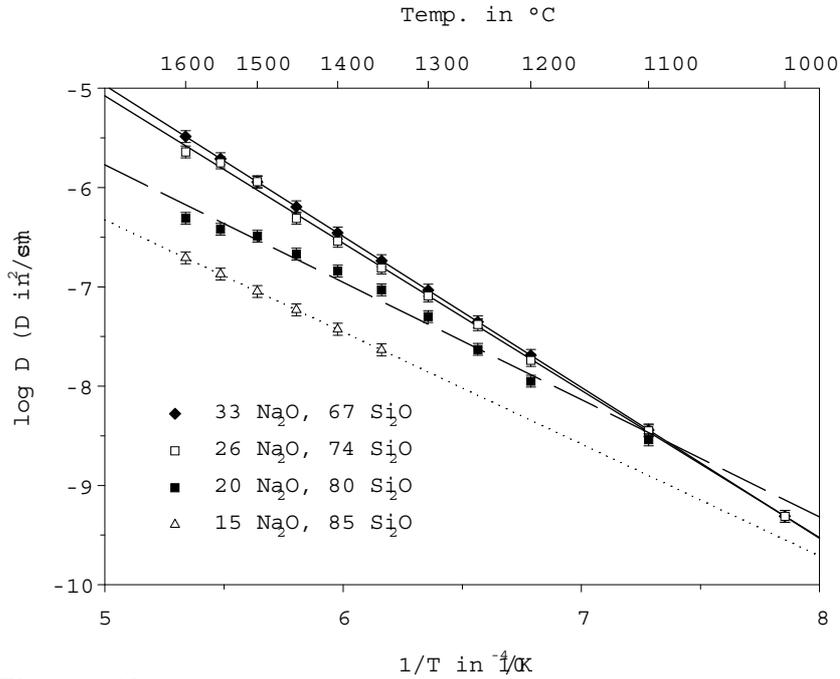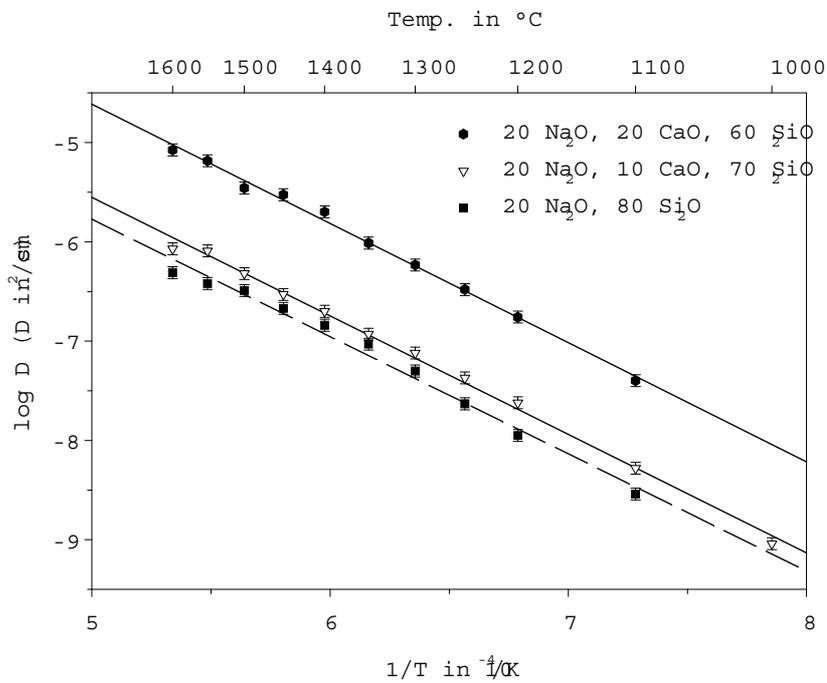Figure 7.15: Diffusion coefficients of tin as a function of the temperature in silicate melts.

Temp. in °C
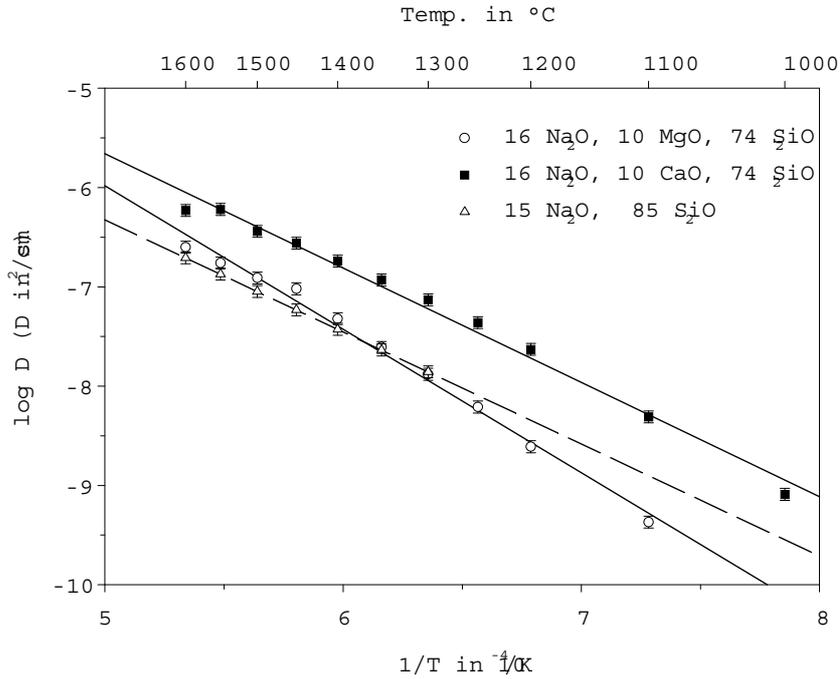
Figure 7.16: Diffusion coefficients of tin as a function of the temperature in silicate melts. Data for $[Na_2O] = 15$ mol% by G. von der Gönna [70].

$4.76 \cdot 10^{-8}$ cm^{2}s^{-1} is observed. The diffusion coefficient decreases further to a value of $1.91 \cdot 10^{-8}$ cm^{2}s^{-1} for K$_2$O containing melts.

In Fig. 7.15 the temperature dependency of the diffusion coefficients of tin in silicate melts is plotted for different CaO concentrations. Also here, for all compositions a linear dependency in the Arrhenius plots is observed within the limits of error. Compositions with higher CaO concentrations have larger diffusion coefficients in the investigated temperature range. For a temperature of 1300°C, diffusion coefficients of $4.96 \cdot 10^{-8}$ cm^{2}s^{-1} for the CaO free melt and of $5.92 \cdot 10^{-7}$ cm^{2}s^{-1} for the melt with 20 mol% CaO are calculated.

Figure 7.16 shows the diffusion coefficients of tin as a function of the temperature and different alkaline earth oxides. The data for $[Na_2O] = 15$ mol% are taken from Ref. [70]. A linear dependency within the limits of error is observed in the Arrhenius plots for all compositions. At a temperature of 1300°C a far larger diffusion coefficient of $7.41 \cdot 10^{-8}$ cm^{2}s^{-1} is observed for the CaO containing melts, whereas the MgO

containing melt and the melt without alkaline earth show almost the same diffusion coefficient of $1.31 \cdot 10^{-8}$ cm^{2}s^{-1} and $1.41 \cdot 10^{-8}$ cm^{2}s^{-1}.

From the linear parts in Figs. 7.12–7.16 the diffusion activation energies have been calculated and are summarised in Table B.3. The activation energies for soda-silicate melts range from 216 to 291 kJmol^{-1} and for soda-lime-silicate melts from 211 to 259 kJmol^{-1}. The diffusion activation energy increases from 223 kJmol^{-1} for 16 Li$_2$O $\cdot$ 10 CaO $\cdot$ 74 SiO$_2$ and 220 kJmol^{-1} for 16 Na$_2$O $\cdot$ 10 CaO $\cdot$ 74 SiO$_2$, respectively to 318 kJmol^{-1} for 16 K$_2$O $\cdot$ 10 CaO $\cdot$ 74 SiO$_2$. The diffusion activation energy shows no significant changes as a function of the CaO concentration. It varies between 222 and 229 kJmol^{-1}. The addition of MgO to a melt without alkaline earth leads to an increase in the diffusion activation energy. The type of alkaline earth has a strong effect on the activation energy. For the melt 16 Na$_2$O $\cdot$ 10 CaO $\cdot$ 74 SiO$_2$ and for the melt 16 Na$_2$O $\cdot$ 10 MgO $\cdot$ 74 SiO$_2$ diffusion activation energies of 220 and 277 kJmol^{-1} have been calculated, respectively.

7.4.2 Alumosilicate melts

Figure 7.17 shows the temperature dependency of the self-diffusion coefficients of tin in alumosilicate melts with 16 mol% Na$_2$O. A linear dependency is observed within the limits of error for all melt compositions. A complicated behaviour is observed for the tin diffusion coefficient as a function of the Al$_2$O$_3$ concentration. At 1300°C, the tin diffusion coefficients decrease with increasing Al$_2$O$_3$ concentration from $7.41 \cdot 10^{-8}$ cm^{2}s^{-1} in the melt without Al$_2$O$_3$ to $1.95 \cdot 10^{-8}$ cm^{2}s^{-1} for 10 mol% Al$_2$O$_3$. A further increase in the Al$_2$O$_3$ concentration to 15 mol% leads to an increase in the diffusion coefficient to $6.62 \cdot 10^{-8}$ cm^{2}s^{-1}. On the other hand, the diffusion coefficient decreases once more to a value of $3.63 \cdot 10^{-8}$ cm^{2}s^{-1} for the composition with 20 mol% Al$_2$O$_3$.

Figure 7.18 represents the temperature dependency of the self-diffusion coefficients of tin in alumosilicate melts with 10 mol% Na$_2$O. A sufficient number of peak currents fulfilling the linear correlation between I_P and $\tau^{-1/2}$ (see Eq. 3.13) could not be

Temp. in °C

1600 1500 1400 1300 1200 1100 1000

◇ 16 Na$_2$O, 10 CaO, 15 Al$_2$O$_3$, 59 SiO$_2$
□ 16 Na$_2$O, 10 CaO, 74 SiO$_2$
● 16 Na$_2$O, 10 CaO, 5 Al$_2$O$_3$, 69 SiO$_2$
▼ 16 Na$_2$O, 10 CaO, 20 Al$_2$O$_3$, 54 SiO$_2$
△ 16 Na$_2$O, 10 CaO, 10 Al$_2$O$_3$, 64 SiO$_2$

log D (D in cm^2/s)

1/T in 10^{-4} 1/K
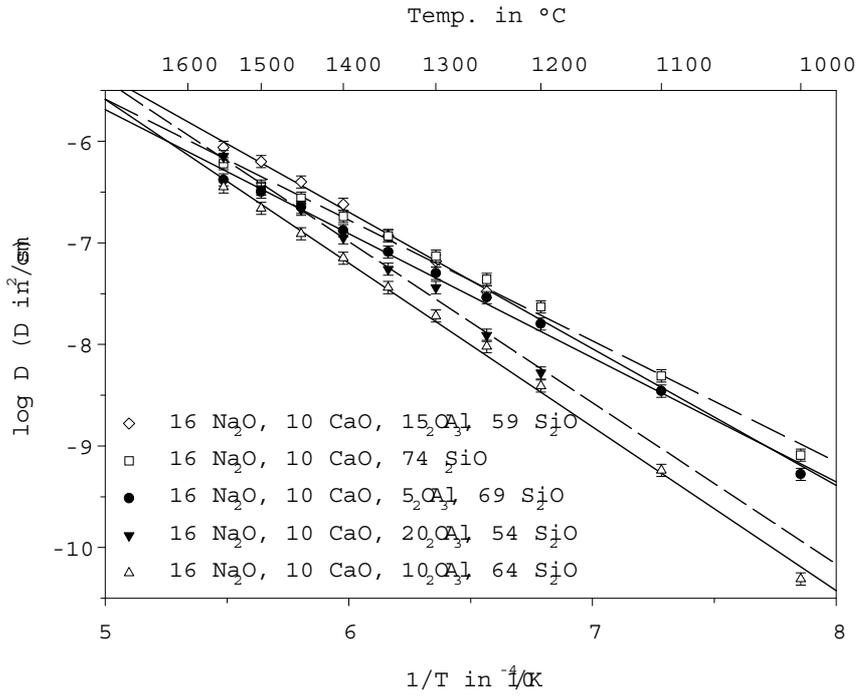
Figure 7.17: Diffusion coefficients of tin as a function of temperature in alumosilicate melts with 16 mol% Na$_2$O.

Temp. in °C

1600 1500 1400 1300 1200 1100 1000

▲ 10 Na$_2$O, 10 CaO, 15 Al$_2$O$_3$, 65 SiO$_2$
□ 10 Na$_2$O, 10 CaO, 80 SiO$_2$
○ 10 Na$_2$O, 10 CaO, 5 Al$_2$O$_3$, 75 SiO$_2$
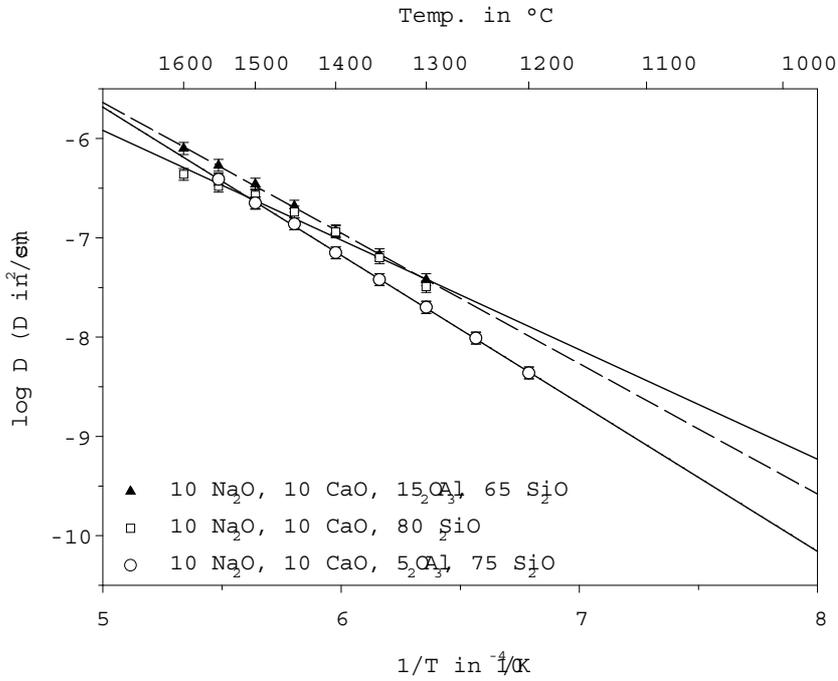
log D (D in cm^2/s)

1/T in 10^{-4} 1/K

Figure 7.18: Diffusion coefficients of tin as a function of temperature in alumosilicate melts with 10 mol% Na$_2$O.

provided for the composition with 25 mol% Al_2O_3. Hence, the calculation of diffusion coefficients has not been possible. A linear dependency has been observed within the limits of error for compositions containing up to 20 mol% Al_2O_3. The tin diffusion coefficients slightly decrease from $3.20 \cdot 10^{-8}$ to $1.99 \cdot 10^{-8}$ cm^2s^{-1} due to the addition of 5 mol% Al_2O_3 at a temperature of 1300℃. However, a further increase of the Al_2O_3 concentration leads to an increase of the diffusion coefficient to $3.79 \cdot 10^{-8}$ cm^2s^{-1}.

The activation energies have been calculated from the linear parts in Figs. 7.17 and 7.18 and are summarised in Table B.3. The diffusion activation energies vary between 220 and 304 $kJmol^{-1}$ for melts with 16 mol% Na_2O and range from 211 to 285 $kJmol^{-1}$ for melts containing 10 mol% Na_2O.

7.5 Discussion of tin diffusion coefficients

In both, soda-silicate and soda-lime-silicate system, the activation energies increase with increasing Na_2O concentration. The effect of the Na_2O concentration on the activation energies in soda-lime-silicate melts is less pronounced than in soda-silicate melts. The diffusion coefficients increase with increasing alkali concentrations at temperatures $\geq$ 1300℃. As shown in Fig. 5.1, this runs parallel with a decrease in the viscosities. Therefore, an increasing Na_2O concentration leads to both, larger tin diffusion coefficients and smaller viscosities. In order to discuss the diffusion activation energies and diffusion coefficients as an effect of the composition, it has to be taken into account that the viscosity of the melt has a large effect on the diffusion of any species. Hence, it is not possible to draw structural conclusions from the compositional dependency of the diffusion activation energy and the diffusion coefficients at constant temperature.

Figure 7.19 shows the tin diffusion coefficients of soda-silicate melts as a function of the viscosity. A linear correlation for all melt compositions is observed. Melts with the smallest alkali concentration have the largest diffusion coefficients at the same viscosity, which decrease with increasing alkali concentration.
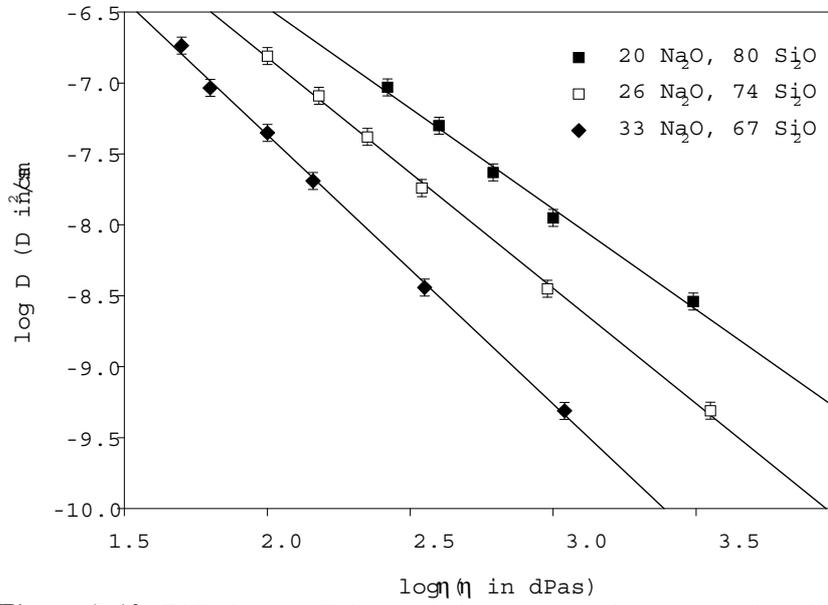
Figure 7.19: Diffusion coefficients of tin as a function of the viscosity in soda-silicate melts. Data for $33\ Na_2O \cdot 67\ SiO_2$ were taken of Refs. [67, 70].
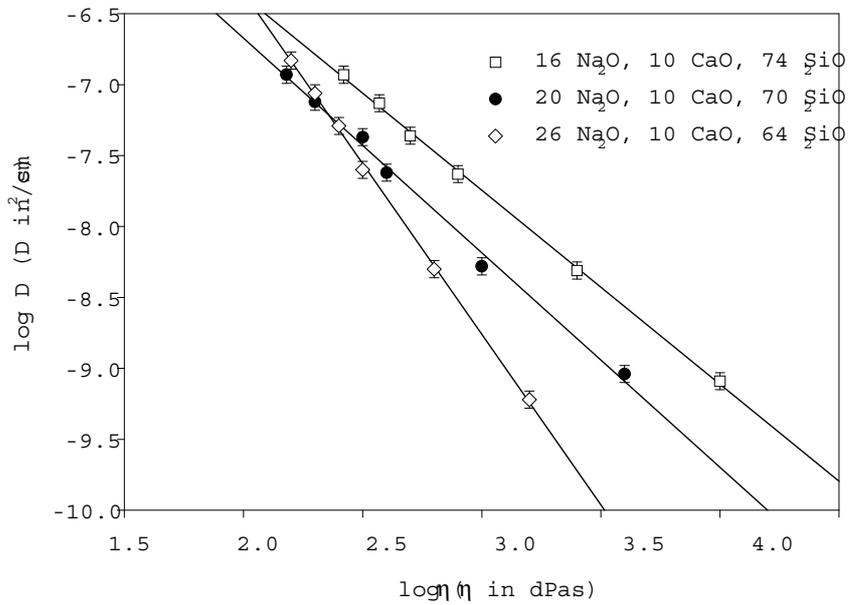
Figure 7.20: Diffusion coefficients of tin as a function of the viscosity in soda-lime-silicate-melts.
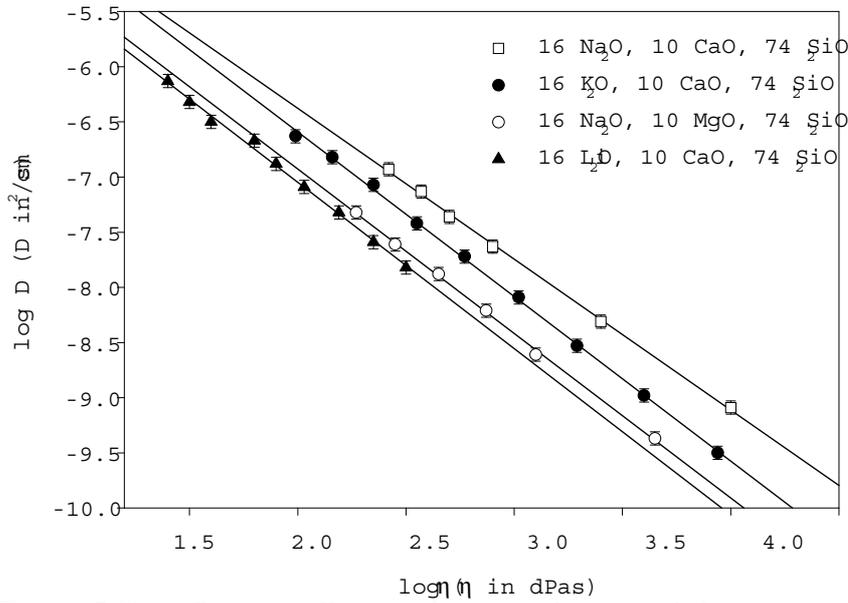
Figure 7.21: Diffusion coefficients of tin as a function of the viscosity in melts with different alkali and alkaline earth oxides. Viscosity data for $16\,K_2O \cdot 10\,CaO \cdot 74\,SiO_2$ and $16\,Na_2O \cdot 10\,MgO \cdot 74\,SiO_2$ are taken from Ref. [68].

Figure 7.20 shows the tin diffusion coefficients of soda-lime-silicate melts as a function of the viscosity. Also here, a linear correlation for all melt compositions is observed. At viscosities $log\ \eta\ (\eta/dPas) \geq 2.5$, melts with the smallest alkali concentration have the largest diffusion coefficients, which decrease with increasing alkali concentration. It has to be noted that the tin diffusion in the composition $26\,Na_2O \cdot 10\,CaO \cdot 64\,SiO_2$ is faster than in melts with smaller Na_2O concentrations at viscosities $log\ \eta\ (\eta/dPas)$ < 2.5.

Figure 7.21 shows the diffusion coefficients of tin as a function of the viscosity in melts with different alkali and alkaline earth oxides. A linear correlation for all melt compositions is observed. The melt $16\,Li_2O \cdot 10\,CaO \cdot 74\,SiO_2$ has the smallest diffusion coefficient, which increases for the melt $16\,Na_2O \cdot 10\,CaO \cdot 74\,SiO_2$. On the other hand, a further increase in the size of the alkali ion (Na to K) leads to a decrease in the diffusion coefficients. It can further be observed that the MgO containing melt
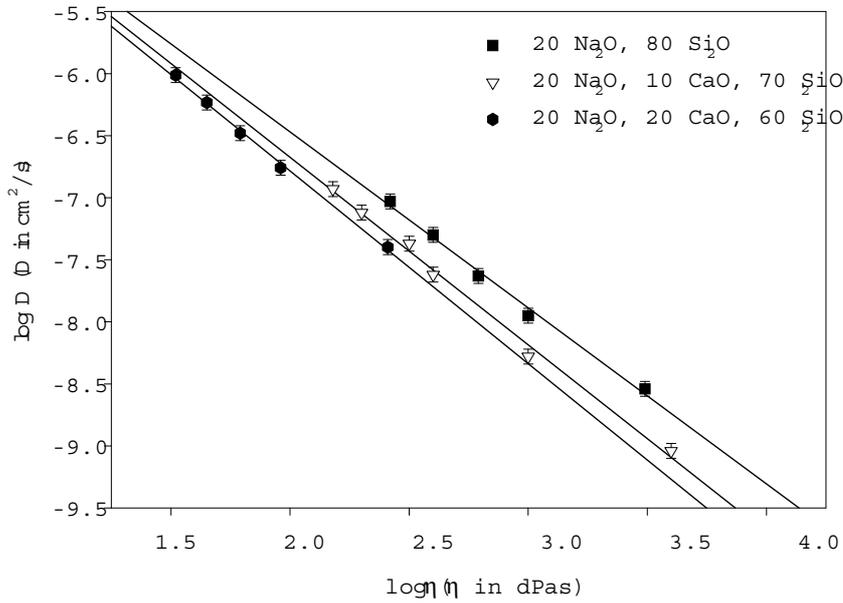
Figure 7.22: Diffusion coefficients of tin as a function of the viscosity in melts with varying CaO-concentrations.

shows a smaller tin ion diffusion than CaO containing melts.

Figure 7.22 shows the tin diffusion coefficients in melts with varying CaO concentrations as a function of the viscosity. Also here, a linear correlation for all melt compositions is observed. Melts without alkaline earth possess the largest diffusion coefficients, which slightly decrease with increasing CaO concentration.

Figure 7.23 shows the tin diffusion coefficients as a function of the viscosity in alumosilicate melts with 16 mol% Na_2O. A linear correlation for all melt compositions is observed. Alumina free melts have the smallest diffusion coefficient, which increases while increasing the Al_2O_3 concentration up to an Al_2O_3 concentration of 15 mol %. At larger Al_2O_3 concentrations a decrease of the tin diffusion coefficients is observed. The same trend is observed for alumosilicate melt with 10 mol% Na_2O (see Fig. 7.24).

The variation in the tin diffusion with increasing Al_2O_3 concentration has the same order of magnitude as the variation which has been observed in soda-lime-silicate melts by changing the melt composition. However, an increase in the Na_2O concentration
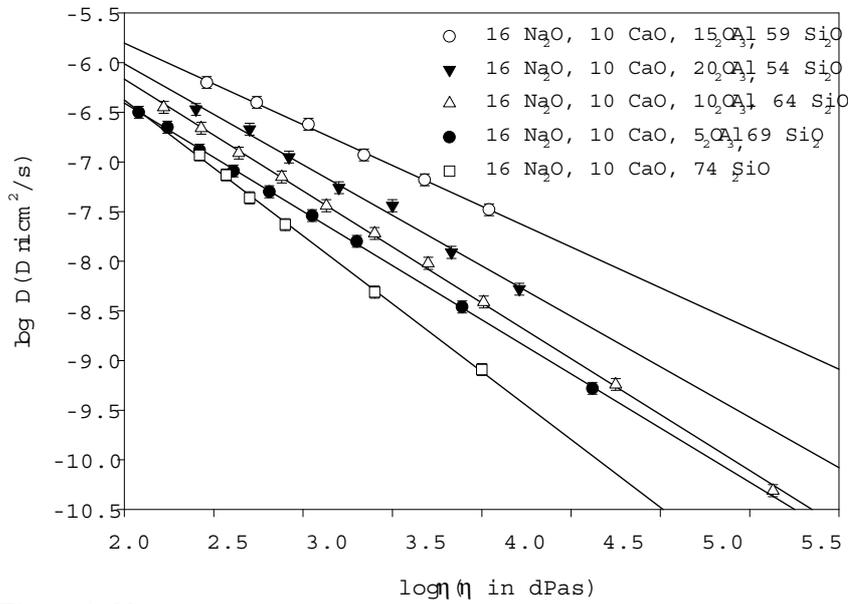
Figure 7.23: Diffusion coefficients of tin as a function of the viscosity in alumosilicate melts with 16 mol% Na_2O. Viscosity data for $16\ Na_2O \cdot 10\ CaO \cdot 5\ Al_2O_3 \cdot 69\ SiO_2$–$16\ Na_2O \cdot 10\ CaO \cdot 15\ Al_2O_3 \cdot 59\ SiO_2$ are taken from Ref. [68].
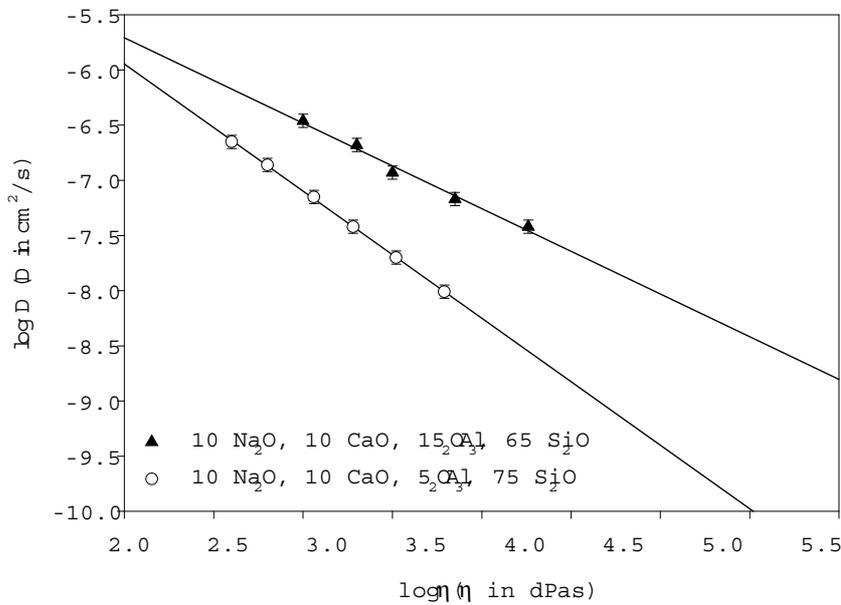
Figure 7.24: Diffusion coefficients of tin as a function of the viscosity in alumosilicate melts with 10 mol% Na_2O.

leads to a decrease of the tin diffusion coefficients. The largest effect due to variation of the melt composition has been observed in binary silicate melts as a function of the Na_2O concentration. The effect of the CaO concentration on the tin diffusion coefficients is rather insignificant. The effect due to a change of the alkali oxide or the alkaline earth oxide is small compared to that of the Na_2O and the Al_2O_3 concentration.

Chapter 8

Mössbauer spectroscopy

8.1 Measurements at room temperature

8.1.1 Silicates

Figure 8.1 shows the room temperature Mössbauer spectrum of the glass 16 Na$_2$O · 10 CaO · 74 SiO$_2$ doped with 2.5 mol% SnO$_2$. On the basis of a fit using Voigt functions, the spectrum has been deconvoluted into an asymmetrical doublet at 2.78 mms^{-1}, due to Sn^{2+} with a large quadrupole splitting and into a symmetrical doublet at -0.26 mms^{-1} due to Sn^{4+} with a small quadrupole splitting. The excellent fit of the spectrum and notably that of the asymmetric subspectrum due to Sn^{2+} has been achieved by using a linear coupling between the isomer shift and the quadrupole splitting [81] for divalent tin. Such coupling has not been applied in the case of the spectral part due to Sn^{4+}. As a consequence, the fits yield average isomer shifts and average quadrupolar interaction parameters for Sn^{2+} and isomer shifts and quadrupole splittings for Sn^{4+}. Table C.1 summarises the Mössbauer parameters of all compositions. For the glass 16 Na$_2$O · 10 CaO · 74 SiO$_2$ the isomer shifts have been found to be independent of the tin concentration (0.25, 1.6 and 2.5 mol%). Therefore, it is concluded that the tin concentration has no influence on the Mössbauer parameters in the investigated
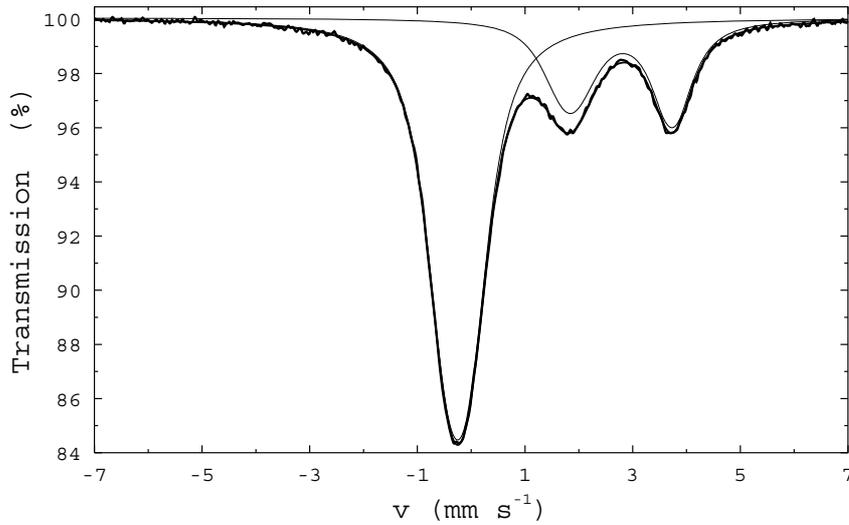
Figure 8.1: Mössbauer spectrum of the glass 16 Na$_2$O · 10 CaO · 74 SiO$_2$ doped with 2.5 mol% SnO$_2$ at room temperature.

concentration range.

Figures 8.2(a) and 8.3(a) present the isomer shifts of Sn^{2+} and Sn^{4+} as a function of the Na$_2$O concentration for soda- and soda-lime silicates. Values for the compositions 15 Na$_2$O · 85 SiO$_2$ and 33 Na$_2$O · 67 SiO$_2$ are taken from Ref. [28]. For Sn^{2+} the isomer shifts are found to vary between 2.75 and 2.72 mms^{-1} (soda-silicates) and to decrease from 2.81 to 2.68 mms^{-1} (soda-lime-silicates). In soda- and soda-lime-silicates the shifts of Sn^{4+} vary from -0.33 to -0.25 mms^{-1} and -0.26 to -0.23 mms^{-1}, respectively. For Sn^{2+} mean quadrupole splittings ranging from 1.90 to 1.93 mms^{-1} (soda-silicates) and from 1.85 to 1.95 mms^{-1}(soda-lime-silicates) are observed. In soda- and soda-lime-silicates the splittings of Sn^{4+} are found to take values from 0.34 to 0.42 mms^{-1} and 0.42 to 0.51 mms^{-1}, respectively. The quadrupole splitting of 0 mms^{-1} observed by [28] is treated as an outlier.

8.1.2 Alumosilicates

Figure 8.4 shows the room temperature Mössbauer spectrum of the glass 16 Na$_2$O · 10 CaO · 15 Al$_2$O$_3$ · 59 SiO$_2$ doped with 0.5 mol% SnO$_2$. The spectrum has been

(a)   (b)
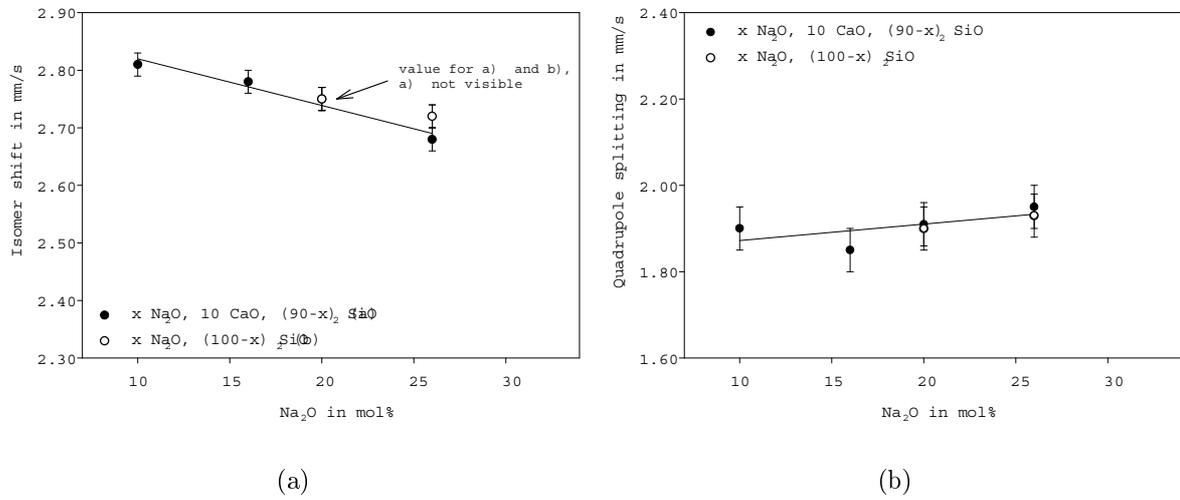
Figure 8.2: Isomer shift (a) and quadrupole splitting (b) of Sn^{2+} in soda- and soda-lime-silicates doped with 1.5–3.1 mol% SnO_2 as a function of the Na_2O concentration at room temperature.

(a)   (b)

Figure 8.3: Isomer shift (a) and quadrupole splitting (b) of Sn^{4+} in soda- and soda-lime-silicates doped with 0.5–3.1 mol% SnO_2 as a function of the Na_2O concentration at room temperature. Values for the compositions 15 $Na_2O \cdot$ 85 SiO_2 and 33 $Na_2O \cdot$ 67 SiO_2 are taken from Ref. [28] quoted relative to $CaSnO_3$.
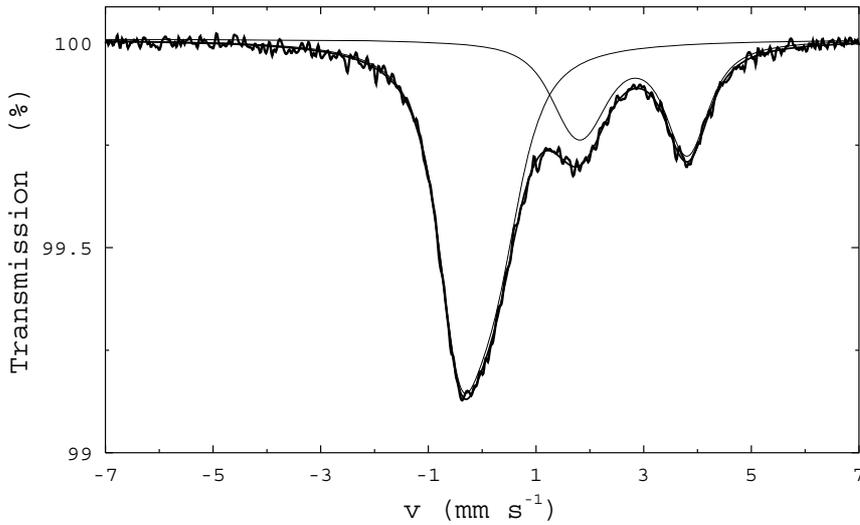
Figure 8.4: Mössbauer spectrum of the glass 16 Na_2O · 10 CaO · 15 Al_2O_3 · 59 SiO_2 doped with 0.5 mol% SnO_2 at room temperature.

deconvoluted into an asymmetrical doublet at 2.80 mms^{-1} due to Sn^{2+} with a large quadrupole splitting and into an asymmetrical doublet at -0.13 mms^{-1} due to Sn^{4+} with a smaller quadrupole splitting. The fitting procedure of the asymmetric subspectra has already been described in section 8.1.1. However, all Mössbauer spectra of the investigated alumosilicates show —in contrast to those of the investigated silicates— asymmetric subspectra due to both Sn^{2+} and Sn^{4+}. Table C.2 summarises the determined Mössbauer parameters. (It has not been possible to determine the Sn^{2+} parameters for the composition 16 Na_2O · 10 CaO · 20 Al_2O_3 · 54 SiO_2 due to small Sn^{2+} concentration (1.6 mol%) and low activity of the γ-ray source).

Figures 8.5(a) and 8.5(b) show the isomer shifts and quadrupole splitting of Sn^{2+} as a function of the Al_2O_3 concentration for alumosilicates. For Sn^{2+} the isomer shifts are observed to be constant within the limits of error. Unlike the isomer shifts the quadrupole splitting increases from 1.85 to 2.01 mms^{-1}. Figures 8.6(a) and 8.6(b) present the isomer shifts and quadrupole splitting of Sn^{4+} as a function of the Al_2O_3 concentration for alumosilicates. The isomer shifts and the quadrupole splitting are found to increase simultaneously from -0.26 to -0.04 mms^{-1} (IS) and from 0.42 to
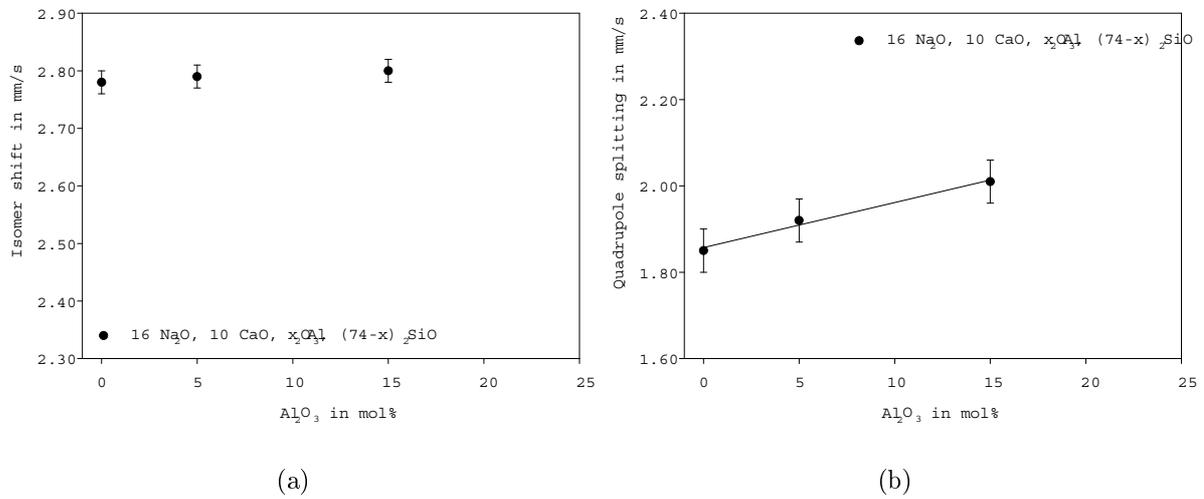
Figure 8.5: Isomer shift (a) and quadrupole splitting (b) of Sn^{2+} in alumosilicates doped with 0.5–2.5 mol% SnO_2 as a function of the Al_2O_3 concentration at room temperature.

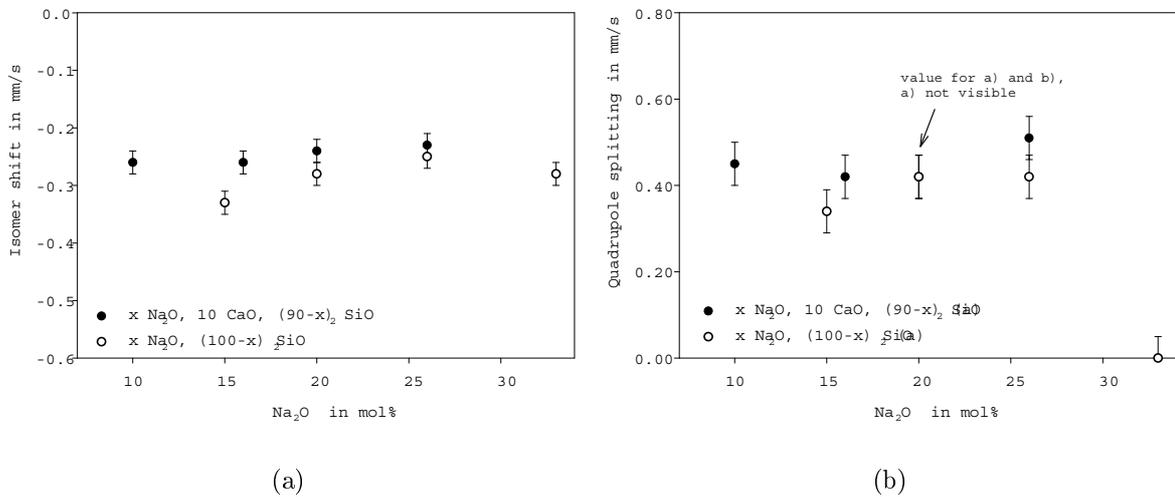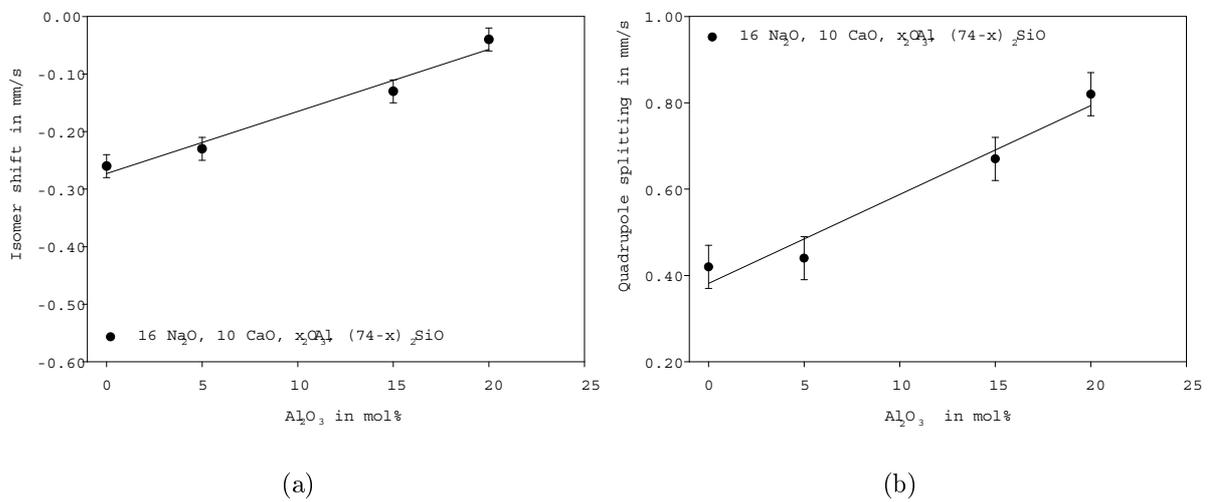
Figure 8.6: Isomer shift (a) and quadrupole splitting (b) of Sn^{4+} in alumosilicates doped with 0.5–2.5 mol% SnO_2 as a function of the Al_2O_3 concentration at room temperature.
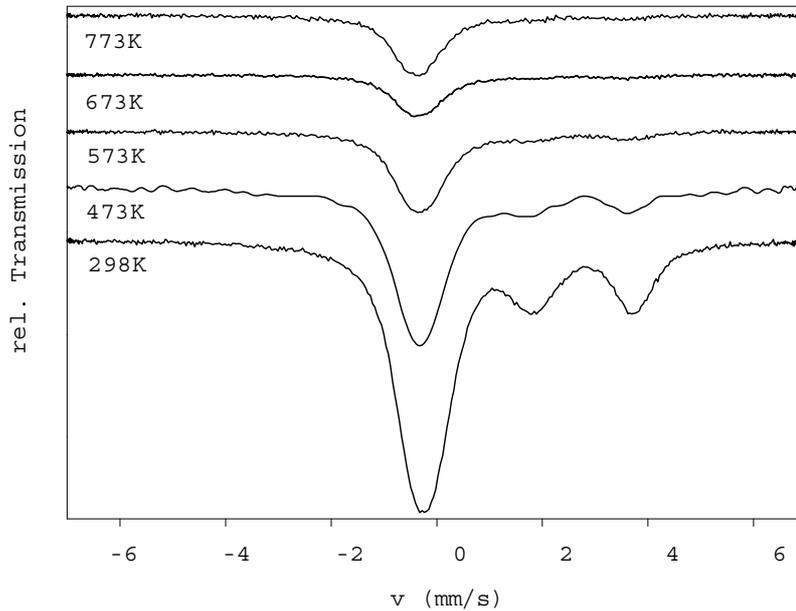
Figure 8.7: Mössbauer spectrum of the glass 16 Na$_2$O · 10 CaO · 74 SiO$_2$ doped with 2.5 mol% SnO$_2$ at different temperatures.

0.82 mms^{-1} (QS).

8.2   Measurements at high temperatures

Mössbauer spectra of the composition 16 Na$_2$O · 10 CaO · 74 SiO$_2$ doped with 2.5 mol% SnO$_2$ are shown for different temperatures in Fig. 8.7. The decrease in the signal intensities is clearly visible. Room temperature spectra which have been recorded before and after the high temperature measurements have proved that the redox ratio has not changed after the high temperature measurements. This enables the determination of the Debye temperatures according to Eq. (3.29). The Debye temperatures have been calculated from the slope of ln A (absorption area) vs. temperature by using the values of ln A which are listed in table C.1 and C.2. For instance, Sn^{2+} has a Debye temperature of 186K and Sn^{4+} a Debye temperature of 263K in the glass 16 Na$_2$O · 10 CaO · 74 SiO$_2$. It has been found that the Debye temperatures of both, Sn^{2+} and Sn^{4+} do

Table 8.1: Debye temperatures Θ_D

Composition (mol%)	[SnO$_2$] (mol%)	Θ_D(Sn^{2+}) (K)	Θ_D(Sn^{4+}) (K)
20 Na$_2$O $\cdot$ 80 SiO$_2$	1.5	179	263
26 Na$_2$O $\cdot$ 74 SiO$_2$	3.1	178	266
10 Na$_2$O $\cdot$ 10 CaO $\cdot$ 80 SiO$_2$	2.4	187	270
16 Na$_2$O $\cdot$ 10 CaO $\cdot$ 74 SiO$_2$	2.5	186	263
20 Na$_2$O $\cdot$ 10 CaO $\cdot$ 70 SiO$_2$	3.0	187	272
26 Na$_2$O $\cdot$ 10 CaO $\cdot$ 64 SiO$_2$	2.4	187	272
16 Na$_2$O $\cdot$ 10 CaO $\cdot$ 20 Al$_2$O$_3$ $\cdot$ 54 SiO$_2$	1.6	n.d.	257

not change within the limit of error ± 10K for the investigated glass compositions (see Table 8.1).

In order to determine the correct Sn^{4+}/Sn^{2+} redox ratios, it is necessary to account for the respective Debye-Waller factors f_D of the tin species. The Debye-Waller factors f_D can be determined from the temperature dependent signal intensities in the framework of the Debye model of lattice vibrations (see Eq. 3.29). f_D(Sn^{2+}, 293K = 0.22$\pm$0.04) and f_D(Sn^{4+}, 293K = 0.49$\pm$0.04) have been obtained for Sn^{2+} and Sn^{4+}, respectively. These values are characteristic for all investigated soda-silicate and soda-lime-silicate glasses. It it assumed that an increasing Al$_2$O$_3$ concentration does not exercise an influence on the Debye-Waller factors f_D of the respective tin species. The corrected redox ratios are listed in Tables C.1–C.3.

8.3 Discussion of results from Mössbauer spectroscopy

8.3.1 Incorporation of Sn^{2+} in glass

Table 8.2 gives an overview of isomer shifts (IS) of Sn^{2+}, quadrupole splittings (QS) and Debye temperatures θ_D reported in the literature for glasses and relevant crystalline compounds. In this study average isomer shifts have been found to take values between 2.68 and 2.81 mms^{-1} with quadrupole splittings from 1.85 to 2.01 mms^{-1} (see Figs. 8.2(a) and 8.2(b), 8.5(a) and 8.5(b)). These values are within the range of IS and QS observed for Sn^{2+} in glasses reported in the literature.

In order to interpret the experimental Mössbauer parameters —IS and QS— they have to be compared to the parameters of well known crystalline compounds. For this reason a short description of crystalline and amorphous SnO is given in the following: The crystal structure of gray SnO is tetragonal. Sn^{2+} is placed at the top of a square pyramid [83]. Here, the main contribution of the electric field gradient arises from the unbalanced p-electron population of the non-bonding lone pair. Compared to crystalline SnO, IS and QS are increased in amorphous SnO [82]. The increase of the electric field gradient can be attributed to an increase in the difference between the p-electron in the z-direction and the population in the x-y plane $(\sigma_p - \pi_p)$ compatible with an axial elongation of the pyramid. Thus the general interpretation is that the axial bond length is larger in amorphous SnO. A decrease in the Debye temperature confirms the assumption that the covalent character has not increased [82]. This interpretation is in agreement with the observation that the IS is found to decrease when pressure is applied, i.e. when the density increases, which shows the shielding effect of the p-electrons [84].

In contrast to tetravalent tin, see below, a clear correlation between the shift and the electronegativity has not been established for divalent tin compounds [59]. However, for Sn^{2+} ions the completely ionic configuration is $4d^{10}5s^2$. The transition from the ionic $5s^2$ configuration towards a more covalent 5s-p hybridisation is accompanied by a

Table 8.2: Mössbauer parameters of Sn^{2+} from literature

amorphous material	IS (mms^{-1})	QS	to	IS (mms^{-1})	QS	Θ_D (K)	Ref.
float glass	2.84	1.97	–	2.89	2.01	191–170	[3]
float glass (15 wt% SnO)	2.87	1.96				206	[29]
silicates*	2.8		–	3.1			[30]
tin-silicates	~ 3	2.0				181–191	[31]
alkali-tin silicates	2.24	2.07	–	3.19	1.94	172–210	[32]
soda-silicate (5–10 mol% SnO_2)	2.66	1.87	–	2.79	1.90	181	[33]
alkali-alkaline earth-tin silicates	2.61	1.92	–	2.98	2.06		[34]
borates	2.91	2.09	–	3.56	1.78		[35]
borates						185–192	[36]
tin borate glasses	2.76	1.80	–	3.43	1.78		[37]
fluorophosphate	3.30	1.70	–	3.36	1.72	146	[38]
SnO	2.87	1.71				181	[82]
IS of crystalline compounds range from 2.3 to 4.4 mms^{-1}							[60]
SnO	2.68	1.36				203	[82]

IS are quoted relative to $CaSnO_3$. IS scale assumes that the $CaSnO_3$ shift is the same as the $BaSnO_3$ shift. *) The used γ-source is unknown.

decrease in the 5s-electron density and an increase in the electrical field gradient. There is a rough negative correlation between IS and QS [61]. Thus, for Sn^{2+}, a decreasing shift accompanied by an increase in the quadrupolar interaction corresponds to an increase in covalent character of the chemical bonds.

In this study the quadrupole splittings take values between 1.85 and 2.01 mms^{-1} (see Fig. 8.2(b) and 8.5(b)). This values are larger than those observed for crystalline and amorphous SnO —1.36 and 1.71 mms^{-1}, respectively (see Table 8.2). The quadrupole splitting increases either as the s-electron density decreases or as the arrangement of the ligands —the electron charge distribution in the neighbourhood of the tin atom— becomes more asymmetric [32]. The decrease in the s-electron density implies a decrease in IS (see the correlation between IS and QS explained above). Since the observed average isomer shifts (2.68 to 2.80 mms^{-1}, see 8.2(a) and 8.5(a)) are smaller than that of amorphous SnO (2.87 mms^{-1} (see Table 8.2)), it seems reasonable to suppose that Sn^{2+} in glasses is slightly more rigidly bound than in amorphous SnO. The slightly higher Debye temperature of 184K compared with that of amorphous SnO (181K) might support this assumption. (The Debye temperature is a measure of the bonding strength and is discussed in detail in section 8.4).

In soda-lime-silicate glasses the IS of Sn^{2+} are found to decrease slightly with increasing Na_2O concentration. Such a dependency on the Na_2O concentration was already observed in ternary silicate glasses [85]. This decrease is simultaneously accompanied by an increase in the QS of the Sn^{2+} ions (see Figs. 8.2(a) and 8.2(b)). For Sn^{2+}, a decreasing shift accompanied by an increase in the quadrupolar interaction corresponds to an increase in the covalent character of the chemical bonds. (The correlation between IS and QS has above been outlined in detail). However the Debye temperature of Sn^{2+} is constant within the limits of error (see Table 8.1).

Now there is the question which effect gives rise to this slight strengthening of the Sn^{2+}-O bonds. The strengthening of the Sn^{2+}-O bonds itself suggests a weakening of the respective O-cation bonds. The weakening of the O-cation bond is caused by a larger

and less polarising cation. Such a systematic variation of the Mössbauer parameters was early established for alkali-metal or related tin(II)halides [86]. In consequence, it seems reasonable to assume that the $[Sn(II)O_4]^{2-}$ complex is located in a slightly different neighbourhood as the Na_2O concentration increases.

In alumosilicates the quadrupole splittings of Sn^{2+} ions are found to increase with increasing Al_2O_3 concentration. In contrast to the correlations outlined above, this increase is not accompanied by a change of the IS of Sn^{2+}, i.e. the IS remains constant within the limit of error as the Al_2O_3 concentration increases (see Figs. 8.5(a) and 8.5(b)). In general, QS increases as the s-electron density decreases or as the arrangement of the ligands becomes more asymmetric [32]. A decrease in the s-electron density implies a decrease in IS. Hence, the observed increase in QS might be due to an increasing asymmetry of the ligands —e.g. oxygen which is bound to Si and oxygen which is bound to Al. This is not surprising since Al acts in the investigated concentration range as a NWF —in tetrahedral coordination— in analogy to Si.

However, the correlations between isomer shifts, quadrupole splittings and Debye temperatures are very complex and thus, not easy to interpret. This can be recognised by studying the values of IS, QS and θ_D of glasses reported in the literature (see Table 8.2).

8.3.2   Incorporation of Sn^{4+} in glass

Table 8.3 gives an overview of the isomer shifts (IS) of Sn^{4+}, quadrupole splittings (QS) and Debye temperatures θ_D which are reported in the literature for silicate and borate glasses and relevant crystalline compounds. In this study average isomer shifts have been found to take values between -0.33 and -0.04 mms^{-1} with quadrupole splittings from 0.34 to 0.82 mms^{-1} (see Figs. 8.3(a) and 8.3(b), 8.6(a) and 8.6(b)). The isomer shifts are within the limits of error in the range of IS reported for Sn^{4+} in glasses in the literature. Nevertheless, such a large quadrupole splitting as 0.83 mms^{-1} of Sn^{4+} in glasses was not yet reported in the literature.

Table 8.3: Mössbauer parameters of Sn^{4+} from literature

amorphous material	IS (mms^{-1})	QS	to	IS (mms^{-1})	QS	Θ_D (K)	Ref.
float glasses	-0.20	0.41	–	-0.11	0.58	283–230	[3]
float glasses	-0.27	0.43	–	-0.26	0.39		[39]
float glass (15 wt% SnO)	-0.20	0.48				364	[29]
silicates*	-0.25		–	-0.02			[30]
soda silicates (2–10 mol% SnO$_2$)	-0.27	0.5	–	-0.22	0.5	232–308	[33]
borates	-0.21		–	-0.04			[35]
borate						259	[36]
tungstate	-0.02					360	[25]
fluorophosphate	-0.23					155	[38]
SnO$_2$	0.13	0.70				243	[82]
Is of crystalline compounds range from -0.4 to 1.9 mms^{-1}							[60]
SnO$_2$	0.00	0.45				313	[82]
Malayaite CaSn[OSiO$_4$]	-0.07	1.45				410	[87]
Pabstite Ba(Sn,Ti)[Si$_3$O$_9$]	-0.28	0.4				339	[33]
K$_2$SnF$_6$	-0.39						[88]

IS are quoted relative to CaSnO$_3$. IS scale assumes that the CaSnO$_3$ shift is the same as the BaSnO$_3$ shift. *) The used γ-source is unknown.

In order to interpret the values of the Mössbauer parameters —IS and QS— they have to be compared to the parameters of well known crystalline compounds. For this reason a short description of crystalline and amorphous SnO_2 is given in the following: The crystal structure of SnO_2 is of the Rutile type: Sn^{4+} is situated in a distorted octahedron, all Sn-O distances are equal in the basal plane. The Sn-O axial distances in direction perpendicular to the basal plane are by 2% longer than those in the base [89]. Such a structure generates a non-axially-symmetric electric field gradient. Hence, the large change in the quadrupole splittings (see Table 8.3) between amorphous and crystalline SnO_2 can be attributed to a further elongation of the axial Sn-O bond with respect to the basal bonds. The IS (see Table 8.3) of amorphous SnO_2 is more positive than in crystalline SnO_2 suggesting a larger s-density at the nucleus. This is due to a decrease in donation of s-electrons to the oxygen ion caused by larger distances in amorphous SnO_2 rather than an increase in covalency of the Sn-O bond. Besides, the Debye temperature of amorphous SnO_2 ($\theta_D = 243K$) is smaller than in crystalline SnO_2 ($\theta_D = 313K$). Since a smaller Debye temperature corresponds to a weaker bonding, it was concluded that the covalency in the Sn-O bond of amorphous SnO_2 is not increased [82].

For tetravalent tin compounds, there is a clear correlation between the isomer shift and the ionicity of the bonds: Compounds of tetravalent tin range from 1.9 mms^{-1} for essentially covalent compounds to about -0.4 mms^{-1} for fully ionic compounds [60]. That signifies that increasing bond ionicity correlates with decreasing isomer shifts. In this context, the shift of K_2SnF_6 -0.39 mms^{-1} is one of the smallest known shifts of tetravalent tin [88]. The ionic character of Sn^{4+} bonds in crystalline SnO_2 gives rise to an isomer shift of 0.00 mms^{-1} [82]. Since the isomer shifts measured in this work are between theses values, the bonding of Sn^{4+} in silicates may be predominantly ionic. The quadrupole splitting of $\sim$0.44 mms^{-1} implies that Sn^{4+} is incorporated in analogy to crystalline SnO_2. That is in an octahedral coordination situated in a fairly symmetric neighbourhood. The high ionicity of the Sn^{4+}-O bonds implies a high

polarising cation such as Si in the vicinity of the oxygen ion. The high ionicity of the Sn^{4+}-O bonds is in agreement with the lower Debye temperature observed for Sn^{4+} ($\sim$268K) in silicate glass in comparison to that of crystalline SnO_2 (313K). (The Debye temperature is a measure of the bonding strength as discussed in detail in section 8.4).

In this study the isomer shifts of Sn^{4+} are found to be constant within the limits of error with increasing Na_2O concentration. Furthermore, the quadrupole splittings and Debye temperatures are not affected by Na_2O concentrations. In consequence, it has been concluded that the neighbourhood of Sn^{4+} does not significantly change in soda-silicate and soda-lime-silicate glasses. Nevertheless, increasing the Al_2O_3 concentration —from 0 to 20 mol%— leads to an increase of the isomer shift by 0.22 mms^{-1}. In the case of tetravalent tin with its ideal ionic configuration of $4d^{10}$, this observation corresponds to an increase in the number of 5s-electrons associated with the tin atoms. As outlined above, this probably represents an increase in the covalent character of the chemical bonds. However, such a clear increase in covalency should be accompanied by an increase in the Debye temperature —larger Debye temperatures correspond to stronger bonding. The results of this study do not confirm such an increase in the Debye temperature. Indeed, there is a slight decrease from 263K to 257K as the Al_2O_3 concentration increases from 0 to 20 mol%. However, the increase in the isomer shift is accompanied by an increase in the quadrupole splitting of 0.40 mms^{-1}. A similar difference in isomer shift and quadrupole splitting is observed between crystalline and amorphous SnO_2 but accompanied by an evident decrease in the Debye temperature. (The difference in the structure of crystalline and amorphous SnO_2 is described above). Nevertheless, the simultaneous increase in the s-electron density and quadrupole splitting with increasing Al_2O_3 concentrations may result from elongation of the axial Sn^{4+}-O bonds, rather than from a change in the degree of covalency.

8.4   Function of tin ions in glass network

The Debye temperature of $\sim$269K (soda-lime-silicate) for Sn^{4+} —present in octahedral coordination— does not change within the limit of error as the Na_2O concentration is varied. Also the addition of Al_2O_3 to a soda-lime-silicate glass does not greatly affect the Debye temperature of Sn^{4+}. Nevertheless, the Debye temperature of $\sim$187K Sn^{2+} —present in fourfold coordination— is far smaller indicating that Sn^{4+} is more rigidly bonded to the glass network than Sn^{2+}. The variation in the Na_2O concentration neither has a pronounced effect on the Debye temperature of Sn^{2+}. As a result, it seems reasonable to suppose that the incorporation of tin ions is not affected in a large extent by variations in the Na_2O concentration. For the Al_2O_3 concentration, however, there are not enough data available to propose any trend.

Now, the question arises which function have Sn^{2+} and Sn^{4+} in soda-lime-silicates and in the investigated alumosilicate glass: According to Nishida [25]-[27] the Debye temperature θ_D for a network former is higher than 280K —owing to its stronger bonding to the glass network, whereas the Debye temperature θ_D assigned to a network modifier is smaller than 270K. According to this hypothesis, Sn^{2+} acts as network modifier and Sn^{4+} is a border line case. Nevertheless, other authors [90, 91] have observed that Sn^{4+} being present in octahedral coordination strengthens the glass network in silicate glasses. On the other hand, larger Debye temperatures θ_D for Sn^{4+} were observed in soda-silicate glass having 10 mol% SnO_2 (308K) [33] and in float glass with 15 mol% SnO_2 (364K) [29]. Further, it was found that Sn^{4+} has a very low solubility in pure SiO_2 and is difficult to accommodate in a tetrahedral network due to its preference for octahedral coordination [31]. In consequence, Williams et al. [92] have suggested an intermediate function for Sn^{4+} having a Debye temperature θ_D of 260K and being present in octahedral coordination in float glass. Accordingly, the splitting into exclusively network modifier and network former might be too strict and an "intermediate" may be added to this graduation for the case of Sn^{4+}. However, the splitting into network modifiers and network formers as a measure of the Debye

temperature may be easier understandable in correlation with the polarising power of the network forming cations in which Sn^{4+} is incorporated: Large Debye temperatures θ_D are observed when Sn^{4+} is incorporated in a glass network formed by network formers having a smaller polarising power. For example, a Debye temperature θ_D of 360K was found for Sn^{4+} in a tungstate glass [25]. According to this, a less polarising network former gives rise to a weakening of the O-NWF bond and in consequence to a strengthening of the Sn^{4+}-O bond. Small Debye temperatures θ_D are observed when Sn^{4+} is incorporated in a glass network formed by network former having a large polarising power. For example a Debye temperature θ_D of 155K was determined in a fluorophosphate glass [38]. In this context it seems reasonable to assume that Sn^{4+} acts as an intermediate in silicate glasses.

For Sn^{2+} caution might be exercised in applying the "Nishida model": The Debye temperatures, which have been reported in the literature, are not larger than 210K (see Table 8.2) implying that Sn^{2+} is always present as a network modifier. Nevertheless, several authors [29, 31, 32, 93] indicated that SnO is not only acting as a network modifier, but rather as intermediate or even conditional former.

Chapter 9

Discussion

9.1 Redox ratios

By means of both methods, square-wave voltammetry and Mössbauer spectroscopy, only Sn^{2+} and Sn^{4+} have been detected. Thus, there is no occurrence of metallic tin, even under reducing conditions reached in the SWV experiments at high negative potentials. The redox ratios of glasses having the same SnO_2 concentration determined by means of both methods are listed in Table 9.1.

Comparing the Sn^{4+}/Sn^{2+} redox ratios evaluated by using square-wave voltammetry and Mössbauer spectroscopy, the ratios determined from both methods are in agreement within the limits of error. Even the determination of the redox ratios in alumosilicate glasses by using estimated values for the Debye-Waller factors leads to acceptable results.

Hence, the knowledge of the Debye-Waller factors enables the evaluation of the redox ratios by means of Mössbauer spectroscopy in soda-silicate, soda-lime-silicate and alumosilicate glasses.

Table 9.1: Redox ratios determined by square-wave voltammetry at 1600°C, oxygen activity measurements and Mössbauer spectroscopy (MS)

Composition (mol%)	[SnO$_2$] (mol%)	Sn^{2+} (%)	Sn^{4+} (%)	Sn^{2+} (%)	Sn^{4+} (%)
		by SWV		by MS	
16 Na$_2$O · 10 CaO · 74 SiO$_2$	0.25	29(1)	71(1)	34(6)	66(6)
16 Na$_2$O · 10 CaO · 5 Al$_2$O$_3$ · 69 SiO$_2$	0.5	44(1)	56(1)	54(6)	46(6)
16 Na$_2$O · 10 CaO · 15 Al$_2$O$_3$ · 59 SiO$_2$	0.5	56(1)	44(1)	51(6)	49(6)
		by a$_{O_2}$		by MS	
10 Na$_2$O · 10 CaO · 80 SiO$_2$	2.0	64(3)	36(3)	60(6)	40(6)
16 Na$_2$O · 10 CaO · 74 SiO$_2$	1.8	45(3)	55(3)	33(6)	67(6)
20 Na$_2$O · 10 CaO · 70 SiO$_2$	1.6	43(3)	57(3)	45(6)	55(6)
26 Na$_2$O · 10 CaO · 64 SiO$_2$	1.3	37(3)	63(3)	32(6)	68(6)

Figure 9.1: Redox ratios of tin (a) and iron (b) at 1300°C as a function of the alkali concentration in silicate melts. Data for the melts 15 $Na_2O \cdot 85\ SiO_2$, 33 $Na_2O \cdot 67\ SiO_2$ and iron redox ratios are taken from Ref. [70] and Refs. [7, 68] .

9.2   Comparison with other studies mainly of iron

9.2.1   Redox equilibria and structure

As seen in Fig. 9.1(a) in soda-silicate melts most of the tin is present in the Sn^{4+} state, but still a very small fraction of Sn^{2+} is present. However, if CaO is added to a soda silicate melt, there exists a linear correlation between the redox ratio and the Na_2O concentration: There is a slight increase from 95 to 97.3 % at 1300°C; at 1600° this trend is more pronounced —however still small: it increases from 63.4 to 72.5%. (The effect of the CaO concentration on the redox equilibrium is discussed below.) It has been noted also by other authors that the tetravalent state is most stable in silicate glasses [5, 28, 94]. The present finding, that at higher alkali concentrations the higher oxidation state is slightly favoured, has already been reported in other studies, e.g. concerning the polyvalent element tin [30, 95] and iron (see Fig. 9.1(b) [7, 8]. It was found that Fe^{3+} being present in tetrahedral coordination is as well the dominating

species. $[FeO_4]^-$ tetrahedra are charge compensated mainly by alkali ions —charge compensation by Ca^{2+} is less effective but possible. A smaller alkali ion exercises a more stabilising effect on the FeO_4 tetrahedra due to its larger Coulomb forces. As a consequence, larger alkali concentrations and smaller alkali ions lead to slightly larger Fe^{3+}/Fe^{2+} redox ratios [7, 8, 14].

As outlined above, both Sn^{4+} and Fe^{3+} are highly favoured in alkali-silicate glasses. For Fe^{3+}, however, it is described above that its occurrence is mainly linked to the presence of network modifiers. This implies that this might also be the case for Sn^{4+}. The validity of this statement will be discussed throughout this chapter:

First, it has been concluded from Mössbauer spectroscopy that Sn^{4+} is incorporated in octahedral coordination (see chapter 8). Further, several authors have suggested that Sn^{4+} enters the glass network in the presence of alkali as $[SnO_{6/2}]^{2-}$ octahedra [91, 96, 97] and that the coordination number of tin depends largely on the alkali species [98]. Takeda [99] has remarked that the formation of non bridging oxygen is required to provide the local electroneutrality around Sn^{4+} being present in octahedral coordination.

Second, a further indicator might be the existence of crystalline compounds R_2SnO_3 with R = Li, Na. [100].

Third, evidence for charge compensation of $[SnO_{6/2}]^{2-}$ octahedra by alkali ions might be the fact that several authors have observed that Sn^{4+} does not enter pure SiO_2 glass due to its tendency for octahedral coordination. Nevertheless, Sn^{2+} is found to be incorporated in binary tin-silicate glasses [29, 31, 93].

In summary, the incorporation of Sn^{4+} in silicate glasses has only been observed in alkali containing silicate glasses which seems to be an evidence for alkali stabilisation of Sn^{4+} octahedra.

In Fig. 9.1(a) it can be seen that the stabilisation of Sn^{4+} is getting slightly less effective in the sequence K → Na → Li. This effect was also described in Ref. [30, 98]. However, this is contrary to the observation made for the Fe^{3+}/Fe^{2+}-redox equilibrium
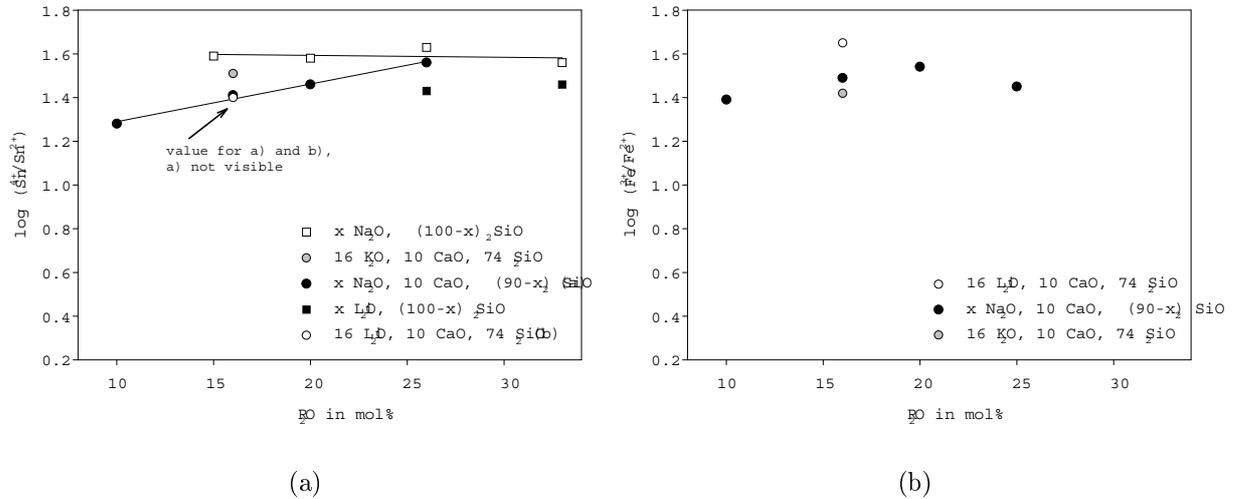
Figure 9.2: Redox ratios of tin (a) and iron (b) at 1300°C as a function of the alkaline earth concentration in silicate melts. Iron redox ratios are taken from Ref. [7, 68, 70].

(see Fig. 9.1(b)). A possible explanation may be given by the different coordination numbers of Sn^{4+} (6) and Fe^{3+} (4) and the different function of the alkali ion in the network: According to Scholze [101], alkali ions possess different coordination numbers in silicate glasses, i.e. $Li^+ = 4$, $Na^+ = 6$, $K^+ = 8$ and thus they form different cavities. Because of the tendency of Sn^{4+} for octahedral coordination, it is necessary to keep in mind that it needs larger cavities to enter the network. Owing to its tetrahedral coordination Fe^{3+} does not have such difficulties to enter a dense network.

The increase in the CaO concentration has at most a minor effect on the Sn^{4+}/Sn^{2+} redox equilibrium. In consequence, it does not seem very reasonable to draw any conclusion on the influence of the CaO concentration. However, the presence of MgO favours slightly the Sn^{2+} state (see Fig. 9.2(a)). MgO is not exclusively a network modifier [101] and accordingly the network is denser. As already outlined above, Sn^{4+} has difficulties to enter a denser network owing to its preference for octahedral coordination. Gerlach et al. [8] have observed that the change in the CaO concentration has a minor effect on the Fe^{3+}/Fe^{2+} redox equilibrium (see Fig. 9.2(b)). In Ref.
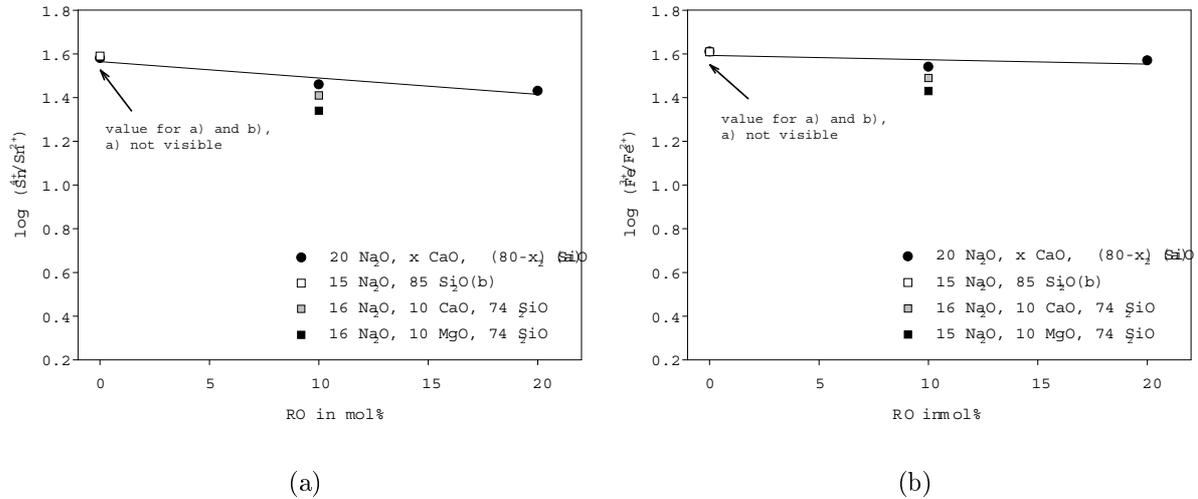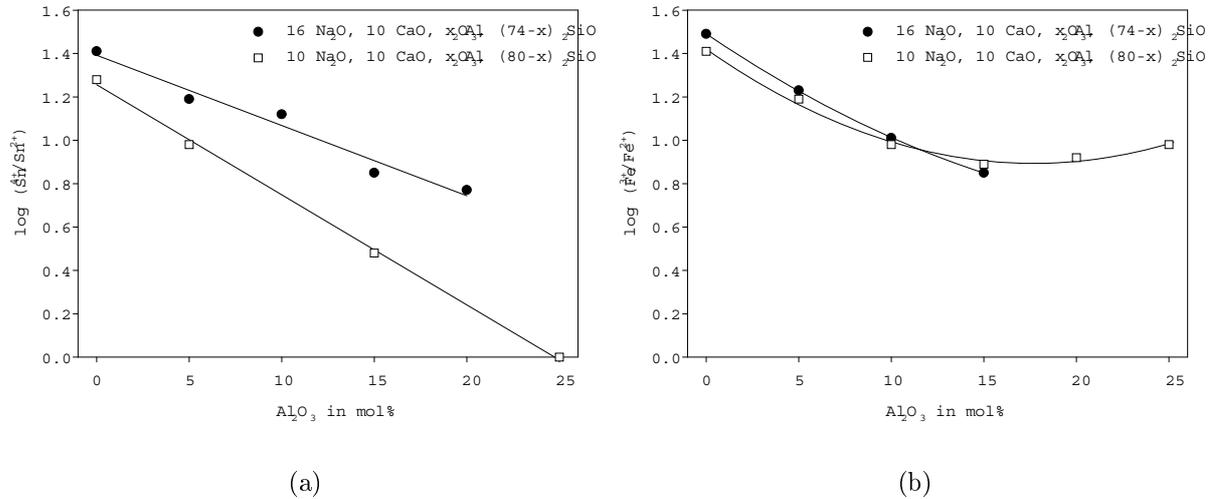
Figure 9.3: Redox ratios of tin (a) and iron (b) at 1300°C as a function of the Al_2O_3 concentration in alumosilicate melts. Iron redox ratios are taken from Ref. [9].

[11, 12, 17] it has been concluded that also Ca^{2+} contributes to the stabilisation of $[FeO_4]^-$ tetrahedra but not MgO.

In alumosilicate melts, a major fraction of tin is present in the Sn^{4+} state. However, the fraction of Sn^{4+} decreases linearly with increasing Al_2O_3 concentration: e.g. at 1300°C for alumosilicates with 16 mol% Na_2O from 96.3 to 85.5 % and for alumosilicate with 10 mol% Na_2O from 95.0 to 50.0%. The variation in the Al_2O_3 concentration exercises a far more pronounced influence on the Sn^{4+}/Sn^{2+}-redox equilibrium than the variation in the alkali concentration and alkaline earth concentration. The change of the Fe^{3+}/Fe^{2+}-redox ratio is found to be of the same order of magnitude but has a different trend at large Al_2O_3 concentrations ($[Al_2O_3] > [Na_2O]$) [9].

In order to discuss the dependency of the redox ratio of polyvalent elements on the Al_2O_3 concentration it is necessary, at first, to give a simplified explanation of the function of Al^{3+} in the glass network: If $[Na_2O]/[Al_2O_3] \gg 1$ —peralkaline range, alumina is incorporated as AlO_4^- tetrahedra and an alkali cation is demanded for charge compensation. If $[Na_2O]/[Al_2O_3] \ll 1$ —peraluminous range, excess alumina can no longer

be incorporated in tetrahedral coordination but in octahedral coordination. Due to the changes in the Al^{3+} coordination, the glass structure and the physical behaviour of glass liquids, e.g. viscosity, change drastically [102, 103]. Such a change in the viscosity is observed for melts 16 Na_2O · 10 CaO · x Al_2O_3 · (74-x) SiO_2 with x = 5, 10, 15, 20: The viscosity increases up to a maximum of 15 mol% Al_2O_3 and decreases again at larger Al_2O_3 concentrations (see Fig. 5.3).

As already outlined above, Fe^{3+} is present as $[FeO_4]^-$ tetrahedra charge compensated by alkali ions. Accordingly, it has been concluded by several authors [9]-[12] that Fe^{3+} and Al^{3+} compete for the charge balancing alkali ions in the peralkaline range: With increasing Al_2O_3 concentrations, increasing quantities of alkali ions are necessary for the charge compensation of the $[AlO_4]^-$ tetrahedra. As a consequence, the alkali ion concentration which is available for the stabilisation of $[FeO_4]^-$ tetrahedra decreases and as a result, the Fe^{3+} concentration decreases. In the peraluminous range the concentration of Fe^{3+} increases again. This is a consequence of the incorporation of Al^{3+} in octahedral coordination, i.e. as a network modifier [16, 17]. In the peralkaline range Sn^{4+}/Sn^{2+} and Fe^{3+}/Fe^{2+}-redox equilibria show the same shift: That is the reduced state is favoured with increasing Al_2O_3 concentration. This analogy implies that also Sn^{4+} competes with Al^{3+} for Na^+ ions as charge balancing ion. This conclusion might further confirm the assumption that $[Sn^{4+}O_6]^{2-}$ octahedra need Na^+ for their stabilisation. Nevertheless, Al^{3+} in octahedral coordination does not shift the redox ratio to the Sn^{4+} state as observed for iron. It seems that Sn^{4+} is tied to the stabilisation by alkali ions due to its octahedral coordination. Fe^{3+} due to its tetrahedral coordination may be easier to charge compensate by higher charged cations. As it is known from $[AlO_4]^-$ tetrahedra a stabilisation by Ca ions is possible. However, the presence of Sn^{2+} is not tied to alkali ions (see above). Sn^{2+} is even known to be present as intermediate or conditional network former in alkali free silicate glasses because of its smaller coordination number [29, 31, 32, 93]. Systematic studies on the incorporation of Sn^{2+} in peraluminous glasses are necessary to provide a better understanding of the

(a)   (b)
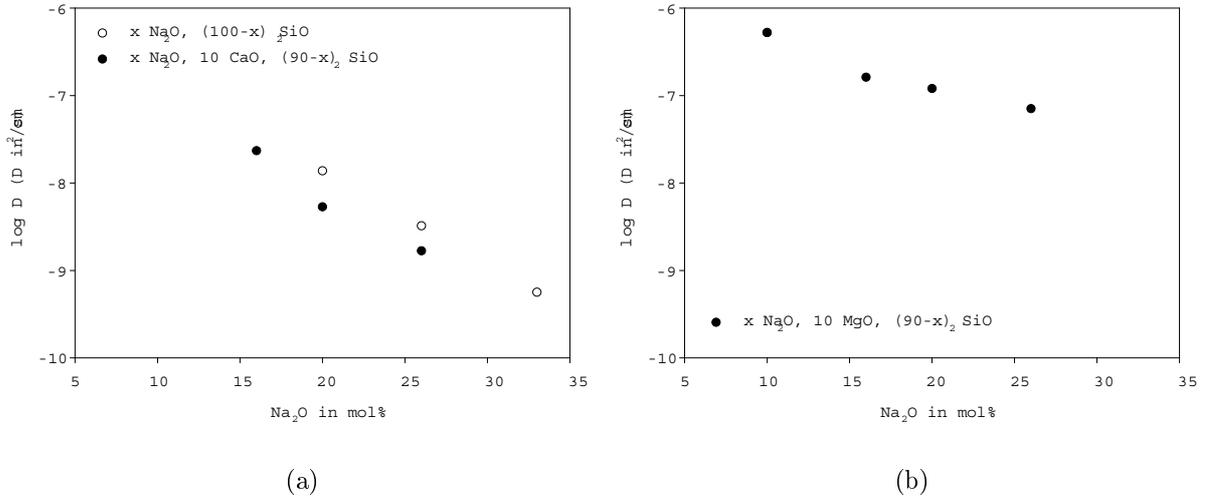
Figure 9.4: Diffusion coefficients of tin (a) and iron (b) at constant viscosities η of 10^3 dPas as a function of the Na_2O concentration in soda- and soda-lime-silicate melts. Data for $33\ Na_2O \cdot 67\ SiO_2$ and iron diffusion coefficients are taken from Refs. [67, 70] and Ref. [68].

function of Sn^{2+} ions.

9.2.2   Diffusion and structure

As already reported in the case of iron diffusion coefficients [13]-[15], the large variation of tin diffusion coefficients can not be described by the Stokes-Einstein equation $D \sim \frac{1}{\eta}$. First of all, the viscosity is attributed to the mobility of the glass network. This gives rise to the question why the mobility of tin at a constant network mobility changes as a function of the glass composition. Regarding various types of glass components such as network modifiers, network formers and polyvalent elements, the diffusion coefficients predominantly depend on their incorporation into the glass structure and vary over several orders of magnitude [13, 104, 105].

For example, in soda-silicate melts the diffusion coefficients decrease at a constant viscosity of 10^3 dPas by almost two orders of magnitude with increasing Na_2O concentration from 20 to 33 mol%: They decrease from $1.38 \cdot 10^{-8}$ to $5.62 \cdot 10^{-10}$ cm^{2}s^{-1}. In

soda-lime-silicate melts the diffusion is found to decrease by around one order of magni-
tude from 16 to 26 mol% Na_2O, i.e. they decrease from $2.34 \cdot 10^{-8}$ to $1.68 \cdot 10^{-9}$ cm^2s^{-1}
(see Fig. 9.4(a)).

The dependency of tin diffusion coefficients on the Na_2O concentration observed in
this work has already been reported in the case of iron diffusion coefficients in alkali-
magnesia-silicate melts (see Fig. 9.4(b)) [14]. A decrease in the iron diffusion coeffi-
cients with larger alkali concentrations was pointed out at constant viscosity. It was
concluded that this effect is caused by the stronger incorporation of Fe^{3+} in the glass
network. Here, Fe^{3+} is forming a distorted tetrahedrally coordinated complex charge
balanced by Na^+ cations. Consequently, a larger Na^+ ion concentration has a more
stabilising effect. According to the result obtained by Mössbauer spectroscopy (see
8.3.2), Sn^{4+} is forming a distorted octahedrally coordinated complex and the character
of the Sn-O bonds in not significantly affected by the variation of the Na_2O concentra-
tion. In section 9.2.1 it has been suggested that this complex may be charge balanced
by Na^+ cations. Also the dependency of the tin and iron diffusion coefficients on the
Na_2O concentration is very similar, thus, it seems reasonable to suppose that a larger
Na^+ ion concentration has in analogy to iron ions a more stabilising effect on tin ions.

In section 7.5 (see Fig. 7.20) it has been described that in soda-lime-silicate melts the
slope —$log\ D$ vs. $log\ \eta$— for the 26 Na_2O · 10 CaO · 64 SiO_2 melt is different from
that for the other compositions. That is due to the fact that the tin diffusion in this
melt is faster than in melts containing less Na_2O at viscosities $log\ \eta\ (\eta/dPas) < 2.5$
—this trend is contrary to the trend described above. By Mössbauer measurements
(chapter 8) it has been concluded that the incorporation of tin in glass is not affected
significantly by the change in the Na_2O concentration (within the composition range
studied). Hence, the behaviour of the 26 Na_2O · 10 CaO · 64 SiO_2 melt described above
cannot be explained by a drastic change in the incorporation of tin. However, it should
be noted that this composition is the only one in which Q^3 and Q^2 tetrahedra coexist
[106], whereas in all other melts, predominantly Q^3 and Q^4 tetrahedra are present. A
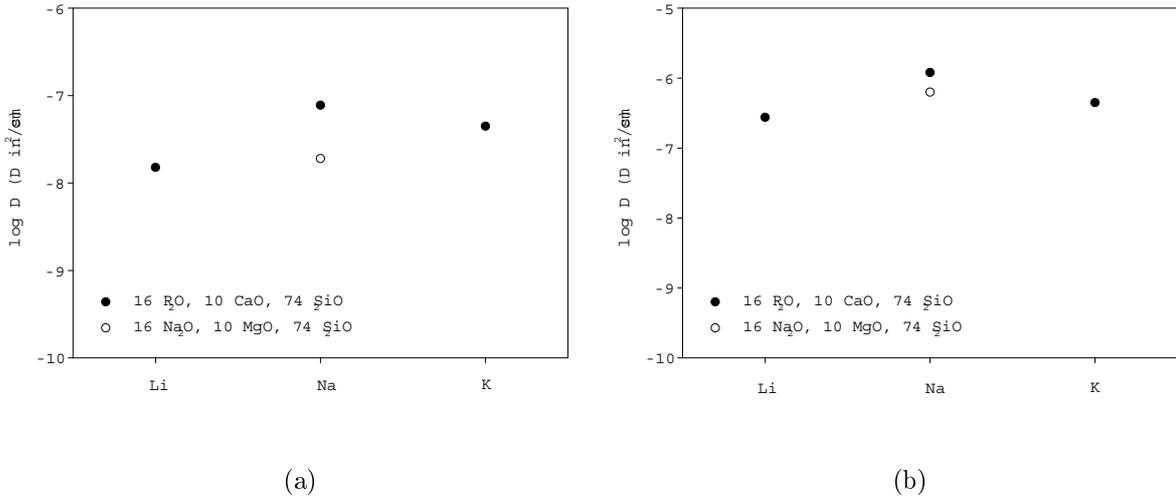
Figure 9.5: Diffusion coefficients of tin (a) and iron (b) at constant viscosities η of $10^{2.5}$ dPas in alkali-alkaline earth-silicate melts. Iron diffusion coefficients and viscosities for 16 $K_2O \cdot 10$ CaO $\cdot$ 74 SiO_2 and 16 $Na_2O \cdot 10$ MgO $\cdot$ 74 SiO_2 are taken from Ref. [68].

similar investigation on the diffusion of iron does not exist to verify this interpretation. However, in soda-lime-silicates the change observed in the thermodynamic behaviour of iron is due to the outlined structural change [7].

In Fig. 9.5(a) variations in the diffusion coefficients in silicate melts with different alkali and alkaline earth oxides are shown at a constant viscosity of $10^{2.5}$ dPas. By changing the alkali ion from Li to Na, the diffusion coefficient increases from $1.51 \cdot 10^{-8}$ to $7.76 \cdot 10^{-8}$ cm^{2}s^{-1}. However, a further increase of the alkali ion radius (Na to K) leads to a comparatively small decrease of the diffusion coefficient ($4.47 \cdot 10^{-8}$ cm^{2}s^{-1}).

Variations in the size of the alkali ion have the same effect on the iron diffusion coefficients in silicate melts (see Fig. 9.5(b)) [68]: By changing the alkali ion from Li to Na, the diffusion coefficient increases from $2.75 \cdot 10^{-7}$ to $1.2 \cdot 10^{-6}$ cm^{2}s^{-1}. However, a further increase of the alkali ion radius (Na to K) leads to a decrease of the diffusion coefficient ($4.46 \cdot 10^{-7}$ cm^{2}s^{-1}). The indicated correlations are explained by the fact that Li has a more stabilising effect on the FeO_4^--tetrahedra due to its larger Coulomb
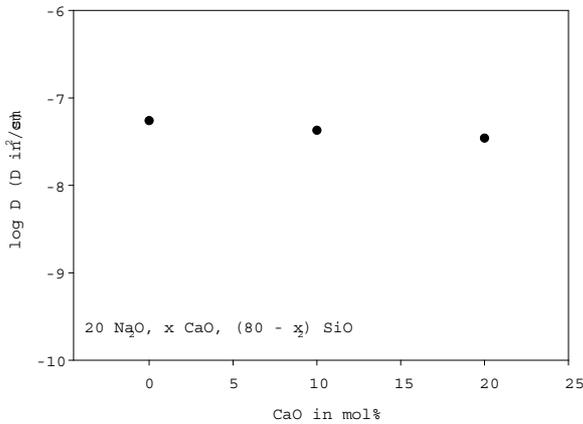
Figure 9.6: Diffusion coefficients of tin a viscosity η of $10^{2.5}$ dPas in soda-lime-silicate melts.

forces [14]. Because tin diffusion coefficients show an analogous trend, the compositional dependency of tin diffusion coefficients may be interpreted in the same way. Nevertheless, the slight decrease in the diffusion coefficients of tin and iron by further increasing the alkali ion size, i.e. from Na to K is, is in contradiction. The variation in the type of alkaline earth (Mg to Ca) leads to an increase in the tin diffusion coefficient, i.e. from $(1.91 \cdot 10^{-8}$ to $7.76 \cdot 10^{-8}$ cm^{2}s$^{-1})$. Here, the effect which has been observed for iron is less pronounced: That is the iron diffusion coefficient increases from $6.31 \cdot 10^{-7}$ to $1.20 \cdot 10^{-6}$ cm^{2}s^{-1} (see Fig. 9.5(a) and 9.5(b)). Accordingly, alkaline earth ions do probably have a minor effect on the tin and iron diffusion coefficients.

Diffusion coefficients as a function of the CaO concentration are plotted at a constant viscosity η of $10^{2.5}$ dPas in Fig 9.6. While increasing the CaO concentration from 0 to 20 mol%, the diffusion coefficients decrease from $5.50 \cdot 10^{-8}$ to $3.47 \cdot 10^{-8}$ cm^{2}s^{-1}. Hence, the variation of the diffusion due to changes of the melt composition is almost negligible. In consequence, it may be concluded that variations in the CaO concentration have at most only minor contribution to the diffusion coefficients. However, the Sn^{2+} fraction is slightly larger as the CaO concentration is increased. Unfortunately there is no comparable study of the diffusion coefficients of iron.

The variation in the tin diffusion as a function of the Al$_2$O$_3$ concentration is shown at a

constant viscosity η of 10^3 dPas in Fig. 9.7(a). In melts with 16 mol% Na_2O, the diffusion coefficients increases from $2.34\cdot10^{-8}$ (0 mol% Al_2O_3) to $2.24\cdot10^{-7}$ cm^2s^{-1} (15 mol% Al_2O_3). Alumosilicate melts with 10 mol% Na_2O show the same dependency of the Al_2O_3 concentration: The tin diffusion coefficient increases from $8.51\cdot10^{-8}$ cm^2s^{-1} (5 mol% Al_2O_3) to $3.47\cdot10^{-7}$ cm^2s^{-1} (15 mol% Al_2O_3).

This dependency of tin diffusion coefficients on the Al_2O_3 concentration observed in the present work was already reported in the case of iron diffusion coefficients (see Fig. 9.7(b)) [68]. An increase in the iron diffusion coefficients from $2.88\cdot10^{-7}$ (0 mol% Al_2O_3) to $6.61\cdot10^{-7}$ cm^2s^{-1} (15 mol% Al_2O_3) is found. This correlation was interpreted in the following manner: By introducing alumina, which is incorporated as $[AlO_4]^-$ tetrahedra charge compensated by Na^+, the $[FeO_4]^-$-tetrahedra are less stabilised, because an increasing fraction of Na^+ is demanded for the Al stabilisation. (The incorporation of Al_2O_3 is outlined in section 9.2.1.) Since $[FeO_4]^-$ is the least mobile iron species, the mobility of iron increases and consequently the diffusion process is faster [15]-[17]. Now the question is which effect gives rise to the changes of the tin diffusion coefficients as the composition is varied. It is assumed that Sn^{4+} is forming a distorted octahedral coordinated complex which is charge balanced by alkali ions. It has been discussed in section 9.2.1 that an increase in the Al_2O_3 concentration — a decrease in the availability of alkali— destabilises Sn^{4+}. In other words, the tin diffusion increases.

A further increase in the Al_2O_3 concentration leads to a decrease in the tin diffusion ($9.12\cdot10^{-8}$ cm^2s^{-1}). This decrease in the diffusion coefficient runs parallel with a change in the Al^{3+} coordination. (see section 9.2.1). However, Al octahedra do not stabilise Sn^{4+} but an increasing fraction of Sn^{2+} is stabilised. Accordingly, the decrease in the diffusion coefficient may be caused by a better stabilisation of Sn^{2+}. Sn^{2+} is known to act not exclusively as a network modifier but also as a intermediate or even as a conditional network former [29, 31, 32, 93]. However, there are further investigations necessary to verify this hypothesis.
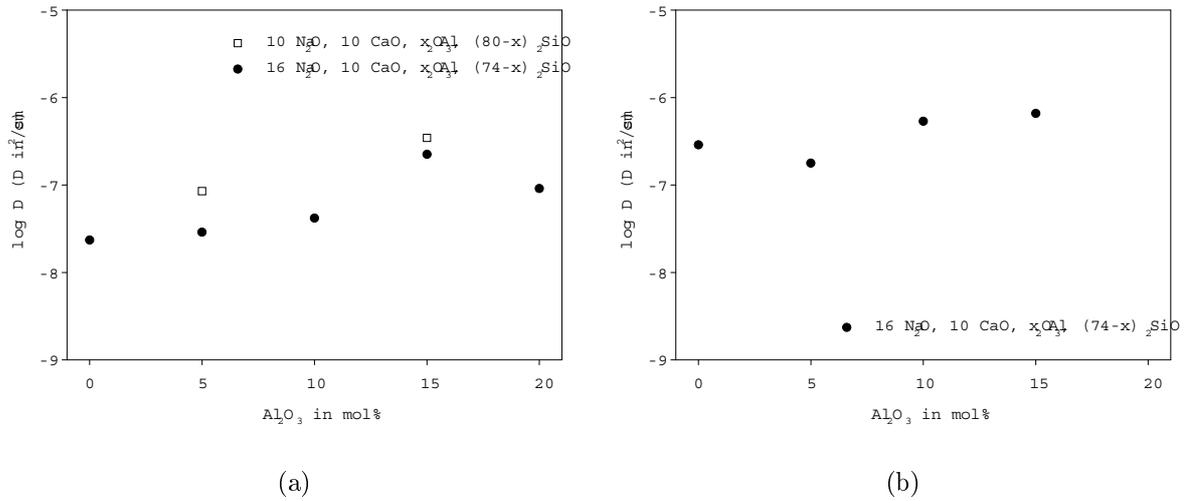
Figure 9.7: Diffusion coefficients of tin (a) and iron (b) at constant viscosities η of 10^3 as a function of the Al_2O_3 concentration in alumosilicate melts. Iron diffusion coefficients and viscosities for 16 Na_2O · 10 CaO · 5 Al_2O_3 · 69 SiO_2–16 Na_2O · 10 CaO · 15 Al_2O_3 · 59 SiO_2 are taken from Ref. [68].

In this context, it is appropriate to make some remarks concerning the interpretation of the Mössbauer parameters of Sn^{4+} as a function of the Al_2O_3 concentration: In section 8.3.2 it has been concluded that the increase in the s-electron density —as the Al_2O_3 concentration is increased— is rather caused by an elongation of the Sn^{4+}-O bonds than by a change in the degree of covalency. Therefore, the simultaneous increase in the tin diffusion coefficients might support this interpretation.

Since the diffusion coefficients of tin are smaller than those of iron, it is concluded that the incorporation of tin in the glass network is stronger than that of iron. Hence, tin ions possess a larger network forming ability than iron ions. This goes along with the fact that octahedrally coordinated Sn^{4+} ions have a higher field strength (0.94) than tetrahedrally coordinated Fe^{3+} ions (0.85) [107].

9.3 Conclusions on the fining behaviour

Conclusions on the fining behaviour of Sn^{4+} compounds can be drawn from the dependency of the peak potential on temperature. Oxygen gas evolution takes place, if the oxygen activity of a melt exceeds the value attributed to an oxygen fugacity of 1 bar. The maximum gas evolution is at a Sn^{4+}/Sn^{2+} ratio equal to unity. Temperatures for maximum formation of oxygen bubbles can be obtained from linear extrapolation of the data shown in Figs. 7.1–7.7. This temperature is $\sim$1700°C for the composition $16\ Na_2O \cdot 10\ CaO \cdot 74\ SiO_2$. For the other alkali-alkaline earth silicate glass compositions the temperature of bubble formation is similar ($\pm$45K). However, a lower fining temperature of 1625°C has been found for the K_2O containing glass. This is caused by the larger standard entropy of the Sn^{4+}/Sn^{2+} reaction (see Table B.1). In alumosilicates even lower temperatures for maximum bubble formation have been obtained, e.g. for the composition $16\ Na_2O \cdot 10\ CaO \cdot 20\ Al_2O_3 \cdot 54\ SiO_2$ $\sim$1575°C. In the peraluminous glass composition $10\ Na_2O \cdot 10\ CaO \cdot 25\ Al_2O_3 \cdot 55\ SiO_2$ this temperature has even shifted to $\sim$1300°C.

Tin compounds are fining agents giving raise to bubble formation at temperatures far larger than more convenient fining agents such as As_2O_5, Sb_2O_5 or Na_2SO_4. It should be noted, however, that in oxidised melts, i.e. those with a Sn^{4+}/Sn^{2+} ratio much larger than unity, smaller quantities of bubbles are already formed at lower temperatures. Nevertheless, the temperatures necessary for effective fining are not reached in convenient glass tanks. However, Sn^{4+} compounds are promising candidates for high temperature fining in e.g. peralkaline alumosilicate melts.

Chapter 10

Summary

Both, electrochemical and Mössbauer spectroscopic measurements have been carried out at high temperatures in alkali-alkaline earth-silicates and alumosilicates. The alkali concentration, the type of alkali, the alkaline earth concentration, the type of alkaline earth and the Al_2O_3 concentration have been varied. The determination of thermodynamics of redox equilibria, diffusion coefficients, Mössbauer parameters and Debye temperatures as a function of the glass composition should contribute to a better understanding of the structural incorporation of tin in silicate melts.

In order to provide at first an understanding of the mechanism of the electrode reaction, a soda-silicate melt has been investigated by means of **square-wave voltammetry** and **electrochemical impedance spectroscopy**: The square-wave voltammograms recorded at larger temperatures show one pronounced peak. By contrast, the appearance of a second peak is observed at smaller temperatures and shorter step times. The peak appearing at all temperatures is due to a fully reversible electrode reaction, whereas the peak appearing in addition at lower temperatures and shorter step times is not caused by an electrode reaction controlled by diffusion. The impedance spectra at larger temperatures have been simulated using a simple equivalent circuit in which the Warburg impedance accounts for a diffusion controlled electron transfer reaction. At smaller temperatures the impedance spectra had to be simulated by an equivalent

circuit with an additional resistance and capacitance accounting for absorption. The minima in the Warburg impedance-dc-potential dependency and the peak potentials observed by SWV have been attributed to the same electrode reaction. According to results of electrolysis and Mössbauer spectroscopy, this reaction has been assigned to the Sn^{4+}/Sn^{2+} redox pair. Potentials which are observed at the maxima in the adsorption capacitance-dc-potential dependency and the peak potentials of the peak appearing only at lower temperature are assigned to an adsorbed state. The adsorption of SnO_x on a Pt-electrode at high temperatures has been shown for the first time.

The peak potentials attributed to the redox pair Sn^{4+}/Sn^{2+} have been found to decrease linearly with temperature. This is attributed to a shift of the redox equilibrium to the Sn^{4+} state. The linear correlation between peak potential and temperature enables the determination of the standard enthalpy ΔH^0, standard entropy ΔS^0. **Oxygen activity measurements** provide an alternative method to determine the standard enthalpy ΔH^0. A good agreement between the standard enthalpies ΔH^0 determined by both, SWV and oxygen activity measurements has been obtained. Besides, the knowledge of the oxygen activity and the thermodynamic standard data enables the determination of oxidation states at high temperatures. It has been determined that the equilibrium state has been reached for the investigated peralkaline melts.

The peak potentials determined in lithium oxide- and soda-silicate melts do not depend within the limits of error on the alkali concentration. Therefore, the change of the alkali concentration has no significant influence on the redox equilibrium. By contrast, for soda-lime-silicate melts, the dependency of the peak potentials on the Na_2O concentration is linear within the limit of error. That is, the oxidised state is favoured with increasing alkali concentration. An increase in the size of the alkali ion leads to more negative standard potentials in alkali-silicate melts. Accordingly, a higher fraction of Sn^{4+} is formed. However, in alkali-lime-silicate melts a pronounced effect has been observed only in the case of Na to K. An increase in the CaO concentration or the replacement of CaO by MgO shifts the peak potentials to slightly larger values.

Increasing Al_2O_3 concentrations lead as well to larger peak potentials. That means, a higher fraction of Sn^{2+} is formed. The variation in the Al_2O_3 concentration has the most pronounced effect on the redox equilibrium. Sn^{4+} has been the dominating species in almost all glass compositions.

In soda-silicate and soda-lime-silicate melts the diffusion coefficients decrease at a constant viscosity with increasing Na_2O concentration. The variation in the diffusion coefficients as a function of the CaO concentration is almost negligible. Also the effect due to a change of the alkali oxide or the alkaline earth oxide is small compared to changes of the Na_2O concentration. However, the variation in the diffusion coefficients due to an increase in the Al_2O_3 concentration has the same order of magnitude as the variation in the diffusion coefficients which has been observed in soda-silicate melts by varying the Na_2O concentration. By contrast, an increase in the Al_2O_3 concentration leads to an increase in the diffusion coefficients in the peralkaline range.

In soda-lime-silicates, the **Mössbauer spectra** of tin doped glasses show an asymmetric doublet due to Sn^{2+} with a large quadrupole splitting and a symmetrical doublet due to Sn^{4+} with a small quadrupole splitting. The isomer shifts of Sn^{2+} decrease with increasing Na_2O concentration accompanied by an increase in the quadrupole splitting. This is interpreted in terms of slightly increasing covalency of the Sn-O bonds. The isomer shifts of Sn^{4+} are constant within the limits of error. In alumosilicates the spectra are composed of asymmetric subspectra due to both Sn^{2+} and Sn^{4+}. For Sn^{2+} the isomer shifts are observed to be constant within the limits of error. Nevertheless, the quadrupole splitting increases with increasing Al_2O_3 concentration. This is probably due to an increasing asymmetry of the ligands. For Sn^{4+}, the isomer shifts increase with increasing Al_2O_3 concentration which corresponds to an increase in the number of 5s-electrons. This observation is accompanied by an increase in the quadrupole splitting. It has been concluded that Sn^{2+} most probably possesses a fourfold coordination similar to that of tin in amorphous SnO. Sn^{4+} has a preference to a distorted octahedral position with strongly ionic bonding. The Debye temperatures of both Sn^{4+}

($\sim$263K) and Sn^{2+} ($\sim$187K) do not change within the limits of error with increasing Na_2O concentration.

The effect of the glass composition on the Sn^{4+}/Sn^{2+} redox equilibrium and the tin diffusion has been compared with similar studies on iron. Analogous trends in the Sn^{4+}/Sn^{2+} and Fe^{3+}/Fe^{2+} redox equilibrium and in the tin and iron diffusion coefficients with variation of the glass composition have implied a tendency of Sn^{4+} for forming a distorted octahedrally coordinated complex which might be charge balanced by Na^+ ions.

Applying Sn^{4+} compounds as fining agents the formation of oxygen bubbles is maximum at temperatures far higher than those of convenient fining agents.

Bibliography

[1] Ehrt, D., Leister, M. and Matthai, A., Molten Salt Forum **5-6** (1998) 547.

[2] Townsend, P.O., Can, N., Chandler, P.J., Farmery, B.W., Lopez-Heredero, R., Peto, A., Salvin, L., Underdown, D. and Yang, B., J. Non-Cryst. Solids **223** (1998) 73.

[3] Williams, K.F.E., Johnson, C.E., Nikolov, O., Thomas, M.F., Johnson, J.A. and Greengrass, J., J. Non-Cryst. Solids **242** (1998) 183.

[4] Naumann, K., Ott, F., Diezel, R. and Becker, O. Patent DE 100 34 985 C 1 (2001).

[5] Duffy, J.A., J. Non-Cryst. Solids **196** (1996) 45.

[6] Paul, A. and Douglas, R. W., Phys. Chem. Glasses **6** (1965) 207.

[7] Rüssel, C., Glastech. Ber. **66** (1993) 93.

[8] Gerlach, S., Claußen, O. and Rüssel, C., J. Non-Cryst. Solids **238** (1998) 75.

[9] de Strycker, J., Gerlach, S., von der Gönna, G. and Rüssel, C., J. Non-Cryst. Solids **272** (2000) 131.

[10] Wiedenroth, A. and Rüssel, C., J. Non-Cryst. Solids **290** (2001) 41.

[11] Wiedenroth, A. and Rüssel, C., J. Non-Cryst. Solids **318** (2003) 79.

[12] Wiedenroth, A. and Rüssel, C., J. Non-Cryst. Solids **320** (2003) 238.

[13] Claußen, O. and Rüssel, C., Solid State Ionics **105** (1998) 289.

[14] Gerlach, S., Claußen, O., and Rüssel, C., J. Non-Cryst. Solids **226** (1998) 11.

[15] Gerlach, S., Claußen, O., and Rüssel, C., J. Non-Cryst. Solids **240** (1998) 110.

[16] Wiedenroth, A. and Rüssel, C., Phys. Chem. Glasses **43** (2002) 7.

[17] Wiedenroth, A. and Rüssel, C., J. Non-Cryst. Solids **297** (2002) 173.

[18] Schreiber, H.D., J. Non-Cryst. Solids **84** (1986) 129.

[19] Takahashi, K. and Miura, Y., J. Non-Cryst. Solids **38&39** (1980) 527.

[20] Takahashi, K. and Miura, Y., Glastech. Ber. **56K** (1983) 928.

[21] Rüssel, C., Phys. Chem. Glasses **32** (1991) 138.

[22] Lee, J.H. and Brückner, R., Glastech. Ber. **57** (1984) 7.

[23] Paul, A. and Lahiri, D., J. Am. Ceram. Soc. **49** (1966) 565.

[24] Hirashima, H., Yoshida, T. and Brückner, R., Glastech. Ber. **61** (1988) 283.

[25] Nishida, T., J. Non-Cryst. Solids **177** (1994) 257.

[26] Nishida, T., Radioanalytical and Nuclear Chemistry **182** (1994) 451.

[27] Nishida, T., Hyperfine Interactions **95** (1995) 23.

[28] Ehrt, D., Leister, M. and Matthai, A., Phys. Chem Glasses **42** (2001) 231.

[29] Johnson, J.A., Johnson, C.E., Williams, K.F.E, Holland, D. and Karim, M.M., Hyperfine Interactions **95** (1995) 41.

[30] Dannheim, H., Oel, H.J. and Tomandl, G., Glastech. Ber. **49** (1976) 170.

[31] Williams, K.F.E, Johnson, C.E., Johnson, J.A., Holland, D. and Karim, M.M., J. Phys.: Condens. Matter **7** (1995) 9485.

[32] Johnson, J.A., Johnson, C.E., Holland, D., Sears, A., Bent, J.F., Appleyard, P.G., Thomas, M.F. and Hannon, A.C., J. Phys.: Condens. Matter **12** (2000) 213.

[33] Schultz-Münzenberg, C., *Bindungszustände von polyvalenten Zusätzen in einfachen oxidischen Gläsern*, PhD thesis, Mainz, 1998.

[34] Appleyard, P.G., Johnson, J.A., Johnson, C.E., Thomas, M.F., Holland, D. and Sears, A., J. Phys.: Condens. Matter **9** (1997) 7477.

[35] Lechtenböhmer, A., Mosel, B.D., Müller-Warmuth, W. and Dutz, H., Glastech. Ber. **55** (1982) 161.

[36] Williams, J.M., Forder, S.D. and Isard, J.O., Struct. Non-Cryst. Mater. Proc. Int. Conf., 2nd (1983) 221.

[37] Paul, A., Donaldson, J.D., Donoghue, M.T. and Thomas, M.J.K., Phys. Chem. Glasses **18** (1977) 125.

[38] Nishida, T., Katada, M., Osawa, N., Sato, R., Komatsu, T. and Matusita, K., Hyperfine Interactions **94** (1994) 2119.

[39] Gao, M., Zhang, Z., Li, L. Li, X. and Takahashi, K., J. Non-Cryst. Solids **80** (1986) 319.

[40] Johnston, W.D., J. Am. Ceram. Soc. **48** (1965) 184.

[41] Rüssel, C., J. Non-Cryst. Solids **119** (1990) 303.

[42] Osteryoung, J.G. and Osteryoung, R.A., Anal. Chem. **57** (1985) 101A.

[43] Osteryoung, J.G and O'Dea, J.J in A.J. Bard, (ed.), Electroanalytical Chemistry **14**, Marcel Dekker New York (1986) 209.

[44] Economou, A. and Fielden, P.R., Anal. Chim. Acta **273** (1993) 27.

[45] Barker G.C., Anal. Chim. Acta **18** (1958) 118.

[46] Claußen, O., *Square-Wave Voltammetrie zur Bestimmung polyvalenter Ionen in Glasschmelzen*, PhD thesis, Jena, 1996.

[47] Freude, E., *Voltammetrische Untersuchung des Redoxverhaltens polyvalenter Ionen in Glasschmelzen, insbesondere von Technetium*, PhD thesis, Nürnberg-Erlangen, 1989.

[48] Montel, C., Rüssel, C. and Freude, E., Glastech. Ber. **61** (1988) 59.

[49] Frey, T., Schaeffer, H.A. and Baucke, F.G.K., Glastech. Ber. **53** (1980) 116.

[50] Tran, T., Brungs, M.P., Phys. Chem. Glasses **21** (1980) 133 and 178.

[51] Kohl, R. and Schaeffer, H.A., Diffusion Defect Data **53/54** (1987) 325.

[52] Lenhart, A. and Schaeffer, H.A., Glastech. Ber. **58** (1985) 139.

[53] Rüssel, C., Kohl, R. and Schaeffer, H.A., Glastech. Ber. **61** (1988) 209.

[54] Ravagnani, C., Keding, R. and Rüssel, C., Glastech. Ber. Glass Sci. Technol. **73 C2** (2000) 166.

[55] Rüssel, C., Glastech. Ber. **64** (1991) 123.

[56] Keding, R. and Rüssel, C., Proc. Europ. Soc. Glass Technol. 5. Conf. "Glass Science and Technology" **C4** (1999) 33.

[57] Göhr, H., I.S.E. Meeting, Ext. Abstracts, Erlangen (1983).

[58] Brooks, J.S., Williams, G.L., Allen, D.W. and de Grave, E., Phys. Chem. Glasses **33** (1992) 167.

[59] Hayes, C., in "Chemical Applications of Mössbauer Spectroscopy", V.I. Goldanskii and R.H. Herber (eds.), Academic press, N.Y., London (1968) 314.

[60] Flinn, P.A., in "Mössbauer Isomer shifts", G.K. Shenoy and F.E. Wagner (eds.) (1978) 593.

[61] Lees, J. and Flinn, P.A., Phys. Letters **19** (1965) 136.

[62] Müller-Simon, H., *Die elektrochemische Sauerstoffaktivitätsmessung in industriellen Glasschmelzanlagen*, PhD thesis, Berlin, 1992.

[63] Wissmann, S., *In Situ Mössbauerspektroskopie zur Kationenverteilung in $(Fe,Mn)_3O_4$-Spinellen und zur Diffusion in Fe_2SiO_4*, PhD thesis, Hannover, 1994.

[64] Wissmann, S. and Becker, K.D., Solid State Ionics **85** (1996) 279.

[65] Lagarec, K. and Rancourt, D.G., "Recoil-Mössbauer Spectral Analysis Software for Windows", Ottawa (1998).

[66] Vogel, W., Glaschemie, Springer Verlag Berlin Heidelberg (1992).

[67] Leister, M., *Das Verhalten polyvalenter Ionen in Silicatgläsern im Hochtemperaturbereich (1400–2000°C)*, PhD thesis, Jena, 2000.

[68] Gerlach, S., *Diffusion von Eisen in Alkali-Magnesium-Silicat- und Alkali-Calcium-Alumosilicatglasschmelzen*, Diploma thesis, Jena, 1997.

[69] Claußen, O. and Rüssel, C., Glastech. Ber. Glass Sci. Technol. **69** (1996) 95.

[70] von der Gönna, G., *Voltammetrische Untersuchungen in Natron- und Alumosilicatglasschmelzen*, PhD thesis, Jena, 2000

[71] Durussel, P.H., Massara R. and Feschotte, P., J. Alloys and Compounds **215** (1994) 175.

[72] Macdonald, J.R. and Johnson, W.B. Fundamentals of Impedance Spectroscopy, Jon Wiley & Sons, New York (1987).

[73] Neeb, R. and Hinkel, S., Z. Anal. Chem. **262** (1972) 343.

[74] Mandler, D. and Bard, A.J., J. Electroanal. Chem. **307** (1991) 217.

[75] Retter, U., and Lohse, H., in "Electroanalytical Methods", Scholz, F. (ed.) Springer Berlin Heidelberg New York (2002) 149.

[76] Bard, A.J. and Faulkner, L.R., J. Electrochemical methods. Wiley, New York 1980.

[77] Cossement, C., Darville, J., Gilles, J.M., Nagh, J.B., Fernandez, C. and Amoureux, J.P., Magnetic Resonance in Chemistry **30** (1992) 263.

[78] van den Berg, J.M., *Acta Cryst.* 14/15 (1961/62) 1002/1051.

[79] Ansbach, O., *Personal Communication.*

[80] Mazurin, O.V., Streltsina, M.V. and Shvaiko-Shvaikovskaya, T.P., Handbook of glass data, Part A, Silica glass and binary silicate glasses, Elsevier Amsterdam. (1983) 109.

[81] Rancourt, D.G. and Ping, J.Y., Nucl. Instrum. Meth. Phys. Res. **B58** (1991) 85.

[82] Collins, G.S., Kachnowski, T., Benczer-Koller, N. and Pasternak, M., Phys. Rev. B **19** (1979) 1369.

[83] Wyckoff, R.W.G., Crystal Structure, Interscience, New York (1965) 134.

[84] Panyushkin, V.N., Soviet Phys.-Solid State **10** (1968) 1515.

[85] Appleyard, P.G., Transfer Report, Liverpool John Moores University (1996).

[86] Donaldson, J.D. and Senior, B.J., J. Chem. Soc. **A** (1966) 1798.

[87] Niemeier, D., Mehner, H., U. Bismayer and K.D. Becker, Phys. Stat. Sol. (b) **211** (1999) 581.

[88] Schatz. G. and Weidinger, A. "Nukleare Festkörperphysik", Teubner Stuttgart (1997) 64.

[89] Baur, W.H., Acta Crystallogr. **9** (1956) 515.

[90] Takahashi, K., Mochida, N. and Yoshida, Y., Yogyo Kyokaishi **85** (1977) 330.

[91] Stemprok, M. and Voldan, J., Silikaty **31** (1987) 1.

[92] Williams, K.F.E., Johnson, C.E., Greengrass, J., Tilley, B.P., Gelder, D. and Johnson, J.A., J. Non-Cryst. Solids **211** (1997) 164.

[93] Bent, J.F., Hannon, A.C., Holland, D. and Karim, M.M.A., J. Non-Cryst. Solids **232-234** (1998) 300.

[94] Duffy, J.A., Phys. Chem. Glasses **40** (1999) 54.

[95] Yamashita, H., Shimaoka, S. and Maekawa, T., J. Ceramic Soc. Japan **106** (1998) 724.

[96] Mitrofanov, K.P. and Sidorov, T.A., Soviet Physics — Solid State **9** (1967) 693.

[97] Vakhrameev, V.I., Evstrop'ev, K.S., Neorganicheskie Materialy **5** (1969) 101.

[98] Yamashita, H., Shimaoka, S., Yamaguchi, S., and Maekawa, T., J. Ceramic Soc. Japan **107** (1999) 385.

[99] Takeda, S., Akiyama, R. and Hosono, H., J. Non-Cryst. Solids **281** (2001) 1.

[100] Lang, G., Z. anorg. allg. Chem. **276** (1954) 77.

[101] Scholze, H., Glas: Natur, Struktur und Eigenschaften, Springer Berlin (1988)

[102] Riebling, E.F., J. Chem. Phys. **44** (1966) 2857.

[103] Engelhardt, G., Nofz, M., Forkel, F.G., Wishmann, M., Magi, A., Samoson, E. and Lippmaa, E., Phys. Chem. Glasses **26** (1985) 157.

[104] Claußen, O. and Rüssel, C., J. Non-Cryst. Solids **215** (1997) 68.

[105] Müller-Simon, H. and Mergler, K.W., Glastech. Ber. Glass Sci. Technol. **68** (1995) 273.

[106] Jones, A.R., Winter, R., Greaves, G.N., Smith, I.H., J. Non-Cryst. Solids **293-295** (2001) 87.

[107] Dietzel, A., Z. Elektrochem. **48** (1942) 9.

Appendix A

Glass data

Table A.1: Properties of the glass samples

Composition (mol%)	ρ (g·cm^{-3})	T$_g$ (°C)	$\alpha_{100/400}$ (10^{-7}K^{-1})
33 Li$_2$O · 67 SiO$_2$	2.353	463	118
15 Na$_2$O · 85 SiO$_2$*	2.343	485	75
20 Na$_2$O · 80 SiO$_2$	2.398	470	105
26 Na$_2$O · 74 SiO$_2$	2.476	462	137
33 Na$_2$O · 67 SiO$_2$*	2.491	460	160
10 Na$_2$O · 10 CaO · 80 SiO$_2$	2.445	567	77
16 Na$_2$O · 10 CaO · 74 SiO$_2$	2.503	534	100
20 Na$_2$O · 10 CaO · 70 SiO$_2$	2.538	520	116
26 Na$_2$O · 10 CaO · 64 SiO$_2$	2.607	520	138
16 K$_2$O · 10 CaO · 74 SiO$_2$	2.470	600	107
16 Na$_2$O · 10 MgO · 74 SiO$_2$	2.435	491	106
20 Na$_2$O · 20 CaO · 60 SiO$_2$	2.677	551	122
16 Na$_2$O · 10 CaO · 5 Al$_2$O$_3$ · 69 SiO$_2$	2.508	562	98
16 Na$_2$O · 10 CaO · 10 Al$_2$O$_3$ · 64 SiO$_2$	2.547	590	97
16 Na$_2$O · 10 CaO · 15 Al$_2$O$_3$ · 59 SiO$_2$	2.546	635	93
16 Na$_2$O · 10 CaO · 20 Al$_2$O$_3$ · 54 SiO$_2$	2.563	688	94
10 Na$_2$O · 10 CaO · 5 Al$_2$O$_3$ · 75 SiO$_2$	2.466	605	75
10 Na$_2$O · 10 CaO · 15 Al$_2$O$_3$ · 65 SiO$_2$	2.507	692	72
10 Na$_2$O · 10 CaO · 25 Al$_2$O$_3$ · 55 SiO$_2$	2.512	783	52

*) Data are taken from Ref. [67].

Table A.2: Vogel-Fulcher-Tamman parameter of the glass melts

Composition(mol%)	A	B(K)	$T_0(°C)$
20 Na_2O · 80 SiO_2	-0.695	2940	406
26 Na_2O · 74 SiO_2	-2.325	5784	17
33 Na_2O · 67 SiO_2[a]	-1.548	3869	156
16 Na_2O · 10 CaO · 74 SiO_2	-0.474	2836	368
20 Na_2O · 10 CaO · 70 SiO_2	-0.347	2498	360
26 Na_2O · 10 CaO · 64 SiO_2	-0.595	1406	466
16 Li_2O · 10 CaO · 74 SiO_2	-1.934	5351	1
16 K_2O · 10 CaO · 74 SiO_2[b]	-1.948	4763	291
16 Na_2O · 10 MgO · 74 SiO_2[b]	-2.302	5925	104
20 Na_2O · 20 CaO · 60 SiO_2	-0.279	1360	593
16 Na_2O · 10 CaO · 5 Al_2O_3 · 69 SiO_2[b]	-2.053	5409	190
16 Na_2O · 10 CaO · 10 Al_2O_3 · 64 SiO_2[b]	-3.700	8914	45
16 Na_2O · 10 CaO · 15 Al_2O_3 · 59 SiO_2[b]	-5.351	11644	10
16 Na_2O · 10 CaO · 20 Al_2O_3 · 54 SiO_2	-2.990	6588	285
10 Na_2O · 10 CaO · 5 Al_2O_3 · 75 SiO_2	-2.454	6936	140
10 Na_2O · 10 CaO · 15 Al_2O_3 · 65 SiO_2	-23.876	125389	-3172

[a]) Data are taken from Ref. [67]. [b]) Data are taken from Ref. [68].

Appendix B

Thermodynamic & diffusion data

Table B.1: Peak potentials, thermodynamic data and redox ratios for the reaction $\frac{1}{2}Sn^{4+} + e^{-} \rightleftharpoons \frac{1}{2}Sn^{2+}$ (T = 1300°C, p_{O_2} = 0.21 bar).

Composition	[SnO$_2$]	E_P	ΔH^0	ΔS^0	$\log\left(\frac{Sn^{4+}}{Sn^{2+}}\right)$
(mol%)	(mol%)	(mV)	(kJmol^{-1})	(Jmol^{-1}K^{-1})	
26 Li$_2$O · 74 SiO$_2$	0.5	-223	105.5	50.0	1.43
33 Li$_2$O · 67 SiO$_2$	0.5	-227	96.0	44.0	1.46
15 Na$_2$O · 85 SiO$_2$*^{a}	0.5	-248	115.5	55.0	1.59
20 Na$_2$O · 80 SiO$_2$	0.25	-247	113.0	53.5	1.58
20 Na$_2$O · 80 SiO$_2$	0.5	-245	112.0	53.0	1.57
20 Na$_2$O · 80 SiO$_2$	1.0	-246	114.0	54.0	1.58
26 Na$_2$O · 74 SiO$_2$	0.25	-254	118.5	56.5	1.63
33 Na$_2$O · 67 SiO$_2$*	0.5	-243	108.0	50.5	1.56
10 Na$_2$O · 10 CaO · 80 SiO$_2$	0.25	-200	97.5	46.5	1.28
16 Na$_2$O · 10 CaO · 74 SiO$_2$	0.25	-220	107.0	51.0	1.41
20 Na$_2$O · 10 CaO · 70 SiO$_2$	0.25	-227	104.0	49.0	1.46
26 Na$_2$O · 10 CaO · 64 SiO$_2$	0.25	-243	105.5	49.0	1.56

*) Data are taken from Ref. [70]. ^{a}) Values are extrapolated.

Composition (mol%)	$[SnO_2]$ (mol%)	E_P (mV)	ΔH^o (kJmol^{-1})	ΔS^o (Jmol^{-1}K^{-1})	$\log\left(\frac{Sn^{4+}}{Sn^{2+}}\right)$
16 Li$_2$O · 10 CaO · 74 SiO$_2$	0.25	-218	102.0	48.5	1.40
16 K$_2$O · 10 CaO · 74 SiO$_2$	0.25	-235	133.5	67.0	1.51
16 Na$_2$O · 10 MgO · 74 SiO$_2$	0.25	-209	103.5	50.0	1.34
20 Na$_2$O · 20 CaO · 60 SiO$_2$	0.5	-223	104.0	49.0	1.43
16 Na$_2$O · 10 CaO · 5 Al$_2$O$_3$ · 69 SiO$_2$	0.5	-186	101.5	50.0	1.19
16 Na$_2$O · 10 CaO · 10 Al$_2$O$_3$ · 64 SiO$_2$	0.25	-175	97.5	48.0	1.12
16 Na$_2$O · 10 CaO · 15 Al$_2$O$_3$ · 59 SiO$_2$	0.5	-133	88.5	45.0	0.85
16 Na$_2$O · 10 CaO · 20 Al$_2$O$_3$ · 54 SiO$_2$	0.5	-120	80.0	40.0	0.77
10 Na$_2$O · 10 CaO · 5 Al$_2$O$_3$ · 75 SiO$_2$	0.5	-152	95.5	48.0	0.98
10 Na$_2$O · 10 CaO · 15 Al$_2$O$_3$ · 65 SiO$_2$	0.5	-75	77.5	41.5	0.48
10 Na$_2$O · 10 CaO · 25 Al$_2$O$_3$ · 55 SiO$_2$[a]	0.5	0	34.0	18.5	0.00

[a]) Values are extrapolated.

Table B.2: Standard enthalpy, oxygen activity at 1300°C and redox ratios determined by oxygen activity measurements in comparison with redox ratios determined by SWV for the reaction $1/2 Sn^{4+} \rightleftharpoons 1/2 Sn^{2+} + e^-$.

Composition (mol%)	[SnO$_2$] (mol%)	ΔH^0 (kJmol^{-1})	a_{O_2}	$log\left(\frac{Sn^{4+}}{Sn^{2+}}\right)$	T (°C)	Sn^{2+} (%) by SWV*	Sn^{4+} (%) by SWV*	Sn^{2+} (%) by a$_{O_2}$	Sn^{4+} (%) by a$_{O_2}$
20 Na$_2$O · 80 SiO$_2$	0.5	107(11)	0.0018	0.54	1600	29	71	22(8)	78(8)
16 Na$_2$O · 10 CaO · 20 Al$_2$O$_3$ · 54 SiO$_2$	0.5	72(7)	0.0127	0.05	1600	53	47	47(5)	53(5)
10 Na$_2$O · 10 CaO · 25 Al$_2$O$_3$ · 55 SiO$_2$ **	0.5	35(2)	0.0225	-0.75	1600	70	30	85(4)	15(4)
10 Na$_2$O · 10 CaO · 80 SiO$_2$	2.0	98(5)	0.0006	-0.26	1500	22	78	64(3)	36(3)
16 Na$_2$O · 10 CaO · 74 SiO$_2$	1.8	107(5)	0.0004	0.08	1450	13	87	45(3)	55(3)
20 Na$_2$O · 10 CaO · 70 SiO$_2$	1.6	104(5)	0.0005	0.13	1400	8	92	43(3)	57(3)
26 Na$_2$O · 10 CaO · 64 SiO$_2$	1.3	106(5)	0.0005	0.24	1400	7	93	37(3)	63(3)

*) For equilibrium with air at 1400°–1600°C, respectively.

**) Values are determined at 1500°C because of crystallisation at lower temperatures.

Table B.3: Diffusion activation energies and diffusion coefficients at 1300°C.

Composition (mol%)	[SnO$_2$] (mol%)	E$_D$ kJmol^{-1}	D cm^{2}s^{-1}
26 Li$_2$O · 74 SiO$_2$	0.5	222	$8.04 \cdot 10^{-8}$
33 Li$_2$O · 67 SiO$_2$	0.5	200	$2.54 \cdot 10^{-7}$
15 Na$_2$O · 85 SiO$_2$*	0.5	216	$1.41 \cdot 10^{-8}$
20 Na$_2$O · 80 SiO$_2$	0.25	222	$4.96 \cdot 10^{-8}$
26 Na$_2$O · 74 SiO$_2$	0.25	284	$8.10 \cdot 10^{-8}$
33 Na$_2$O · 67 SiO$_2$*	0.5	291	$9.25 \cdot 10^{-8}$
10 Na$_2$O · 10 CaO · 80 SiO$_2$	0.25	211	$3.20 \cdot 10^{-8}$
16 Na$_2$O · 10 CaO · 74 SiO$_2$	0.25	220	$7.41 \cdot 10^{-8}$
20 Na$_2$O · 10 CaO · 70 SiO$_2$	0.25	228	$7.57 \cdot 10^{-8}$
26 Na$_2$O · 10 CaO · 64 SiO$_2$	0.25	259	$8.77 \cdot 10^{-8}$
16 Li$_2$O · 10 CaO · 74 SiO$_2$	0.25	223	$4.76 \cdot 10^{-8}$
16 K$_2$O · 10 CaO · 74 SiO$_2$	0.25	318	$1.91 \cdot 10^{-8}$
16 Na$_2$O · 10 MgO · 74 SiO$_2$	0.25	277	$1.31 \cdot 10^{-8}$
20 Na$_2$O · 20 CaO · 60 SiO$_2$	0.5	229	$5.92 \cdot 10^{-7}$
16 Na$_2$O · 10 CaO · 5 Al$_2$O$_3$ · 69 SiO$_2$	0.5	234	$5.02 \cdot 10^{-8}$
16 Na$_2$O · 10 CaO · 10 Al$_2$O$_3$ · 64 SiO$_2$	0.25	303	$1.95 \cdot 10^{-8}$
16 Na$_2$O · 10 CaO · 15 Al$_2$O$_3$ · 59 SiO$_2$	0.5	257	$6.62 \cdot 10^{-8}$
16 Na$_2$O · 10 CaO · 20 Al$_2$O$_3$ · 54 SiO$_2$	0.5	304	$3.63 \cdot 10^{-8}$
10 Na$_2$O · 10 CaO · 5 Al$_2$O$_3$ · 75 SiO$_2$	0.5	285	$1.99 \cdot 10^{-8}$
10 Na$_2$O · 10 CaO · 15 Al$_2$O$_3$ · 65 SiO$_2$	0.5	252	$3.79 \cdot 10^{-8}$

*) Data are taken from Ref. [70].

Appendix C

Mössbauer parameters

Table C.1: Mössbauer parameters of silicates

T	Sn^{2+}				Sn^{4+}				$\frac{Sn^{4+}}{Sn^{2+}}$
	IS	QS	Γ	$ln\left(\frac{area}{background}\right)$	IS	QS	Γ	$ln\left(\frac{area}{background}\right)$	
(K)	(mms^{-1})				(mms^{-1})				corr.
20 Na$_2$O · 80 SiO$_2$ doped with 1.5 mol% SnO$_2$									
293	2.75	1.90	0.42	-2.52	-0.28	0.42	0.31	-2.18	0.6
373	2.74	1.87	0.33	-3.00	-0.29	0.36	0.27	-2.41	
473	2.74	1.81	0.29	-3.54	-0.31	0.33	0.25	-2.65	
573	2.69	1.78	0.34	-4.11	-0.35	0.34	0.26	-2.93	
673	2.66	1.72	0.31	-4.64	-0.36	0.33	0.25	-3.17	
26 Na$_2$O · 74 SiO$_2$ doped with 3.1 mol% SnO$_2$									
293	2.72	1.93	0.38	-3.01	-0.25	0.42	0.32	-1.51	2.0
373	2.71	1.88	0.38	-3.49	-0.27	0.40	0.30	-1.71	
473	2.67	1.85	0.43	-4.05	-0.30	0.42	0.32	-1.99	
573	2.65	1.81	0.40	-4.66	-0.32	0.39	0.30	-2.23	
673	2.62	1.78	0.23	-5.13	-0.35	0.37	0.28	-2.47	
10 Na$_2$O · 10 CaO · 80 SiO$_2$ doped with 2.4 mol% SnO$_2$									
293	2.81	1.90	0.40	-2.18	-0.26	0.45	0.28	-2.15	0.5
373	2.80	1.87	0.38	-2.59	-0.28	0.43	0.28	-2.33	
473	2.77	1.84	0.42	-3.11	-0.31	0.44	0.30	-2.58	
573	2.75	1.84	0.41	-3.60	-0.34	0.42	0.30	-2.83	
673	2.74	1.77	0.39	-4.14	-0.36	0.43	0.29	-3.08	

T	Sn^{2+}				Sn^{4+}				$\frac{Sn^{4+}}{Sn^{2+}}$
	IS	QS	Γ	$ln\left(\frac{area}{background}\right)$	IS	QS	Γ	$ln\left(\frac{area}{background}\right)$	
(K)	(mms^{-1})				(mms^{-1})				corr.
16 Na$_2$O · 10 CaO · 74 SiO$_2$ doped with 0.25 mol% SnO$_2$									
293	2.79	1.92	0.43	-4.73	-0.26	0.40	0.27	-3.26	1.9
16 Na$_2$O · 10 CaO · 74 SiO$_2$ doped with 1.6 mol% SnO$_2$									
293	2.78	1.92	0.46	-3.61	-0.26	0.43	0.31	-2.42	1.5
16 Na$_2$O · 10 CaO · 74 SiO$_2$ doped with 2.5 mol% SnO$_2$									
298	2.78	1.85	0.27	-2.57	-0.26	0.42	0.26	-1.46	1.4
473	2.72	1.86	0.40	-3.45	-0.30	0.41	0.26	-1.95	
573	2.71	1.82	0.43	-3.99	-0.33	0.41	0.15	-2.11	
673	2.63	1.95	0.81	-4.47	-0.36	0.40	0.21	-2.46	
773	2.61	1.89	0.30	-5.04	-0.38	0.37	0.19	-2.69	
20 Na$_2$O · 10 CaO · 70 SiO$_2$ doped with 3.0 mol% SnO$_2$									
293	2.75	1.91	0.32	-2.55	-0.24	0.42	0.22	-1.71	1.0
373	2.72	1.89	0.40	-2.93	-0.27	0.44	0.30	-1.88	
473	2.70	1.90	0.41	-3.40	-0.29	0.47	0.35	-2.10	
573	2.67	1.85	0.40	-3.97	-0.32	0.39	0.22	-2.36	
673	2.63	1.81	0.43	-4.48	-0.34	0.42	0.28	-2.62	
26 Na$_2$O · 10 CaO · 64 SiO$_2$ doped with 2.4 mol% SnO$_2$									
293	2.68	1.95	0.42	-2.83	-0.23	0.51	0.38	-1.44	1.8
373	2.65	1.93	0.44	-3.25	-0.25	0.49	0.37	-1.63	
473	2.60	1.91	0.45	-3.75	-0.28	0.47	0.35	-1.87	
573	2.54	1.90	0.46	-4.21	-0.31	0.48	0.36	-2.11	
673	2.57	1.89	0.47	-4.80	-0.33	0.43	0.32	-2.36	

Table C.2: Mössbauer parameters of alumosilicates

T	Sn^{2+}				Sn^{4+}				$\frac{Sn^{4+}}{Sn^{2+}}$
	IS	QS	Γ	$ln\left(\frac{area}{background}\right)$	IS	QS	Γ	$ln\left(\frac{area}{background}\right)$	
(K)	(mms^{-1})				(mms^{-1})				
16 Na$_2$O · 10 CaO · 5 Al$_2$O$_3$ · 69 SiO$_2$ doped with 0.5 mol% SnO$_2$									
293	2.79	1.92	0.41	-4.69	-0.23	0.44	0.30	-4.03	0.9
16 Na$_2$O · 10 CaO · 15 Al$_2$O$_3$ · 59 SiO$_2$ doped with 0.5 mol% SnO$_2$									
293	2.80	2.01	0.45	-4.86	-0.13	0.67	0.41	-4.09	1.0
16 Na$_2$O · 10 CaO · 20 Al$_2$O$_3$ · 54 SiO$_2$ doped with 1.6 mol% SnO$_2$									
293	n.d.				-0.04	0.82	0.45	-2.06	∞
373	n.d.				-0.08	0.81	0.44	-2.25	
474	n.d.				-0.12	0.77	0.40	-2.53	
573	n.d.				-0.16	0.73	0.40	-2.77	
673	n.d.				-0.19	0.74	0.40	-3.11	
773	n.d.				-0.22	0.72	0.38	-3.34	

Table C.3: Mössbauer parameters of silicates melted in reducing conditions

T	Sn^{2+}				Sn^{4+}				$\frac{Sn^{4+}}{Sn^{2+}}$
	IS	QS	Γ	$ln\left(\frac{area}{background}\right)$	IS	QS	Γ	$ln\left(\frac{area}{background}\right)$	
(K)	(mms^{-1})				(mms^{-1})				
10 Na$_2$O · 10 CaO · 80 SiO$_2$ doped with 2.0 mol% SnO$_2$ + 0.2 wt. C									
293	2.84	1.88	0.47	-4.82	-0.26	0.48	0.17	-4.44	0.7
16 Na$_2$O · 10 CaO · 74 SiO$_2$ doped with 1.8 mol% SnO$_2$ + 0.2 wt. C									
293	2.78	2.01	0.47	-5.40	-0.25	0.44	0.31	-3.90	2.0
20 Na$_2$O · 10 CaO · 70 SiO$_2$ doped with 1.6 mol% SnO$_2$ + 0.2 wt. C									
293	2.78	1.91	0.20	-3.82	-0.25	0.38	0.00	-2.84	1.2
26 Na$_2$O · 10 CaO · 64 SiO$_2$ doped with 1.3 mol% SnO$_2$ + 0.2 wt. C									
293	2.64	1.96	0.51	-5.48	-0.22	0.44	0.28	-3.92	2.1

Danksagung

Selbstständigkeitserklärung

Ich erkläre, dass ich die vorliegende Arbeit selbstständig und unter Verwendung der angegebenen Hilfsmittel, persönlichen Mitteilungen und Quellen angefertigt habe.

Jena, den 13.05.2003

Lebenslauf

Persönliche Daten

Name	Darja Benne
Geburtsdatum	11.03.1975
Geburtsort	Gehrden
Familienstand	ledig

Ausbildungsdaten

Aug. 1991–Juni 1994	Ganztagsgymnasium Barsinghausen
Juni 1994	Abitur
Okt. 1994–Juli 1995	Auslandsaufenthalt in Neuseeland
Okt. 1995–März 2000	Studium der Mineralogie an der Universität Hannover
März 2000	Diplom in Mineralogie
seit Aug. 2000	wissenschaftliche Mitarbeiterin am Otto-Schott-Institut für Glaschemie der Friedrich-Schiller-Universität Jena

Jena, den 13.05.2003